MASTERARBEIT | MASTER'S THESIS

Titel | Title

Characterization of FATZ-1 biomolecular condensates with Z-disc proteins α-actinin-2 and ZASP

verfasst von | submitted by

Izel Deniz Bilgi BSc

angestrebter akademischer Grad | in partial fulfilment of the requirements for the degree of

Master of Science (MSc)

Wien | Vienna, 2025

Studienkennzahl lt. Studienblatt | Degree programme code as it appears on the student record sheet:	UA 066 865
Studienrichtung lt. Studienblatt | Degree programme as it appears on the student record sheet:	Masterstudium Molecular Biology
Betreut von | Supervisor:	Univ.-Prof. Dipl.-Ing. Dr. Kristina Djinovic-Carugo

Abstract

The intrinsically disordered and phase-separating Z-disc protein FATZ-1 has multivalent interactions with major players of sarcomere maturation, including α-actinin-2 and ZASP. It was previously shown that the essential Z-disc proteins α-actinin-2 and ZASP colocalize in the FATZ-1 biomolecular condensates and that α-actinin-2 diminishes droplet formation *in vitro,* suggesting that these interactions might be regulatory and involved in signaling in the Z-disc. However, FATZ-1's role in sarcomere organization and the outcomes of its specific interactions is not yet fully understood. This thesis aims to elucidate how the phase-separation of FATZ is influenced by the colocalizing Z-disc proteins α-actinin-2 and ZASP, focusing on α-actinin-2. As myofibrillogenesis progresses, expression levels and local concentration of these proteins also change. Understanding how the FATZ-1 condensates are regulated might shed light on how the complex interactions and signaling required for myofibrillogenesis is achieved in the Z-disc. We used the established protein constructs Δ91-FATZ-1-GFP and α-actinin-2-Neeck. Taking the statistical Design of Experiment approach, we observed the droplet size, count and overall area covered by droplets at different protein concentrations using confocal microscopy. With these parameters to describe the condensate behavior, we created adapted phase-diagrams of FATZ-1 in function of the increasing concentration of the second Z-disc protein. Protein phase diagrams are important tools to map the complex landscape of phase-separating proteins and to pinpoint potentially important protein concentrations. Initial findings suggest that at the applied concentrations, α-actinin-2 does not change the droplet size, count or overall area covered in a coherent and reproducible manner. The same applies to ZASP, though ZASP experiments were done only in a preliminary way due to resource limitations. Interestingly, microscopy findings reported here do not support the outcome of the previously done turbidity assays with FATZ-1 and α-actinin-2, where droplet formation was reduced by increase of α-actinin-2 concentration. Thus, we repeated the turbidity assay with the protein constructs used in microscopy experiments. The results of the new turbidity assays agree with the microscopy experiments: there is no significant change in turbidity and thus phase-separation behavior, although an overall downwards trend was observed and turbidity at different concentrations changes in a different pace. This implies that the established protein constructs behave differently under liquid-liquid phase separation and more systematic experiments need to be done. Overall, this thesis provides a systematic approach to study FATZ-1 biomolecular condensates in context of colocalizing Z-disc proteins *in vitro,* highlighting links between different experimental outputs to contribute to the overall understanding of this elusive and complex system.

Zusammenfassung

Das intrinsisch ungeordnete und phasentrennende Z-disc Protein FATZ-1 hat multivalente Wechselwirkungen mit wichtigen Akteuren der Sarkomerreifung, einschließlich α-actinin-2 und ZASP. Zuvor wurde gezeigt, dass die essenziellen Z-disc Proteine α-actinin-2 und ZASP in den biomolekularen Kondensaten von FATZ-1 kolokalisieren und dass α-actinin-2 die Tröpfchenbildung *in vitro* verringert. Die Rolle von FATZ-1 bei der Organisation des Sarkomers und die Ergebnisse dieser spezifischen Interaktionen sind jedoch noch nicht vollständig geklärt. In dieser Arbeit soll geklärt werden, wie die Phasentrennung von FATZ durch die Z-disc Proteine α-actinin-2 und ZASP beeinflusst wird, wobei der Schwerpunkt auf α-actinin-2 liegt. Wenn wir verstehen, wie die FATZ-1-Kondensate reguliert werden, könnte dies Aufschluss darüber geben, wie die für die Myofibrillogenese erforderliche Signalübertragung in der Z-disc zustande kommen. Wir verwendeten die etablierten Proteinkonstrukte Δ91-FATZ-1-GFP und α-actinin-2-Neeck. Mit Hilfe der statistischen Versuchsplanung beobachteten wir die Tröpfchengröße, die Anzahl und die von den Tröpfchen bedeckte Gesamtfläche mit Hilfe der konfokalen Mikroskopie. Mit diesen Parametern zur Beschreibung des Kondensatverhaltens, erstellten wir angepasste Phasendiagramme von FATZ-1 in Abhängigkeit von der steigenden Konzentration des zweiten Z-disc Proteins. Erste Ergebnisse deuten darauf hin, dass α-actinin-2 bei den verwendeten Konzentrationen die Tröpfchengröße, die Anzahl, oder die insgesamt bedeckte Fläche nicht in reproduzierbarer Weise verändert. Das Gleiche gilt für ZASP, obwohl die ZASP-Experimente nur vorläufig durchgeführt wurden. Interessanterweise bestätigen die hier berichteten Resultate nicht die Ergebnisse der zuvor durchgeführten Trübungsversuche mit FATZ-1 und α-actinin-2, bei denen die Tröpfchenbildung durch eine Erhöhung der α-actinin-2-Konzentration reduziert wurde. Daher wiederholten wir den Trübungsversuch mit den in den Mikroskopieexperimenten verwendeten Konstrukten. Die Ergebnisse der neuen Trübungsassays stimmen mit den Mikroskopieexperimenten überein: Es gibt keine signifikante Veränderung der Trübung und damit des Phasentrennverhaltens, obwohl ein allgemeiner Abwärtstrend beobachtet wurde. Dies deutet darauf hin, dass sich die etablierten Proteinkonstrukte bei der Flüssig-Flüssig-Phasentrennung unterschiedlich verhalten und weitere systematische Experimente durchgeführt werden müssen. Insgesamt bietet diese Arbeit einen systematischen Ansatz zur Untersuchung von biomolekularen FATZ-1-Kondensaten im Zusammenhang mit kolokalisierenden Z-disc-Proteinen *in vitro* und hebt Verbindungen zwischen verschiedenen experimentellen Ergebnissen hervor, die zum Gesamtverständnis dieses komplexen Systems beitragen.

Table of Contents

1 List of Abbreviations

Abbreviation	Full form
Å	Angstrom (10^{-10} meters)
ABD	Actin-binding domain
ACTN2	α-actinin-2
AEX	Anion exchange
BC	Biomolecular condensate
c	Concentration
CAMD	Calmodulin-like domain
CM	Cardiomyocytes
CP	Centre-point
Cryo-ET	Cryogenic electron tomography
CTR	C-terminal region
Da	Dalton
DMSO	Dimethyl sulfoxide
DoE	Design of Experiment
DOL	Degree of labelling
EDTA	Ethylenediaminetetraacetic acid
F-actin	Actin filament
F-myosin	Myosin filament
FATZ	filamin, alpha-actinin-, and telethonin-binding protein of the Z-disc
FL	Full-length
FRAP	Fluorescence recovery after photobleaching
FUS	Fused In Sarcoma
GRR	Glycine-rich region
GuHCl	Guanidium hydrochloride
hiPSC	Human induced pluripotent stem cell
IMAC	Immobilized metal affinity chromatography

Abbreviation	Full form
IPTG	Isopropyl β-d-1-thiogalactopyranoside
ITC	Isothermal titration calorimetry
K_D	Dissociation constant
LLPS	Liquid-liquid phase separation
LM	Linear motif
AU	Absorbance units
MD	Molecular dynamics
MLO	Membraneless organelles
MW	Molecular weight
N	Sample size
NMR	Nuclear magnetic resonance
NTR	N-terminal region
OFAT	One-Factor-At-A-Time
PAGE	Polyacrylamide gel electrophoresis
PIP2	Phosphatidylinositol bisphosphate
PMSF	Phenylmethylsulfonyl fluoride
Pre3C	PreScission – human rhinovirus 3C
PTM	Post-translational modification
rpm	Rounds per minute
SDS	Sodium dodecyl sulfate
SEC	Size exclusion chromatography
SFLS	Stress fiber-like structures
SR	Spectrin-like repeats
suGFP	Superfolder green fluorescent protein
TEV	Tobacco etch virus
WT	Wild-type
ZASP	Z-disc-associated, alternatively spliced, PDZ-motif-containing protein

2 Introduction

2.1 The sarcomere

Macromolecular self-assembly is a fundamental aspect of biology. The sarcomere, the smallest contractile unit of the striated muscle, is the largest and most ordered multi-protein assembly in biology, sparking curiosity in cell and structural biologists alike (Gautel & Djinović-Carugo, 2016). Sarcomeres are composed of repetitive arrays of myofilaments composed of actin and myosin involved with a myriad of supporting proteins, anchored by their lateral boundaries known as the Z-discs. According to the Sliding Filament Model, muscle contraction is mediated by sliding of actin filaments (F-actins) over the myosin filaments (F-myosin), resulting in reversible pulling of the Z-discs together and thus shortening of the sarcomere (Huxley & Niedergerke, 1954).

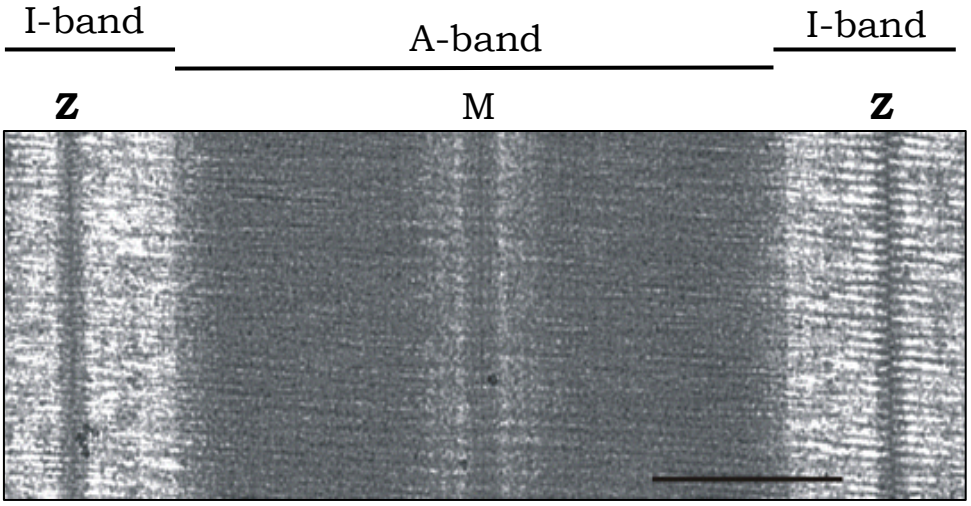

Figure 1: Electron micrograph of fish skeletal muscle sarcomere in longitudinal view. The Z-discs (Z) appear as dark zig-zags with defined width and F-actin overlaps. The dark staining stems from filament systems. The scale bar is 0.5 µm. The figure was adapted from Luther (2009).

The resting sarcomere of vertebrates is typically 2.2-2.3 micrometers (µm) in length and consists of distinct compositional zones (Squire *et al.*, 2005). The barbed (+) ends of F-actins are capped and anchored at the Z-disc, while the F-myosins are anchored at their center forming the central M-line of the sarcomere (Figure 1). F-actin and F-myosin partially overlap at the A-band, flanked by I-bands that do not harbor any F-myosin. Titin, the largest protein in the human proteome with a MW exceeding three megaDaltons (MDa), spans from the Z-disc to the M-line and is proposed to be an elastic "molecular

scaffold" during sarcomere assembly (Kontrogianni-Konstantopoulos *et al.*, 2009). Despite current advances in integrative approaches to uncover the Z-disc interactome, the molecular details and sequence of events during Z-disc and consequently sarcomere self-assembly remain elusive, largely due to the high multivalency of contributing proteins.

2.2 The Z-disc

The Z-disc is a protein-dense architecture that harbors α-actinin-2 crosslinks, F-actins, structural scaffolds like Titin and many other multivalent proteins. The main function of the Z-disc is maintaining the structural integrity of the sarcomere while serving as a hub for cell signaling (Sponga *et al.*, 2021). Accordingly, mutations in the major Z-disc proteins have been linked to the most common human (cardio-)myopathies including myofibrillar myopathy (Wadmore *et al.*, 2021).

At the Z-disc, antiparallel α-actinin-2 dimers crosslink the barbed (+) end of antiparallel F-actins as well as titin from the opposite sarcomere halves. In longitudinal view, the Z-disc appears as a zig-zagged band (Figure 1). The Z-disc is approximately 100-140 nanometers (nm) wide in slow muscles, including cardiac cells, and 30-40 nm in fast twitching muscle (Luther *et al.*, 2002). It is widely accepted that the transverse-sectional view of the Z-disc resembles a highly ordered, crystal-like lattice which changes from a small-square form to a distinct basketweave form upon contraction (Goldstein *et al.*, 1988). A recent cryogenic electron tomography (cryo-ET) study reaching a resolution of 10 angstroms (Å) revealed the three-dimensional architecture of the native rigor state mouse skeletal muscle sarcomere, offering novel insights into actin organization especially across I-Z-I zones (Z. Wang *et al.*, 2021). Z-discs in various thicknesses ranging from 80 nanometers (nm) to 100 nm were observed along a single, non-contractile and isolated myofibril. Accordingly, the authors proposed that the thickness of the Z-disc corresponds to different stress states, thin form likely representing a relaxed state. The α-actinin-2 mesh in thin Z-discs they have described is less ordered, contains doublets of crosslinks and forms more tetragonal patterns in contrast to previously described forms reviewed in detail (Luther, 2009).

Moreover, fluorescence recovery after photobleaching (FRAP) experiments done in skeletal myoblasts isolated from quail embryos revealed that the actin-binding Z-disc proteins exhibit remarkably higher exchange rates with the cytoplasmic pool than their half-lives (J. Wang *et al.*, 2005). These fast exchange rates imply that the Z-disc is a dynamic assembly capable of rapid incorporation of its components rather than a static structure as presumed from the electron micrographs. Furthermore, Z-body proteins FATZ, ZASP, α-

actinin-2 and filamin C showed faster rates in the Z-body stage. The Z-body is a transient structure in embryonic cells during early sarcomere development. The molecular details of how the para-crystalline Z-disc structure assembles from highly dynamic components present in the early stages of development is unknown.

2.2.1 The Z-body

The Z-bodies were first observed on "stress fiber-like structures" (SFLS) in embryonic cardiomyocytes (CMs) (Dlugosz *et al.*, 1984). The electron micrographs of immunostained SFLS showed that F-actins are stained continuously with periodical interruptions by puncta of α-actinin and non-muscle myosin. The SLFS are the "premyofibrils" of early development and the periodical dense bodies rich in α-actinin are the transient Z-bodies (Rhee *et al.*, 1994) (Figure 2).

As the cells mature, Z-bodies less than a micron in diameter at the spreading edges of the CMs merge into highly ordered Z-discs, suggesting that the Z-disc is potentially assembled from Z-bodies (Du *et al.*, 2003). These findings highlight the role of the Z-body as an assembly site for cytoskeletal molecules. However, the molecular mechanisms behind the transition from Z-body to the Z-disc is elusive.

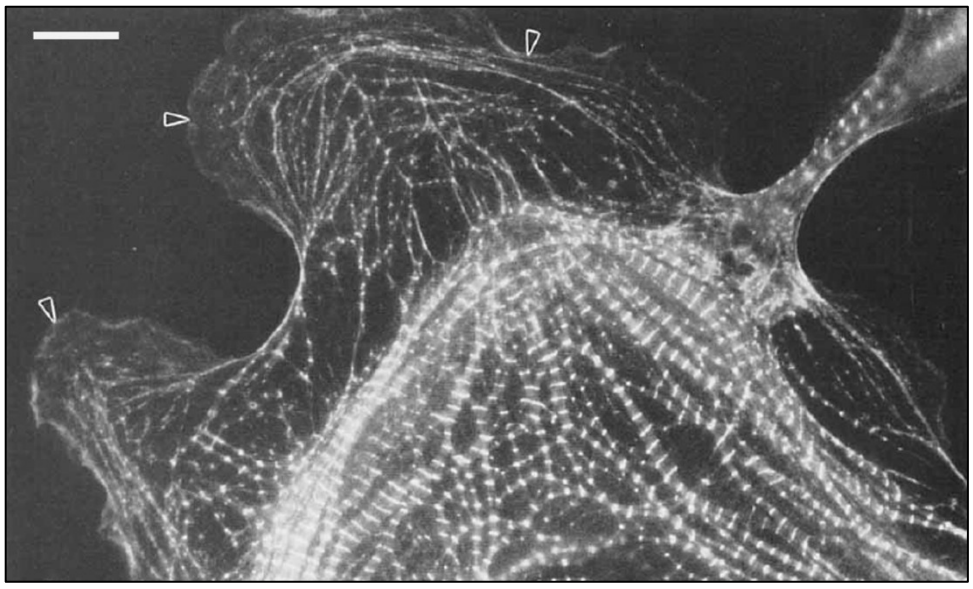

Figure 2: Chick CMs immunostained with α-actinin-2. Fibers at the cell periphery contain short spacings of concentrated α-actinin-2 (the Z-bodies) and form the early premyofibrils with "beads-on-a-string" appearance (arrowheads), according to the Premyofibril Model. The mature banded Z-discs are visible in the cell-center. The scale bar is 10 μm. The image was adapted from Rhee et al. (1994).

in vitro reconstituted models of Z-disc and Z-body can provide high resolution insights to the Z-body transition into the Z-disc. In his PhD, Philipp Galuska from Djinović Lab (Max Perutz Labs) was able to reconstitute Z-body-like-structures *in vitro* with distinctly fluorescent-labeled constructs of actin, α-actinin-2, FATZ, ZASP and Filamin C from purified components (unpublished data). This is an important milestone to uncover the sequential involvement of Z-body proteins in the event of myofibrillogenesis.

2.2.2 "Premyofibril Model" of Myofibrillogenesis

Myofibrillogenesis is the process of myofibril assembly and maturation within the sarcoplasm of myotubes during embryonic development. The mechanism of myofibrillogenesis is likely to be conserved in animals, since the sarcomere architecture is highly conserved. In mammals, the sarcomeric proteins transcriptionally switch isoforms across embryonic, neonatal and adult stages, strictly regulating expression levels (Kaya-Çopur *et al.*, 2021). Nevertheless, how the sarcomeres form, align and attach to each other and to the sarcolemma is an active area of research. Elucidating the roles of sarcomeric proteins during myofibrillogenesis may shed light on myopathies that arise from their defective assembly.

There are currently several models of myofibrillogenesis reviewed in detail elsewhere (Sanger *et al.*, 2006). The Premyofibril Model is the most comprehensive and widely accredited one, first adopted by Rhee *et al.* (1994). Premyofibril Model proposes that the sarcomere assembles from Z-discs and that the Z-body is the precursor of the Z-disc (Du *et al.*, 2003). At the initial step, premyofibrils are composed of "mini-sarcomeres" which contain all sarcomeric components necessary to initiate self-assembly (Sanger *et al.,* 2016) (Figure 3). In the mini-sarcomeres, Z-bodies are distributed along non-muscle myosin II and actin filaments. At the second step, Z-bodies from neighboring premyofibrils align into "beads-on-a-string" appearance through an undefined mechanism and form the nascent myofibrils. Nascent myofibrils contain Titin, muscle-myosin II as well as actin capping protein CapZ, yet are still less ordered compared to the mature myofibrils. At the final step of the mature myofibril, beaded Z-bodies have aligned into linear Z-discs, which contain myosin-associated proteins and Telethonin exclusive to the mature Z-disc (White *et al.*, 2014). Overall, the Premyofibril Model suggests a stepwise recruitment and incorporation of sarcomeric proteins into the Z-body during development.

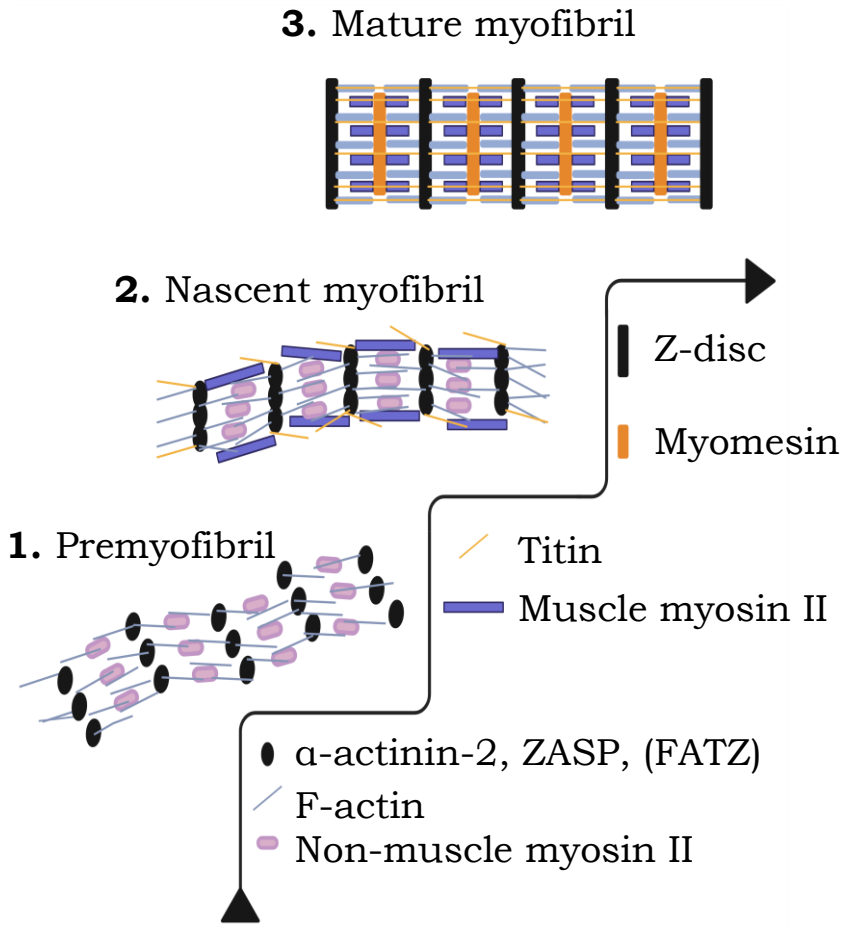

Figure 3: The Premyofibril Model. As myofibrillogenesis progresses, stepwise addition of Titin, muscle myosin II and supporting proteins like actin-capping protein CapZ organize the premyofibrils into a more aligned "nascent myofibril", with a beaded appearance. In the final step, non-muscle myosin is not present anymore. Z-disc exclusive protein telethonin and M-band proteins appear in the mature myofibril, which displays the highly ordered sarcomere structure. Figure was adapted from Sanger *et al.* (2016) in BioRender.

The major proteins important for skeletal muscle Z-body maturation into the Z-disc have been suggested over the years as actin, filamin C, α-actinin-2, ZASP and FATZ, without exact time-points of recruitment and action (Sanger *et al.*, 2016). In addition, the skeletal isoform of FATZ (FATZ-1) phase separates and forms a fuzzy polar complex with α-actinin-2 *in vitro* (Sponga *et al.*, 2021). The dynamic protein landscape, the transient nature and "merge" of Z-bodies raise the question whether FATZ phase separation plays a role in myofibrillogenesis.

Recently, an extensive BioID study captured the α-actinin-2 proximity-proteins in human induced pluripotent stem cell cardiomyocytes (hiPSC-CMs)

which mimic the Z-body and Z-disc stages (Ladha *et al.*, 2021). Confocal micrographs confirm that the cardiac troponin T-knockout cells are not able to form Z-discs and rest in a Z-body alike stage. In contrast, the troponin T-wild-type (WT) cells exhibit Z-discs. Using quantitative proteomics, Ladha *et al.* (2021) identified 324 α-actinin-2 proximity partners, only 24 of them exclusive to the Z-disc. Several isoforms of ZASP and cardiac isoform of FATZ (filamin, alpha-actinin-, and telethonin-binding protein of the Z-disc) were found to be enriched in Z-body-like structures, comparable with the Z-disc abundancies, further highlighting their involvement in early maturation. However, the hiPSC-CMs utilized in the Ladha *et al.* (2021) study are not contractile and represent a specific condition (troponin T-knockout) more than physiological Z-disc developmental stages.

2.3 Biomolecular Condensates

Cellular compartmentalization provides the cells spatiotemporal control over biological materials. The "membraneless organelles" (MLOs) are liquid-like self-assembling compartments formed exclusively by liquid-liquid phase separation (LLPS) (Boeynaems *et al.*, 2018). The MLOs, also known as "phase-separated droplets" and "biomolecular condensates" (BCs), concentrate and exchange biomolecules with the surrounding environment (Banani *et al.*, 2017). First described by Brangwynne *et al.* (2009) for P granules in a detailed biological context, LLPS is now realized as a major driving force for many supramolecular assemblies with heightened signaling functions and strong links to disease (B. Wang *et al.*, 2021). However, the molecular mechanisms behind LLPS of proteins, especially regarding its functionality and regulation, remain elusive.

BCs are formed by reversible LLPS and exhibit a wide range of liquid-like properties that are highly dynamic and versatile. In terms of morphology, droplets typically assume a spherical shape to minimize surface tension. Like simple liquids, phase-separated droplets fuse based on their surface tension and favorable interactions between their components, minimizing the total surface area exposed in macroscopic time scales. BCs also drip under gravitational and shear force. BCs might interact with a surface such as a coverslip due to attractive forces like hydrophobicity, flatten-out and wet the surface just like liquids (Feric *et al.*, 2016). Moreover, within the dense-phase, the molecules are mobile and in dynamic exchange with the dilute-phase in a rate determined by their diffusion. This means, BCs will recover fluorescence upon photobleaching of labeled components. Furthermore, the BCs may undergo "gelation", when the dense-phase transitions into a gel-like state due to increased molecular interactions and forms a viscoelastic network within the condensate, resulting in reduced dynamics (Kato *et al.*, 2012). The

reversibility of LLPS, along with dynamic exchange of molecules distinguishes liquid-like BCs from solid-like non-functional protein precipitates and aggregates such as the infamous amyloid fibrils formed by Fused In Sarcoma (FUS) protein (Patel *et al.*, 2015). In summary, BCs are liquid-like, spherical compartments formed by LLPS that concentrate proteins and exchange components with their surroundings.

2.3.1 Size Distribution of Biomolecular Condensates

Size of the condensates is linked to their biological function (Brangwynne, 2013). Studied biomolecular condensates are on a mesoscopic scale, with sizes ranging approximately from 0.2 to 2 μm, while variability by an order of magnitude is common even within the same type of BC (Hirose *et al.*, 2023; Spector, 2006). Mesoscopic scale defines a domain between nm and μm, where quantum phenomena interfere with macroscopic, statistical scale physics, influencing range-interactions and cooperativity along a polymer such as a peptide (Nakatsuji, 2013). Indeed, LLPS of biomolecules has emerged as an interdisciplinary field with recent application of material science principles to describe the behavior of phase-separated condensates. However, how the droplet size, count and position – described by a size distribution – is biologically regulated remains ambiguous.

A pioneering study recently demonstrated that the droplet size (the sphere volume) distribution is exponential and polydisperse (Lee *et al.*, 2023). Moreover, pathological condensates lean toward a power-law size distribution and non-Stokesian diffusion (e. g. preferential-attachment). Following these findings, the authors propose two mechanisms of droplet nucleation and growth, which influence the droplet size distribution first-hand, and are out of scope of this project. Another factor that contributes to the complex size distribution of droplets is Ostwald Ripening mediated by diffusion and surface energy, a scientific phenomenon describing how smaller droplets shrink in expense of larger droplets (Bressloff, 2020). Additionally, a "limiting component" within the condensates may control the size by limiting the amount of other components as proposed for centrosome assembly (Decker *et al.*, 2011). Overall, molecular concentration (c), droplet coarsening, nucleation and sequence-based interactions, all driven by LLPS principles, factor in the size of BCs.

2.3.2 Liquid-Liquid Phase Separation of Proteins

Macromolecules interact to varying extent through transient, low-affinity, and non-stereospecific forces. These non-covalent interactions include pi-stacking, cation-pi, electrostatic, hydrophobic forces between the aromatic residues, polar residues and charged residues. Hydrogen bonding and van der

Waals forces between atoms also contribute to weak interactions. LLPS occurs reversibly when the macromolecule/macromolecule interactions add up to be stronger than macromolecule/solvent interactions. To minimize the free energy, system demixes into two phases: a large "dilute-phase" and a small "dense-phase" (Banani *et al.*, 2017). At the equilibrium state, the concentration of both phases is maintained while allowing for a diffusive flux between them. Multivalent proteins often contain multiple low-affinity binding domains or intrinsically disordered regions (IDRs) and thus facilitate substantially high numbers of homo- or hetero-typical weak interactions. Proteins with "low-complexity" sequence patches and stretches of alternating charges can self-assemble into BCs *in vitro* (Nott *et al.*, 2015). Accordingly, computational tools can predict the phase separation propensity of a protein based on its amino acid sequence alone (Vernon & Forman-Kay, 2019). The widely accepted Sticker-Spacer Model was proposed based on molecular dynamics (MD) simulations, where stickers are the sequence motifs driving the multivalent interactions and spacers are the flexible linker regions that regulate dynamics of the condensates (Ranganathan & Shakhnovich, 2020). In light of this model, droplet kinetics at non-equilibrium states and thus size distribution can be better understood.

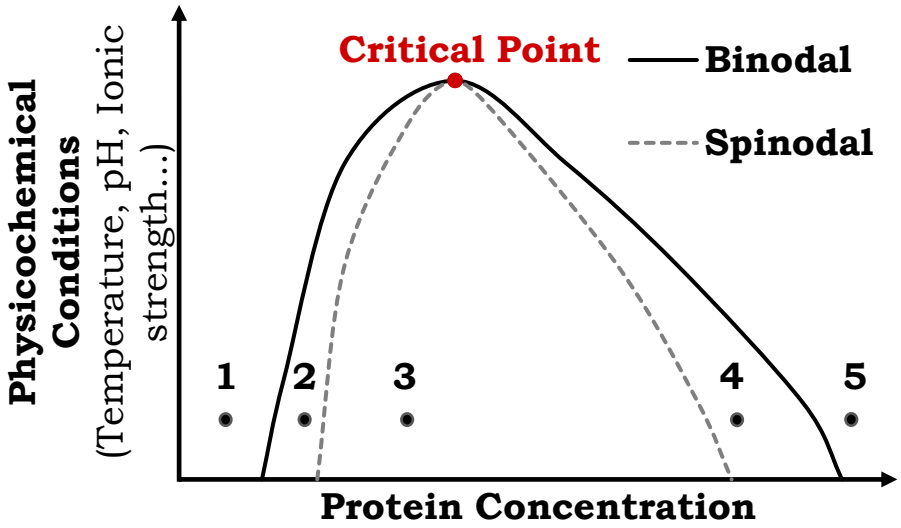

Figure 4: An imaginary protein phase diagram. Critical point (red) is where the two phases are indistinguishable with high fluctuations and opalescence. The binodal curve is also called the coexistence line and predicts formation of the condensates. Outside the binodal curve (Points 1 and 5), system is in 1-phase regime, uniform and well-mixed. Within the 2-phase regime (under the binodal) is the region of instability. Under the spinodal, the system demixes by "spinodal decomposition" (Point 3), depicted with dashed line. Points 2 and 4 are nucleation zones, where the condensates are "meta-stable" and nucleation events are prominent. The figure was adapted from Alberti *et al.* (2019).

Moreover, *in vitro* LLPS is highly sensitive to experimental conditions such as buffer additives, concentration, pH and temperature and does not occur until a specific condition is reached. Protein phase diagrams describe the LLPS behavior of a protein at increasing concentrations in function of a physicochemical condition via the "coexistence line" (binodal) that separates one-phase and two-phase states (Alberti *et al.*, 2019) (Figure 4). Recently, a phase diagram of FUS at increasing ionic strength conditions was created (Arter *et al.*, 2022). In analogy to crystallographic phase diagrams, protein phase diagrams are used to understand the phase boundaries, transitions, critical points, metastable and supersaturation zones, where droplet kinetics vary across phase diagram regions (Cinar & Winter, 2020). Thus, multi-angled approaches are required to study the complex phase-space of proteins.

2.3.3 Techniques to Study Protein Phase Separation

Previously utilized in optimization of protein crystallization, statistically designed experiments with Design of Experiment (DoE) approach take into account the combined effects on a process in stark contrast to One-Factor-At-A-Time (OFAT) screening approach (Papaneophytou, 2019). Notably, the choice of DoE design, such as a full-factorial, incomplete-factorial or response-surface-methodology (RSM), depends heavily on the amount of available resources and existing knowledge about the system being studied. Overall, studying the phase-space of proteins requires a systematic and statistical approach which allows to distinguish the numerous external and internal effects that influence LLPS.

To detect and study LLPS of proteins, confocal microscopy and turbidity assays are used commonly in combination (Alberti *et al.,* 2019). Turbidity assays are a primarily useful tool to study early onset of LLPS, where the system is far from the critical point and diffusion or other biologically relevant processes like coarsening are not reducing accuracy (Alberti *et al.*, 2019; Cinar & Winter, 2020). The amount of scattered light depends on the light wavelength, refractive indices of the droplets as well as the medium and the size distribution of the droplets without distinguishing the droplet size, shape or number. Thus, turbidity measurements are meaningful alongside microscopic observation of droplets.

The size, count and shape of BCs can be determined in high-resolution using confocal microscopy. With current advances in microscopy equipment, labeling techniques and development of versatile fluorophore-tags which are non-invasive to protein structure and dynamics, multi-component experiments can be done using confocal microscopy. In the confocal microscope, the dichroic mirror directs the laser-beam onto the sample, while

allowing the emitted fluorescence wavelength to pass and reach the detector through a pinhole. This way, out-of-focus light is removed efficiently and a resolution theoretically up to 0.2 µm laterally and 0.6 µm axially can be reached (Elliott, 2020). However, the effect of fluorescent-tags on protein LLPS has not been systematically studied yet. Recently, the *in vitro* LLPS behavior of tau-GFP linked to Alzheimer's disease was described by using confocal microscopy, while demonstrating that conjugation of fluorescent probes to tau interfered with binding and aggregation properties (Kanaan *et al.*, 2020).

To study whether colocalizing Z-body proteins α-actinin-2-Neeck and ZASP influence LLPS behavior of FATZ-1 condensates *in vitro,* adapted phase diagrams of truncated and GFP-fused FATZ-1 construct (Δ91-FATZ-1-GFP) in function of fluorescently labeled α-actinin-2-Neeck and ZASP concentrations were generated using confocal microscopy imaging experiments designed with DoE approach.

2.4 FATZ-1

FATZ-1 is encoded by *MYOZ1* in humans and belongs to the FATZ family of proteins. It is also known as Myozenin or Calsarcin due to its discovery at similar time points by different research groups. FATZ-1 (Myozenin-1 or Calsarcin-2) is the skeletal muscle isoform predominant in fast-twitch fibers. Particularly, FATZ is a "hotspot" for human myopathies (Frank *et al.*, 2006).

FATZ-1 is an intrinsically disordered protein with a MW of approximately 31 kDa without distinct structural domains or canonical binding sites. Functionally, it has a glycine-rich region (GRR) region between its N-terminal region (NTR) and C-terminal region (CTR) (Figure 5A). The protein lacks secondary structural elements and is highly flexible in solution (Sponga *et al.*, 2021). Thus, FATZ-1 structure is a dynamic ensemble of various conformations.

FATZ-1 fulfills both structural and signaling roles in the sarcomere, acting as a multivalent interaction hub in the Z-disc (Sponga *et al.*, 2021). According to Western blot and immunofluorescence data, the level of FATZ-1 increases during development (Faulkner *et al.*, 2000). In context of the Premyofibril Model, FATZ-1 is considered to be present in the myofibrillogenesis from "mini-sarcomere" stage on without an exact knowledge on timing, together with its interaction partners filamin C, ZASP and α-actinin-2 (J. Wang *et al.*, 2005). FATZ interaction with the PDZ domain of ZASP indicates potential involvement in signaling and PTM pathways (Von Nandelstadh *et al.*, 2009). Its yet unmapped interaction with Calcineurin, a phosphatase regulating the gene expression of muscle differentiation and composition, is possibly

inhibitory (Frey *et al.*, 2004). Studying FATZ-1 interactions with other Z-disc proteins might provide new insights to how the Z-disc assembles and fulfills its roles.

2.4.1 FATZ-1 phase-separates *in vitro*

After observing temperature-reversible turbidity with naked-eye in the sample, Sponga *et al.* (2021) demonstrated that FATZ-1 undergoes temperature-dependent LLPS *in vitro*. The authors observed droplet formation by microscopy and turbidity assays, as well as self-interaction (homotypic) of FATZ proteins by nuclear magnetic resonance (NMR) experiments.

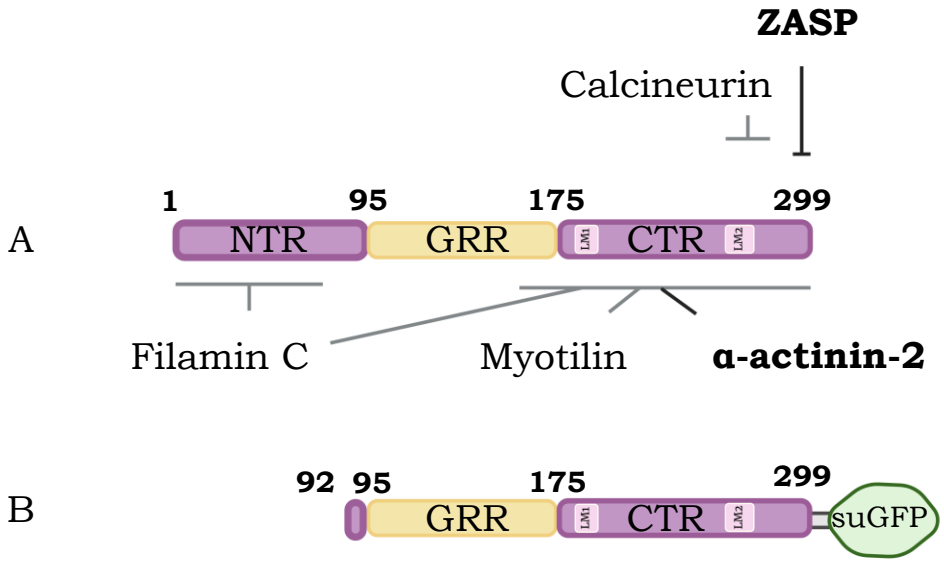

Figure 5: Schematics of FATZ-1. **5A**: FATZ-1-WT interactome and functional regions indicated by residue numbers. NTR is the N-terminal region, GRR is the "glycine-rich region", and CTR is the C-terminal region which contains non-canonical binding sites for ZASP and α-actinin-2. LM1 (residues 180 to 199) and LM2 (residues 216 to 240) found in the CTR are the sequence motifs responsible for α-actinin-2 binding. **5B**: Schematics of Δ91-FATZ-1-GFP construct used in this project. The N-terminal His_6-tag is not depicted. Figure was adapted from Sponga *et al.* (2021) using BioRender.

The primary structure of intrinsically disordered FATZ-1 contains blocks of alternating charges, aromatic residue patches and two arginine/glycine/glycine (RGG) motifs, as well as low-complexity sequence stretches (Sponga *et al.*, 2021). Each of these sequence qualities are typical indicators for protein LLPS. Accordingly, FATZ-1 phase separation propensity

score was predicted to be highest for the GRR (amino acids 100 to 180) based on long-range pi-pi interactions as well as on whole sequence length, disorder and composition by bioinformatic prediction tools. The P-X_n-G motifs, found twice in GRR and once in CTR of FATZ-1, were reported to enhance LLPS typically in a lower critical solution transition, meaning that phase-transition occurs above a threshold temperature (Quiroz & Chilkoti, 2015). The temperature-dependency of FATZ-1 LLPS suggests that majorly hydrophobic reactions drive the phase-transition, more than charge-charge or pi-interactions. Condensate dissolution assays showed that, increasing the arginine concentration above a certain threshold prevented droplet formation by Δ91-FATZ-1 at 50 to 150 µM, indicating that cation-pi interactions additionally mediate Δ91-FATZ-1 phase separation.

Moreover, to pinpoint which regions of FATZ-1 are responsible for LLPS, the authors generated different constructs of FATZ-1 (Figure 5A: FATZ-1-WT). The FATZ-1-WT precipitated under every condition, when temperature was raised from 4° C to 22° C. The N-FATZ-1 (amino acids 1 to 174) lacks the CTR and did not form droplets at any temperature. Meanwhile the Δ91-FATZ-1 (amino acids 92 to 299) construct lacking the NTR did form droplets spontaneously and reversibly when changing the temperature from 4° C to 22° C or 37 ° C degrees, with sizes reaching up to 20 µm. Hence, transient homotypic interactions of GRR and especially CTR mediate LLPS of FATZ-1.

FATZ-1 interacts with α-actinin-2 over the Linear Motifs 1 and 2 (LM1 and LM2) found on its CTR (Figure 5A). To investigate whether α-actinin-2 binding impacts FATZ-1 condensates, Sponga *et al.* (2021) showed with turbidity measurements done at 37 °C with optical density at 600 nm (OD_{600}), that increasing the α-actinin-2 concentration (from 0.25 to 8 µM) while holding Δ91-FATZ-1 concentration constant (50 or 65 µM) prevented droplet formation. Furthermore, pre-formed condensates of His_6-tagged Δ91-FATZ-1 were dissolved by increasing α-actinin-2 in a concentrate-dependent manner (without Arginine). Adding LM2 peptide, to sequester α-actinin-2, restored droplet formation. However, the representativeness and physiological/biological relevance of the constructs and of the turbidity measurements remains to be systematically studied further.

The Δ91-FATZ-1-GFP construct contains an N-terminal His_6-tag, amino acids 92 to 299 and a C-terminal superfolder GFP (suGFP) fusion (Table 6, Figure 5B). According to Sponga *et al.* (2021), the Δ91-FATZ-1-GFP condensates have a diffusion coefficient *D* of 0.096 μm^2/sec, which is two orders of magnitude lower than for bovine serum albumin, indicator of a crowded environment (dense-phase) and the half-time of recovery $t_{1/2}$=12.7 sec is within the accepted range of values for phase-separated droplets exhibiting dynamic

exchange rates (Yin *et al.* 2015). FRAP experiments, together with the morphology and reversibility of droplets, confirmed the liquid-like nature of Δ91-FATZ-1-GFP droplets. This masters project investigates how the α-actinin-2-Neeck mutant and ZASP concentration influence Δ91-FATZ-1-GFP condensate area and count with confocal microscopy.

2.4.2 FATZ-1 interaction with α-actinin-2

Sponga *et al.* (2021) demonstrated that FATZ-1 forms a 2:1 "fuzzy" complex with the dimeric rod of α-actinin-2. In fuzzy complexes, the dynamic disorder and structural multiplicity is preserved while allowing for specific interactions and the IDRs modulate affinity by providing nonspecific and transient anchors to binding partners (Schiaffino *et al.*, 2013). FATZ-1 remains conformationally heterogenic except for two LMs flanked by disordered regions in the CTR. LM1 (residues 180 to 199) and LM2 (residues 216 to 240) show "disorder-to-order" transition upon binding α-actinin-2 (Figure 5A&B). Precisely, residues Tyr^{218} – Tyr^{228} within the LM2 were identified as the major binding site for α-actinin-2. Moreover, LM1 and LM2 carry proline-tryptophan/phenylalanine (P-W/F) motifs that are often found in slow cis/trans conformational switches in regulatory interactions (Sponga *et al.,* 2021).

Isothermal titration calorimetry (ITC) data revealed two independent, non-cooperative binding events for FATZ-1- α-actinin-2 interaction. The binding model suggests that the first FATZ-1 molecule binds α-actinin-2 through main (LM1 and LM2 in the CTR) and secondary binding sites with lower nanomolar affinity (K_{D1} = 3.5 nM), while a second FATZ-1 molecule binding is possible yet in higher nanomolar affinity (K_{D2} = 314 nM), forming a polar architecture arising from setting of concave side of α-actinin-2. Therefore, it is possible that the polar α-actinin-2/FATZ-1 complex functions as a scaffolding actor in the Z-disc organization.

2.5 α-actinin-2

α-actinin-2, encoded by *ACTN2* in humans, belongs to the spectrin superfamily and is a calcium-insensitive sarcomeric isoform of α-actinin which is predominant in the cardiac and oxidative skeletal muscle. The PaxDB 5.0 (protein abundance database) lists α-actinin-2 among the top 10% most abundant proteins in the whole human body and in top 5% in the human heart according to the 2014 PeptideAtlas dataset (Deutsch *et al.*, 2015; Huang *et al.*, 2023). Today, more than 10 variants of *ACTN2* gene are classified as causative of (cardio-)myopathies (Ranta-aho *et al.*, 2022).

α-actinin-2 is the primary structural scaffold of the Z-disc. As an antiparallel homodimer, it crosslinks antiparallel actin filaments from adjacent sarcomeres via its N-terminal actin-binding-domains (ABD), forming the typical Z-disc lattice. α-actinin-2 also binds alternatively spliced Titin Z-repeats, potentially influencing the Z-disc dimensions (Gautel *et al.*, 1996). Its interaction with phosphatidylinositol bisphosphate (PIP2) and PDZ domain proteins like ZASP suggests roles in myofibrillar differentiation and regulation of binding properties by phospholipid pathways (Mills *et al.*, 2001). Furthermore, α-actinin-2 is one of the earliest constituents of the Z-body. Overall, α-actinin-2 serves as a crucial multivalent interaction platform within the Z-disc, facilitating a wide range of structural and signaling interactions including with FATZ-1 (Sjöblom *et al.*, 2008) (Figure 6A).

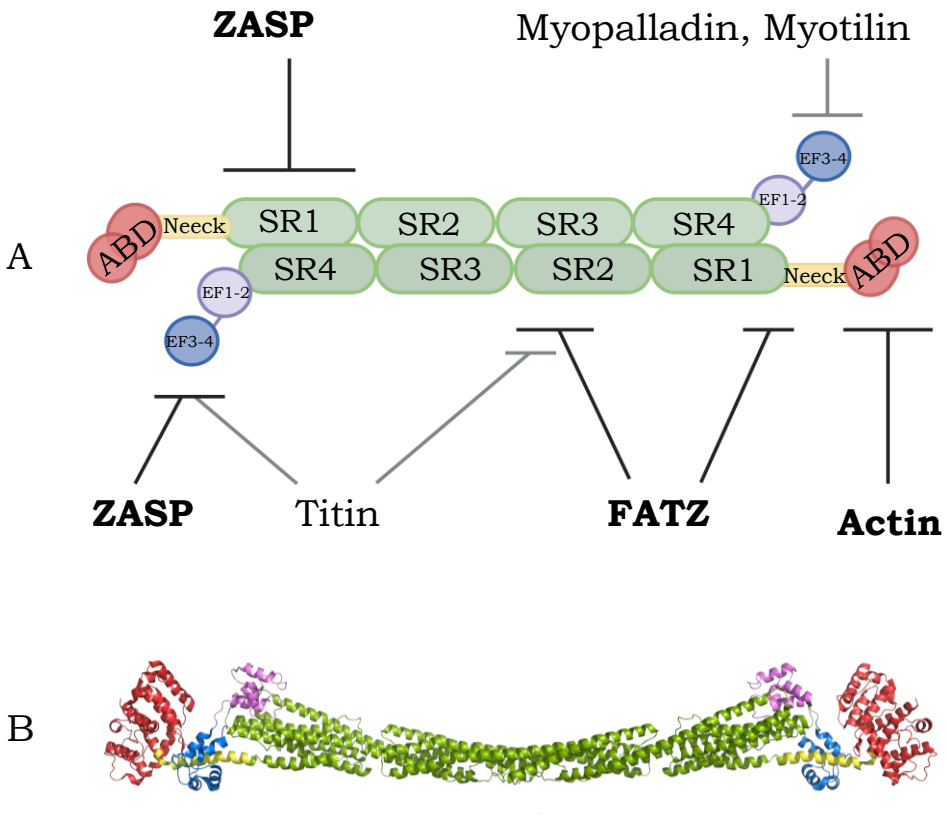

Figure 6: Schematics of α-actinin-2-Neeck mutant and crystal structure of α-actinin-2 in open conformation. **5A**: The α-actinin-2-Neck construct is in a consecutively open conformation due to mutations R268E/I269E/L273E in the Neck region. These disrupt the interaction of Neck with the EF3-4 and therefore provide a hyper-activated binding state, where EF-hands and ABD are free to adopt various orientations. Figure was adapted from Ribeiro *et al.* (2014) using BioRender. **5B:** Crystal structure of α-actinin-2 in open conformation, in absence of PIP2. Color code: Actin-binding domain (red), helical Neck (yellow), helical rod domain SR1-4 (green), EF-hands 1-4 (violet) and EF3-4 (blue). The structure (PDB: 4D1E) was visualized using PyMOL (2.5.4).

The human sarcomeric α-actinin-2 crystal structure in closed/autoinhibited conformation depicted in Figure 6B was solved at 3.5 Å resolution, providing critical insights into its conformational landscape and regulation by PIP2 (Ribeiro *et al.*, 2014). α-actinin-2 is an elongated, antiparallel homodimer with a MW of approximately 208 kDa. The monomer consists of an N-terminal (ABD) followed by four helical spectrin-like repeats (SR1-4) forming the "rod" functional domain. The six-turn α-helical linker "Neck", flanked by flexible hinges, connects the rod domain and the C-terminal region, which contains a calmodulin-like-domain (CAMD) of two pairs of EF hands (EF1-2 and EF3-4), which are helix-loop-helix motifs found in calcium-binding proteins.

In absence of PIP2, the closed-conformation of α-actinin-2 is energetically more favorable than the open-conformation. Upon PIP2-binding to ABD, an activated state is triggered with lower activation energy for "opening": EF3-4 hands with CAMD are released from Neck and in this open conformation, CAMD is free to interact to the titin Z-repeats in nanomolar affinity rather than with Neck itself. The actin-binding sites of α-actinin-2 are not inhibited by interdomain interactions in neither of the conformations. Furthermore, Neck peptide was shown to be unstructured when not bound to CAMD.

Ribeiro *et al.* (2014) generated a consecutively open variant of α-actinin-2 by disrupting the key contacts between Neck and EF3-4. Two hydrophobic residues and one positively charged residue of Neck region was replaced with negatively charged glutamic acid residues (R268E/I269E/L273E), and the mutant was termed α-actinin-2-Neeck. In α-actinin-2-Neeck, EF3-4 hands are in open conformation, allowing for actin crosslinking even without PIP2 activation (Figure 6A). Moreover, α-actinin-2-Neeck has the same molecular weight as α-actinin-2-WT but a higher Stokes radius (R_s), in agreement with increased mobility. α-actinin-2-Neeck transfected CMs displayed widening Z-discs that eventually disintegrated, possibly due to out-of-control incorporation of actin, titin and α-actinin-2 into the Z-discs.

2.6 ZASP

Z-disc-associated, alternatively spliced, PDZ-motif-containing protein (ZASP, also called Cypher or Oracle) belongs to the Enigma family of proteins and is encoded by *LDB3* in humans. It is highly conserved and is present at the earliest Z-disc developmental stages together with α-actinin, essential for Z-disc stability (Katzemich *et al.*, 2013). Typically, ZASP has an N-terminal α-actinin-binding PDZ domain, a central uncharacterized Zasp Motif (ZM) and none or up to four protein-protein interaction LIM domains related to signaling pathways. Human ZASP has more than 8 isoforms, adding to the complexity of sarcomere formation and new ones are ongoingly being identified. ZASP isoforms differ in having different numbers and combinations of ZM, LIM and PDZ domains and are linked to severe Z-disc associated myopathies (Henderson *et al.*, 2017).

ZASP interacts with FATZ-1 and alpha-actinin-2 via the PDZ binding motifs (Von Nandelstadh *et al.*, 2009). Moreover, ZASP colocalizes in the FATZ-1 biomolecular condensates *in vitro*. In this study, we worked with the full-length skeletal muscle ZASP isoform 6 which has the PDZ domain and ZM but no LIM domain, since it is regarded as one of the experimenter-friendlier and soluble constructs in comparison to other ZASP isoforms (Figure 7).

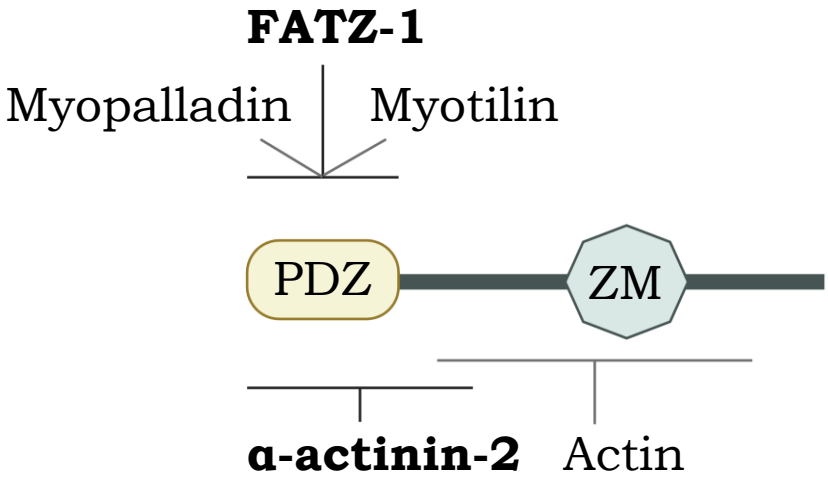

Figure 6: Schematics and interactome of full-length ZASP (isoform 6). No LIM domain. PDZ domain is responsible for interaction with both FATZ and α-actinin-2.

2.7 Aim of Studies

In this study we aim to elucidate how FATZ-1 biomolecular condensates are influenced by the increasing concentration of interacting Z-disc proteins α-actinin-2 and ZASP, with a particular focus on α-actinin-2, in context of sarcomere maturation.

Previous microscopy experiments have shown that α-actinin and ZASP colocalize in the FATZ-1 droplets and turbidity assays suggested that α-actinin-2 diminishes the pre-formed FATZ-1 droplets, suggesting that their interaction might be regulatory and important for Z-disc maturation from Z-bodies (Sponga *et al.* 2021). However, the specific function of FATZ-1 and its interactions is yet to be uncovered.

To assess the relationship between Δ91-FATZ-1-GFP condensates and concentration of a second Z-disc protein, we plan to create protein phase diagrams that parametrize droplet size, count and area covered using confocal imaging. To systematically image the condensates while reducing the amount of resources to a minimum, imaging experiments are to be statistically designed with DoE approach. The fluorescent labeling of α-actinin-2-Neeck and ZASP is already established in the lab and the labeled proteins together with Δ91-FATZ-1-GFP will be imaged at strictly identical conditions and at the 10^{th} minute of incubation at 37 °C.

The main aim extends further to observe the change in turbidity upon increasing the α-actinin-2 concentration as another experimental output. This allows us to compare utilized protein constructs with previously done experiments in our lab and also contribute to understanding of FATZ-1 droplet behavior based on a commonly accepted LLPS measure.

Our study addresses the elusive role of FATZ-1 and its phase-separation in context of myofibrillogenesis and how it might be regulated by key players of the Z-disc, namely α-actinin-2 and ZASP.

3 Materials and Methods

Protein expression, purification and labelling protocols were established by previous members of the Djinović lab.

3.1 Laboratory Materials

Table 1: Laboratory equipment used in this study.

Equipment	Type	Brand
Protein Purification		
Chromatography System	ÄKTA Pure	Cytiva (GE Healthcare)
Software	Unicorn 7.8	
IMAC column	5 ml-HisTrap FF crude	
AEX column	6 ml-Resource Q	
SEC columns		
Protein Purification (all)	HiLoad 26/600 Superdex 200 pg	
Neeck labelling	Superdex 200 Increase 10/300 GL	
ZASP labelling	Superdex 75 10/300 GL	
Biomolecular Imager	Amersham Typhoon	
Spectrometer	NanoDrop One	Thermo Scientific
Condensate imaging		
Glass slide	Superfrost™ microscopy slide	New Erie Scientific LLC
PCR-strip	0.2 ml Amplitube	Simport Scientific
Cover slides	Borosilicate glass, 18 x 18 mm	Jena Bioscience
Spacer	13 mm x 0.12 mm SecureSeal	Grace Bio-Labs
Confocal Microscope	LSM 980 with Airyscan 2	Zeiss
Objective	Plan-Apochromat 63x/1.4 Oil DIC	
Lasers	480 nm (30 mW), 561 nm (25 mW), 639 nm (25 mW)	
Software	ZEN 3.3	

Table 2: List of buffers and their composition used in this study. SEC Buffer A9 is the final buffer for all experiments.

Buffers	Composition
SEC Buffer (A9)	50 mM Tris, 100 mM NaCl, 50 mM Arginine, 50 mM GuHCl, 1 mM β-ME, 1 mM EDTA, 0.5 mM PMSF (pH 7.5)
Δ91-FATZ-1-GFP	
Lysis Buffer	50 mM Tris, 150 mM NaCl, (pH 7.5)
Resuspension Buffer	50 mM Tris, 150 mM NaCl, 4 M Urea (pH 7.5)
HisTrap Buffer A	50 mM Tris, 150 mM NaCl, 2 M Urea, 20 mM Imidazole (pH 7.5)
HisTrap Buffer B	50 mM Tris, 150 mM NaCl, 1 M Urea, 250 mM Imidazole (pH 7.5)
ResQ Buffer A	50 mM Tris, 1 M Urea (pH 8)
ResQ Buffer B	50 mM Tris, 2M NaCl, 1 M Urea (pH 8)
α-actinin-2-Neeck	
Lysis Buffer	50 mM Tris, 150 mM NaCl, 0.5% Triton X-100, 0.5 mM EDTA, 5% Glycerol (pH 8)
HisTrap Buffer A	50 mM Tris, 150 mM NaCl, 20 mM Imidazole, 2 mM β-ME (pH 7.5)
HisTrap Buffer B	50 mM Tris, 150 mM NaCl, 500 mM Imidazole, 2 mM β-ME (pH 7.5)
TEV Cleavage Buffer	50 mM Tris, 0.5 mM EDTA, 1 mM DTT (pH 8)
ResQ Buffer A	50 mM Tris, 0.5 mM EDTA, 0.1 mM PMSF, 2mM β-ME (pH 7.5)
ResQ Buffer B	50 mM Tris, 1 M NaCl, 0.5 mM EDTA, 0.1 mM PMSF, 2 mM β-ME (pH 7.5)
ZASP	
Lysis Buffer	1x PBS, 4M GuHCl, 0.2% Tween 20 (pH 7.5)
HisTrap Buffer A	1x PBS, 3M GuHCl, 300mM NaCl, 20 mM Imidazole, 5% Glycerol (pH 7.5)
HisTrap Buffer B	1x PBS, 3M GuHCl, 300 mM NaCl, 500 mM Imidazole, 5% Glycerol (pH 7.5)
ZASP SEC Buffer	1x PBS, 3 M GuHCl, 300 mM NaCl, 5% Glycerol (pH 7.4)
Pre3C Cleavage Buffer	20 mM Tris, 150 mM NaCl, 1 mM DTT (pH 7.5)
Dialysis Buffer 1	3 M Urea, 50 mM NaOAc, 100mM NaCl (pH 5)
Dialysis Buffer 2	2 M Urea, 50 mM NaOAc, 100 mM NaCl (pH 5)
Dialysis Buffer 3	1 M Urea, 50 mM NaOAc, 100 mM NaCl (pH 5)
Dialysis Buffer 4	50 mM NaOAc, 100 mM NaCl (pH 5)
Refolding Buffer	50 mM NaH_2PO_4, 100 mM NaCl (pH 6.1)

Table 3: Contents of the growth media for protein overexpression and of the protease inhibitor cocktail used in cell lysis. The autoinduction medium was modified from (Studier, 2005).

Expression Media	**Content**
Lysogeny Broth (LB) medium (lab stock)	10 g tryptone, 5 g yeast extract, 10 g NaCl, to 1 L ddH_2O
ZYP 5052 Autoinduction medium	10 g of any tryptic digest of casein, 5 g yeast extract, 1000 ml H_2O, 20xP (0.5 M $(NH_4)SO_4$, 1 M KH_2PO_4, 1 M Na_2HPO_4), 50x5052 (25% Glycerol, 2.5% Glucose, 10% α-lactose), 1 M $MgSO_4$
Reagent	
Protease Inhibitor Cocktail (lab stock)	100 µM bestatin hydrochloride, 14 µM E64 protease inhibitor, 10 µM pepstatin A, 1 µM phosphoramidon disodium salt, dissolved in DMSO

Table 4: Materials used for sortase labelling of proteins. Sortase A was expressed and purified by lab members based on protocols established in the lab. Step of peptide labelling with the fluorescent dye was performed by previous lab members and Philipp Galuska.

Reagent	**Name**	**MW [Da]**	**Source**
Peptide Probe	CLPETG	618	GenScript
Dye for Neeck	ATTO 680 maleimide	1024	ATTO-TEC
Dye for ZASP	ATTO 565 maleimide	733	ATTO-TEC
Sortase A *(Protein Ligase)*	$SrtA_a$	27700	(Hess *et al.*, 2012)

Table 5: Detailed properties of the fluorescent labels used in this study, sourced from the manufacturer product sheets (ATTO-TEC, 2023). CF_{280} stands for correction factor at 280 nm.

Fluorescent Dye	**ATTO 680**	**ATTO 565**
Protein to label	ACTN2-Neeck	ZASP
Modification	Maleimide (thiol-reactive)	Maleimide (thiol-reactive)
MW [Da]	1024	733
$\lambda_{absorbance}$ [nm]	681	564
$\lambda_{emission}$ [nm]	698	590
ε_{max} [$M^{-1}cm^{-1}$]	125000	120000
CF_{280}	0.17	0.12

3.2 Constructs and Strains

Table 6: Protein constructs and bacterial strains used in this study. The theoretical (Thr.) protein parameters were sourced from Expasy ProtParam web-tool (Gasteiger *et al.*, 2005). suGFP stands for superfolder GFP (Pédelacq *et al.,* 2006)).

Construct	**Δ91-FATZ-1-GFP**	**α-actinin-2-Neeck (monomer)**	**ZASP**
Protein	FATZ-1	α-actinin-2	ZASP
Description	Truncated N-terminus	R268E/I269E/L273E mutations	Full length, isoform 6
Length [aa]	469	913	303
Thr. Molecular Weight [kDa]	50.583 (suGFP: 26.781)	103.958	33.251
Thr. Extinction Coefficient [$M^{-1}cm^{-1}$]	43320	126740	25440
Thr. Isoelectric Point [pH]	6.09	5.22	9.17
Thr. A_{280} 0.1% (=1 g/L)	0.856	1.219	0.765
Reference	Sponga *et al.* (2021)	Ribeiro *et al.* (2014)	-
Vector	pET46lic	pET3D	p3NH
Protease Site	Pre3C	TEV	Pre3C
Antibiotic Resistance	Ampicillin	Ampicillin	Kanamycin
Tags and Fusions	N-terminal His_6 tag and suGFP	N-terminal His_6 tag	N-terminal His_6 tag
Cloning Strain	Top10	Top10	Top10
Source	Invitrogen	Invitrogen	Invitrogen
Expression strain	Rosetta2 (DE3) pLysS	Rosetta2 (DE3) pLysS	BL21 (DE3)
Antibiotic Resistance	CAM	CAM	-
Source	Merck	Merck	Sigma Aldrich

3.3 Plasmid amplification

To make new Δ91-FATZ-1-GFP, α-actinin-2-Neeck and full-length (FL) ZASP plasmid stocks, the plasmids were amplified by cloning. The amplification process is identical for all constructs except for the antibiotics used during overnight culture growth.

For the heat-shock transformation, approximately 100 nanograms (ng) of respective plasmid was added to 100 microliters (µL) of chemically competent Top 10 cells. The cells were incubated for 20 min (minutes) on ice, heat-shocked for 40 sec (seconds) at 42 °C on heat-block and incubated for 5 min on ice to close the pores. Transformed cells were given 900 µL of LB and grown for 1 hour at 37 °C at 400 rounds per minute (rpm) (Eppendorf Thermomixer comfort). Next, cells were centrifuged for 3 min at room temperature, 3k (3000) rpm (Eppendorf 5425 with FA-24x2 rotor). The excess LB of 900 µL was removed and the cell pellet was resuspended. Cell suspension was spread on antibiotic-selective agar plates and incubated overnight (o/n) at 37°C (MMM Ecocell). Control plates of cells without the plasmid were subjected to the same procedure.

Next, to grow an overnight culture, 10 milliliters (ml) of LB medium supplemented with the respective antibiotics was inoculated with a single colony from the selective plate. Cells were grown o/n at 37 °C at 220 rpm (Innova 440 Incubator Shaker). Plasmid DNA was purified with NucleoSpin™ Plasmid DNA purification kit protocol with one minor change: the elution volume was reduced to half, aiming for a higher stock concentration (Macherey-Nagel, September 2022/Rev. 13). The plasmids were stored at -20 °C.

3.4 Transformation

Plasmids were heat-shock transformed into their respective chemically competent *Escherichia coli (E. coli)* expression strains following the protocol for Top 10 cells in Chapter 3.3. Δ91-FATZ-1-GFP and α-actinin-2-Neeck encoding pET-based plasmids were transformed into Rosetta 2(DE3)-pLysS cells, which carry rare codon tRNAs to enhance eukaryotic protein expression. The second plasmid of Rosetta 2(DE3)-pLysS strain supplies CAM resistance for additional selection and expresses T7 lysozyme to suppress the basal T7 RNA-polymerase activity until induction (Kopanic *et al.*, 2013). ZASP encoding p3NH plasmid was transformed into BL21(DE3) cells.

3.5 Protein Expression

The contents of the growth medium and reagents used are listed in Table 3. The appropriate antibiotics were used in every step of expression involving growth media (Table 6). Total expression volume for each protein was 5 liters (L).

3.5.1 Δ91-FATZ-1-GFP Expression

To make an overnight culture, 100 ml of LB medium containing appropriate antibiotics was inoculated with multiple colonies from the Δ91-FATZ-1-GFP transformation plate and cells were grown o/n at 220 rpm and at 37 °C (Innova 440).

In a total expression volume of 5 L, each liter of LB medium was inoculated with 17.5 ml of overnight culture. Δ91-FATZ-1-GFP expressing cells were grown at 37 °C, 160 rpm until an OD_{600} of 0.8 was reached, then expression was induced with 1 mM IPTG (Sartorius Certomat BS-1). Induced cells were grown further for 5 h at 37 °C, 160 rpm. Finally, all cells were harvested by centrifugation for 40 min at 4 °C, at 5k rpm using the fixed-angle rotor R9A2 (Hitachi CR22N) and their pellets were stored at -70 °C.

3.5.2 α-actinin-2-Neeck Expression

For the α-actinin-2-Neeck culture, 20 ml of LB was inoculated with multiple colonies from the transformation plate and cells grown for 7 h at 37 °C. α-actinin-2-Neeck was overexpressed in ZYP 5052 autoinduction medium that contains both glucose and lactose. As glucose is depleted, lactose becomes the primary source and is converted to allolactose that induces the lac operon without the need for IPTG (Studier, 2005). Each litre of ZYP 5052 medium was inoculated with 1 ml of culture. The cells were grown o/n at 30 °C, 160 rpm and harvested as described for Δ91-FATZ-1-GFP.

3.5.3 ZASP Expression

To make an overnight culture expressing ZASP, 20 ml of LB medium was inoculated with few colonies from the transformation plate and cells were grown o/n at 37 °C at 220 rpm (Innova 440). To overexpress ZASP, each litre of autoinduction medium was inoculated with 1 ml of ZASP preculture. ZASP expressing cells were grown o/n at 37 °C, 150 rpm. Cells were harvested and stored as described for Δ91-FATZ-1-GFP.

3.6 Protein Purification

The buffers and protein purification equipment used in this study are listed in Tables 1 and 2 respectively. After each step of purification, the fraction identity and purity were evaluated by 12% SDS-PAGE. For chromatography, all buffers were filtered with a 0.45 µM membrane and degassed before use. Eventually, all proteins were stored at ~1 mg/ml concentration.

3.6.1 Δ91-FATZ-1-GFP Purification

Initially, Δ91-FATZ-1-GFP cells dissolved in lysis buffer without urea, a pinch of DNAse I, 100x Protease Inhibitor Cocktail in addition of PMSF on a magnetic stirrer. The dissolved cells were lysed using a pre-cooled cell disruptor at1.9 megabar (Mbar) (Constant Systems LTD). Cell lysates were centrifuged for 40 min at 4 °C, 18k rpm (Hitachi CR22N with R20A2 fixed angle rotor). Since Δ91-FATZ-1-GFP is in the insoluble fraction without urea, the first cell pellet was solubilized in its Resuspension Buffer (Table 2) containing 4 molar (M) urea and centrifuged again under the same conditions. The soluble fraction now containing Δ91-FATZ-1-GFP was diluted with its lysis buffer to reduce urea concentration down to 2 M to start protein purification with IMAC.

To avoid overloading, the unfiltered cell lysates were loaded onto two tandem-attached and Buffer A (Table 2) pre-equilibrated 5-ml HisTrap FF Crude columns. First, the columns were washed with 10 column volumes (CV) of Buffer A to remove any non-specifically bound proteins. The protein was eluted with 10 CV of Buffer B containing 250 mM imidazol in one-step fill (100%) with a flowrate of 5 ml/min and was collected in a 96-well plate. Fractions containing Δ91-FATZ-1-GFP were pooled and dialyzed o/n at 4 °C against ResQ Buffer A using a 12-14 kDa cut-off membrane (Spectra/Por 4).

Dialyzed Δ91-FATZ-1-GFP was further purified based on its charge by AEX (anion exchange) chromatography on a 6-ml ResQ column pre-equilibrated with the saltless ResQ Buffer A with pH 8 (Table 2). Δ91-FATZ-1-GFP was purified applying a 2-step linear gradient of ResQ Buffer B with 20 CV (0 to 30%) and 10 CV (30 to 60%) followed by a high salt wash step with 5 CV (100%) of Buffer B. The absorbance was monitored at 280 nm simultaneously with the GFP excitation maximum at 488 nm. Desired Δ91-FATZ-1-GFP fractions were dialyzed o/n at 4 °C against SEC Buffer A9 containing 50 mM Arginine to gently exchange the buffer. After dialysis, precipitation in the sample was removed by centrifugation in 25-ml concentrators (Vivaspin 200) for 10 min at 3k rpm at 4 °C (Eppendorf 5810 R with A-4-62 rotor).

Finally, Δ91-FATZ-1-GFP with a MW of 50.5 kDa was purified by SEC on a HiLoad 26/600 Superdex 200 column. The protein was eluted in 1.5 CV SEC Buffer A9 with a flow rate of 2 ml/min. After pooling the fractions of choice based on SDS-PAGE, concentration was determined using the A_{280} %0.1 (theoretical absorbance at 280 nm, 0.1% concentration) with NanoDrop (Table 6). For storage at -70 °C, proteins were concentrated to ~1 mg/ml in concentrators (Vivaspin 20) with a 10-30 kDa MW cut-off at 4 °C, 9k rpm (Eppendorf 5427 R with FA-45-30-11 rotor) and were flash-frozen in liquid nitrogen. The purified construct has an N-terminal His_6-tag.

3.6.2 α-actinin-2-Neeck Purification

α-actinin-2-Neeck cell extract was dissolved in its lysis buffer containing 0.5% Triton X-100 with DNAse I, 100x Protease Inhibitor Cocktail and PMSF. Next, the dissolved extract was sonicated three times for 3 min (50% amplitude, 1 s Pulse on, 1 s Pulse off) with a sonicator (Sonoplus, Bandelin Electronic). After sonication, the lysate was centrifuged for 40 min at 4 °C, 18k rpm to remove cell debris. The supernatant was used for IMAC.

α-actinin-2-Neeck was purified by IMAC using two tandem-attached 5-ml HisTrap FF crude columns, using a two-steps elution: 5 CV from 0 to 50% and 5 CV 50 to 100% in Buffer B with a flowrate of 5ml/min. To remove the N-terminal His_6-tag, a step required for fluorescent labelling later, α-actinin-2-Neeck was dialyzed o/n at 4 °C with TEV protease in 1:20 (protease to protein) ratio against its Cleavage Buffer (Table 2). After cleavage, the sample was purified by reverse HisTrap (same method as the IMAC) to remove the uncleaved Neeck and the protease, residual His_6-tags and the protease. Cleaved α-actinin-2-Neeck was collected in the wash or flow-through fractions. The sample was diluted 1 to 5 in its ResQ Buffer A to reduce salt concentration and further purified by AEX chromatography using a two-step linear gradient 20 CV with 30% and 5 CV of 60% ResQ Buffer B. Next, α-actinin-2-Neeck was purified by SEC on a HiLoad 26/600 Superdex 200 column in 1.5 CV SEC Buffer A9 and a flowrate of 2.6 ml/min. Finally, the concentration was determined as described for Δ91-FATZ-1-GFP.

3.6.3 ZASP Purification

After dissolving the ZASP pellet in its lysis buffer with a pinch of DNAse I and 100x Protease Inhibitor Cocktail, cell extract was sonicated three times for 3 min (50% amplitude, 1 s Pulse on, 1 s Pulse off). Cell lysates were centrifuged for 40 min at 4 °C, 18k rpm and the supernatant was collected for IMAC. ZASP was purified by IMAC on two tandem-attached 5-ml HisTrap FF crude columns. The loaded column was washed with 20 CV of its Buffer A (Table 2)

and the protein was eluted with a linear gradient from 0 to 100% Buffer B in 20 CV. ZASP was kept soluble in denaturing guanidium hydrochloride (GuHCl) buffers, where protease cleavage does not work. Thus, the His_6-tag was kept on ZASP during purification. For SDS-PAGE, samples to image were dialyzed into urea before staining with SDS-dye and spinned down to remove any aggregates it might form with GuHCl. After IMAC, ZASP was applied directly onto pre-equilibrated HiLoad 26/600 Superdex 200 column for SEC and eluted in 1.3 CV of its SEC buffer with a flowrate of 2 ml/min.

ZASP has a pI of 9.17 (Table 6). To refold ZASP after SEC, a 5-step acidic serial dialysis with a stepwise buffer exchange was set up, where GuHCl is gradually replaced with urea and the urea amount is gradually reduced to zero. This gave ZASP enough time to adjust to folding conditions. Each dialysis step took place at 4 °C for a day, in 4 liters of buffer with renewal of the dialysis membrane every second day. At the final step of dialysis, protein stabilized in its phosphate buffer. See Table 1 for the list of buffers. Following the refolding procedure, the protein concentration was determined by absorption at 280 nm on NanoDrop as described for Δ91-FATZ-1-GFP. ZASP was flash frozen in liquid nitrogen for storage at -70 °C.

3.7 Fluorescent labelling of α-actinin-2-Neeck and ZASP-FL

To observe the *in vitro* colocalization of Z-disc proteins α-actinin-2-Neeck and ZASP with Δ91-FATZ-1-GFP condensates under the confocal microscope, Neeck and ZASP were distinctly fluorescently labelled. The materials used for labelling and detailed information on fluorescent dyes are given in Tables 4 and 5 respectively. α-actinin-2-Neeck and ZASP were labelled N-terminally with ATTO 680 and ATTO 565 dyes respectively, using a sortase-mediated reaction. The sortase conjugates a peptide probe carrying the sortase recognition motif (LPTGX) and a fluorophore of choice to an exposed N-terminal glycine (Gly) of the protein (Theile *et al.*, 2013). The free Gly on the N-terminus of α-actinin-2-Neeck and of ZASP resulted from the TEV- and Pre3C protease cleavage respectively.

3.7.1 α-actinin-2-Neeck labelling

For a ~200 µl labelling reaction, cleaved α-actinin-2-Neeck carrying an N-terminal glycine was thawed on ice and concentrated to ~20 µM. The protein was then incubated with Sortase A (1:1 molar ratio) and 0.3 mM of ATTO 680-labeled peptide o/n at 4 °C under rotation and exclusion of light (Table 4). This step can be done in room temperature (RT) for faster results. To remove the free dye, labelled peptide and sortase by SEC, the sample was loaded on a Superdex 200 Increase 10/300 GL column using a 500 µl-loop and eluted

with 1.3 CV in the SEC buffer with a flowrate of 0.75 ml/min (Table 2), protected from light. The emission maximum of the dye at 680 nm was simultaneously monitored at the wavelength 698 nm. To select fractions containing fluorescently labelled Neeck, fractions were run on a 12% PAGE-gel and imaged before staining with Coomassie blue on Amersham™ Typhoon Biomolecular Imager (Cytiva). Successfully labelled α-actinin-2-Neeck fractions were pooled based both on the fluorescent and Coomassie-stained gel images. To determine the degree of labelling (DOL) and check the efficiency of labelling for α-actinin-2-Neeck with ATTO 680, Equation 1 from the product information sheet was used (ATTO-TEC, 2023):

$$DOL = \frac{c(dye)}{c(protein)} = \frac{A_{max}/\varepsilon_{max}}{A_{prot}/\varepsilon_{prot}} = \frac{A_{max} \cdot \varepsilon_{prot}}{(A_{280} - A_{max} \cdot CF_{280}) \cdot \varepsilon_{max}} \qquad \text{(Equation 1)}$$

Notably, the correction factor (CF_{280}) accounts for dye absorption at the protein absorption maximum of 280 nm. The absorbance at the absorption maximum of the dye (A_{max}) and of the protein (A_{280}) was measured with NanoDrop UV-Vis spectrometry after diluting the solution for an absorbance below 2 for accuracy. The theoretical extinction coefficient of the Neeck monomer (ε_{prot}) is given on Table 6. The extinction coefficient at the absorption maximum (ε_{max}) and CF_{280} of the fluorescent dye were provided by the manufacturer (Table 5). Finally, α-actinin-2-Neeck-ATTO 680 was concentrated to 20 µM (Vivaspin 20) and aliquoted for imaging experiments. Aliquots were flash frozen and stored at -70 °C.

3.7.2 ZASP labelling

To obtain a free N-terminal glycine on ZASP, protein was first subjected to Pre3C-protease cleavage. ZASP was thawed on ice and dialyzed against its Pre3C Cleavage Buffer (Table 2) in 3.5 kDa cut-off membranes o/n at 4 °C for buffer exchange. On the following day, Pre3C protease was added to ZASP sample in 1:50 ratio and the sample was further dialyzed o/n at 4 °C. For a ~250 µl labelling reaction, cleaved ZASP was concentrated up to ~70 µM and incubated o/n at 4 °C under rotation with the Sortase A (1:1 molar ratio) and 0.3 mM of ATTO 565-labeled peptide, protected from light. The free dye, labelled peptide and sortase were removed by SEC in 1.5 CV of the Buffer A9 with a flowrate of 0.8 ml/min on a Superdex 75 Increase 10/300 GL column while monitoring the dye absorption at 564 and emission at 590 nm. It is worth emphasizing that after the SEC step, ZASP-ATTO 565 is in the same buffer system as, α-actinin-2-Neeck-ATTO 680 and Δ91-FATZ-1-GFP (Table 2). To identify the labelled fractions, fractions were run on a 12% PAGE-gel and imaged on Amersham Typhoon imager before being stained with

Coomassie blue. According to the fluorescence and PAGE-gels, the fractions were pooled and the DOL was determined in the same way described for Neeck-ATTO 680 (Equation 1). Finally, ZASP-ATTO 565 was concentrated back to ~70 µM, then aliquoted and flash frozen for storage at -70 °C.

3.8 Design of Experiment – Δ91-FATZ-1-GFP biomolecular condensates with a second Z-disc protein

To systematically test the individual effect of α-actinin-2-Neeck and ZASP concentration on Δ91-FATZ-1-GFP condensates, Design of Experiment (DoE) approach was taken. DoE is a statistics-based active regression modelling technique to minimize the number of trials in an experiment (Rüttimann & Wegener, 2015). In this study, we treat the experimental output as the response to 2 independent factors (first factor: Δ91-FATZ-1-GFP concentration, second factor: α-actinin-2-Neeck-ATTO 680 or ZASP-ATTO 565 concentration). The experimental output is the condensate count, condensate size and overall area covered by condensates, each quantified from 2D confocal images. For the sake of clarity, potential effects of α-actinin-2-Neeck and ZASP concentration on condensates was tested separately and not both at the same time.

The experimental range of suitable concentrations was determined by two limitations: the highest attainable concentrations of proteins and the total reaction volume. The total reaction volume was selected as 8 µl, for accurate pipetting and resourcefulness. The highest attainable concentrations were determined by concentrating each protein as described before and their available molar ratios. It is general practice in DoE to use 'coded factors' for consistency and to emphasize the equidistance as shown in Table 7: +1 as 'high', -1 as 'low' and 0 as the 'intermediate' concentration. The upper limit (+1) was determined based on the protein's solubility and the total reaction volume of 8 µl, which restricts the possible volume combinations. The lower limit for Δ91-FATZ-1-GFP (-1) was set as the concentration at which condensates were reliably visible under the confocal microscope at the 10th minute. The center point (0) is the middle point of the two selected boundaries.

JMP software (Student Subscription 17.2.0) was used to create a custom design of the 2-factor experiment with 4 center points and 3 replicates. The design has a power of 0.888 whilst a power of 0.80 was aimed as a commonly accepted threshold (Pollard *et al.*, 2019) Finally, the resulting design is a list of conditions in randomized order (Table 8) to experimentally investigate the effect of increasing concentration of the second Z-disc protein on Δ91-FATZ-1-GFP condensates.

Table 7: DoE coded factors and the corresponding biological values.

Coded Factor	Δ91-FATZ-1-GFP [µM]	Neeck-ATTO 680 [µM]	ZASP-ATTO 565 [µM]
+1 (high)	130	12	20
-1 (low)	70	0	0
0 (intermediate)	100	6	10

Table 8: 2-factor DoE experiment with triplicates and 4 center points. The condition column represents quantity of protein concentrations as coded factors. In condition (**+1**, 0), **+1** represents c(Δ91-FATZ-1-GFP) and 0 represents c(second Z-disc protein). CP stands for "center point". The asterisk (*****) indicates missing data points.

Slide/Run	Condition	Δ91-FATZ-1-GFP [µM]	Neeck-ATTO 680 [µM]	ZASP-ATTO 565 [µM]
1	(**-1**, +1)	**70**	12	20
2	(**-1**, +1)	**70**	12	20
3	(**+1**, -1)	**130**	0	0
4	(**+1**, +1)	**130**	12	20
5	CP (**0**, 0)	**100**	6	10
6	(**-1**, -1)	**70**	0	0
7	CP (**0**, 0)	**100**	6	10
8	(**+1**, -1)	**130**	0	0
9	CP (**0**, 0)	**100**	6	10
10	(**+1**, +1)	**130**	12	*****20
11	(**-1**, -1)	**70**	0	0
12	CP (**0**, 0)	**100**	6	10
13	(**-1**, +1)	**70**	12	*****20
14	(**-1**, -1)	**70**	0	0
15	(**+1**, +1)	**130**	12	*****20
16	**(+1, -1)**	130	0	*0

3.9 Confocal imaging of Δ91-FATZ-1-GFP biomolecular condensates

3.9.1 Sample Preparation

On the previous day of imaging, Δ91-FATZ-1-GFP was concentrated up to 260 µM stock and stored o/n at 4 °C. For accurate concentration determination, a 10-15-fold diluted aliquot of the sample outside of phase-separation regime was measured. α-actinin-2-Neeck-ATTO 565 or ZASP-ATTO 565 was thawed on ice half an hour before the experiment. The solution of the desired concentration with a final volume of 8 µl per slide was prepared right before imaging: proteins with the SEC Buffer A9 (Table 2) were mixed by pipetting in PCR-strip tubes on ice in calculated ratios, resuspended 3 times with pipette and pipetted directly onto a clean coverslip at (RT). The glass slide with sticky spacer was gently placed onto a coverslip and incubated for 10 min at 37 °C on the pre-heated heating platform above the objective. The spacer allows the condensates to move without compression and 10 min is enough for them to settle on the cover slip. See Table 1 for the list of equipment used for imaging. A cartoon of microscopy preparation is given in the Figure 8.

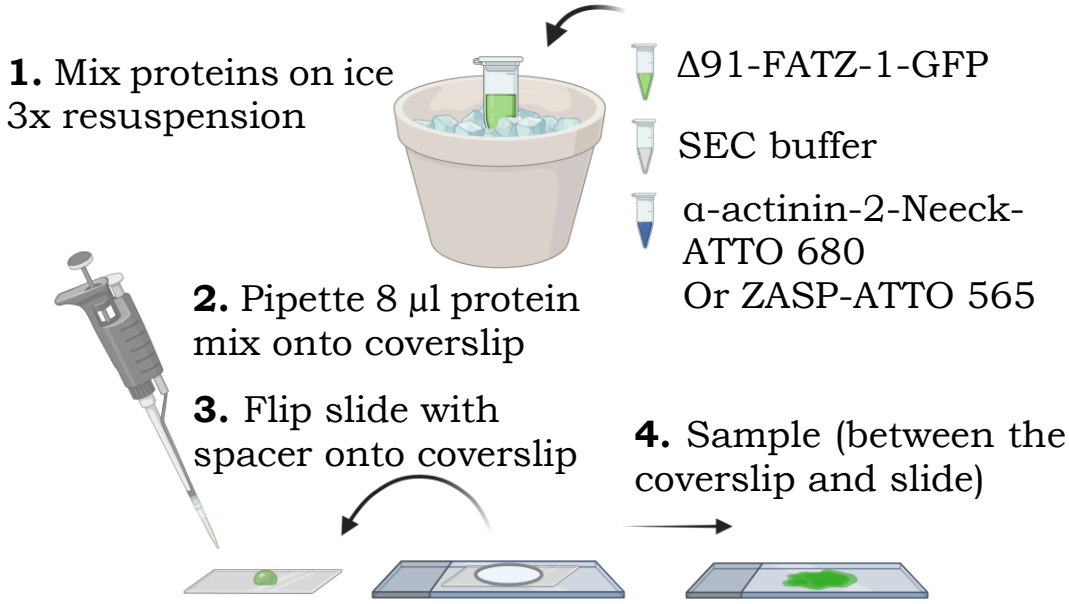

Figure 7: Sample preparation for droplet imaging using confocal microscope. The proteins are mixed on ice and resuspended 3-times in the given order (1). Next, sample is pipetted onto a clean coverslip that is at RT (2). The microscopy glass slide that has the sticky spacer on it is then gently placed onto the cover slip (3). Finally, the sample is between the glass slide and coverslip (4). Without inverting and shaking, the slide is then placed onto the heating platform of the confocal microscope. The figure was made using BioRender.

3.9.2 Condensate Imaging with Δ91-FATZ-1-GFP and α-actinin-2-Neeck

For imaging the 2-dye protein system *in vitro* at 37 °C in high resolution we used a Zeiss LSM 980 confocal microscope equipped with a 63x/1.4 objective and a heating platform. Two dimensional (2D) images of size 84.53x84.53 microns (1.5 crop) of the distinctly labelled proteins were taken using the confocal module and setting up multiple channels utilizing different lasers. See Table 1 for information on microscopy equipment.
After 10 minutes of incubation for droplets to settle on the glass with the lid on the heating platform on the microscope to control humidity at 37 °C, 3 images were taken from random field-of-views on a single slide, representing technical replicates. The DoE run with random field-of-views listed in Table 8 was repeated 3 times, resulting in 9 slides (27 images) per condition. Overall, experiments done on random field-of-views encompass at least 3 biological replicates stemming from different purification and labelling batches of Neeck and 2 purifications of Δ91-FATZ-1-GFP.

3.9.3 Mid-Zone Imaging with Δ91-FATZ-1-GFP and α-actinin-2-Neeck

For a better understanding of the condensate distribution within the sample and to uncover if there is any bias on the surface conditions, imaging was repeated only within the middle-zone of the slide, yet only for one complete DoE run (Table 8, Figure S1). Additionally, to test if there is an uneven heat distribution along the slide, the temperature on the glass slide (inside the heating platform) was measured by a Data Logger (TC-08 Pico Technology) attached to two thermocouples placed on the flip side of the slide, one detector contacting the middle and the other the outer edge of the sample chamber. The Pico Logger was kindly provided by the Juffman Lab (Max Perutz Labs).

3.9.4 Preliminary Imaging with Δ91-FATZ-1-GFP and ZASP

The effect of increasing ZASP concentration on Δ91-FATZ-1-GFP condensates was investigated using the same methodology as described for mid-zone imaging of Neeck in Chapter 3.9.3. The tested concentrations of ZASP and Δ91-FATZ-1-GFP are listed in Table 8. A single DoE experiment was conducted using one biological replicate, meaning imaging experiments were done with the same purification and labelling batch of ZASP-ATTO 565.

3.10 Turbidity Assay with Δ91-FATZ-1-GFP and α-actinin-2-Neeck

To compare the output of condensate images with another physical parameter of LLPS, a turbidity assay with Δ91-FATZ-1-GFP (His_6-tag on) and unlabeled Neeck (His_6-tag off) was performed. An experiment with wild-type α-actinin-2

and a different FATZ-1 construct (His_6-tagged Δ91-FATZ-1, without GFP) was done in 0 mM Arginine buffer previously in our lab, providing an opportunity to compare construct behaviors under LLPS (Sponga *et al.*, 2021). In this study, Δ91-FATZ-1-GFP concentration was held constant at 70 µM, since this concentration is comparable to the one tested before (65 µM) and is the same as the microscopy experiments. Conditions described in Table 9, each with a total reaction volume of 300 µl, were prepared on ice. For triplicates, the 90 µl of each sample was pipetted onto 96-well plate (Greiner) on ice three times. SEC Buffer A9 (Table 2) absorbance was also measured in triplicate as a negative control for LLPS. Turbidity at 600 nm was measured at 37 °C with 20 sec intervals, 1440 rpm shaking for 90 min on the microplate reader with the lid off (Tecan Spark).

Table 9: Turbidity assay scheme.

	Condition
1	70 µM Δ91-FATZ-1-GFP
2	70 µM Δ91-FATZ-1-GFP with 2 µM Neeck
3	70 µM Δ91-FATZ-1-GFP with 4 µM Neeck
4	70 µM Δ91-FATZ-1-GFP with 6 µM Neeck
5	70 µM Δ91-FATZ-1-GFP with 8 µM Neeck
LLPS negative control	SEC Buffer A9

3.11 Data Analysis and Statistics

To measure the condensate count, size and area covered by them, the 2D confocal condensate images were analyzed by the Fiji software (ImageJ 1.54f). Each image taken from the Δ91-FATZ-1-GFP channel was converted into a binary and the threshold for intensity of the binary image was set manually for each image, to exclude out of focus droplets and with a cut-off at 10 pixels, to avoid out of focus and remnant pixels. The count and size (in micron-squared) of the droplets were calculated automatically by the software. The area covered by condensates was calculated from the total area of droplets summed up, divided by the image area and converted to percentages. All measurements were visualized either by Python (Version 3.1), Microsoft Excel (Version 1808), or GraphPad Prism (Version 10.3.1). Leverage analysis, which can capture the significant effects on the experimental outputs like the count, size or area was done on JMP software (JMP Statistical Discovery, 2024). Normality and significance tests (Kruskal Wallis ANOVA) comparing datasets were done using GraphPad using a 0.05 alpha. P-values are given in APA-style.

4 Results

4.1 Protein Chromatogramms

4.1.1 Purification of Δ91-FATZ-1-GFP

Δ91-FATZ-1-GFP was purified by IMAC, AEX and SEC (Figure 9A-C). It is possible to re-apply the flow-through during the first two methods to increase the protein yield slightly. The SEC elution peak is at 182 ml on the HiLoad 26/600 S200 pg column (Figure 9C). The average yield of a 5-L protein expression was 30 mg (milligrams) of N-terminal His_6-tagged Δ91-FATZ-1-GFP.

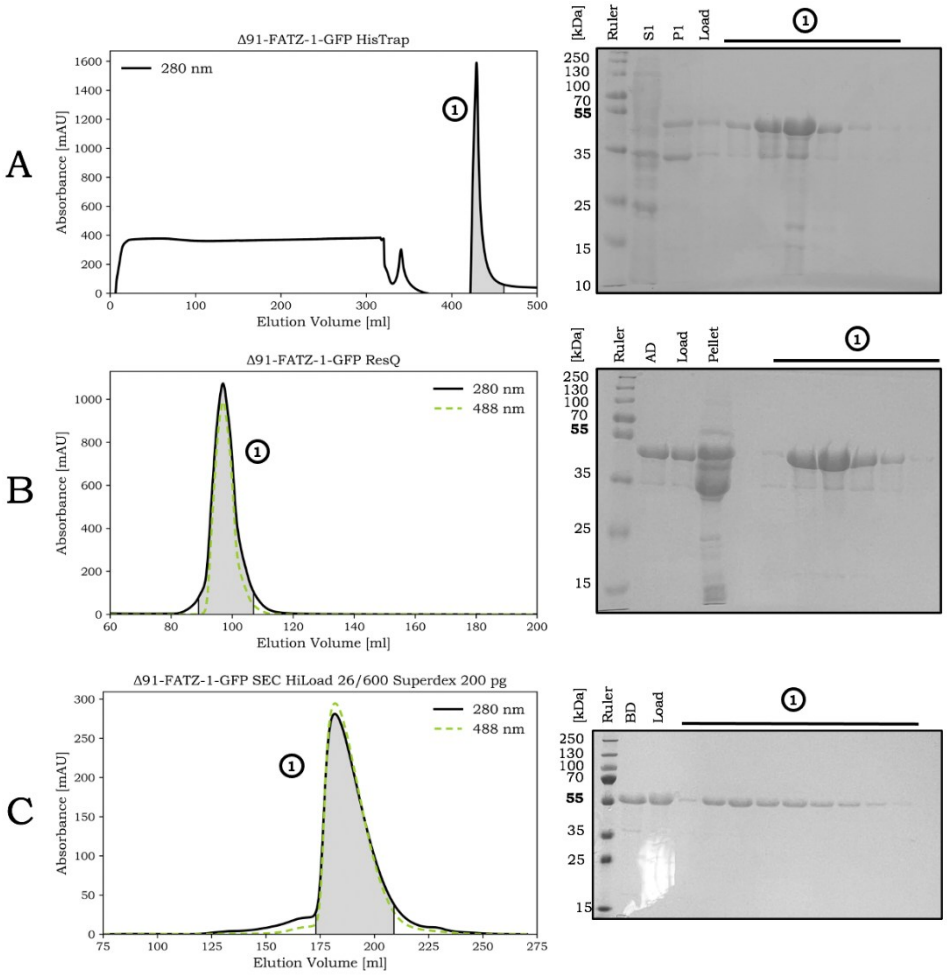

Figure 8: Purification of Δ91-FATZ-1-GFP (MW: 50.5 kDa). All chromatograms displayed a singular protein peak. The buffer exchange/dialysis steps were monitored by 12% SDS-PAGE as well. 8A: IMAC. S1 stands for first lysate supernatant and P1 stands for first pellet, showing solubilization of protein. 8B: AEX. AD stands for After Dialysis. 8C. SEC. The elution peak is at 182 ml. In each gel image, each fraction has 4 µl and the marker 5 µl volume.

4.1.2 Purification of α-actinin-2-Neeck

All α-actinin-2-Neeck purification chromatograms are given in Figure 10. AEX chromatography significantly increased the purity before SEC. Finally, protein was purified by SEC on a HiLoad 26/600 S200 pg column and had the peak elution volume at 156-158 ml. The approximate yield of a 5-L expression was 20 mg of α-actinin-2-Neeck, enough for roughly 4 labeling reactions.

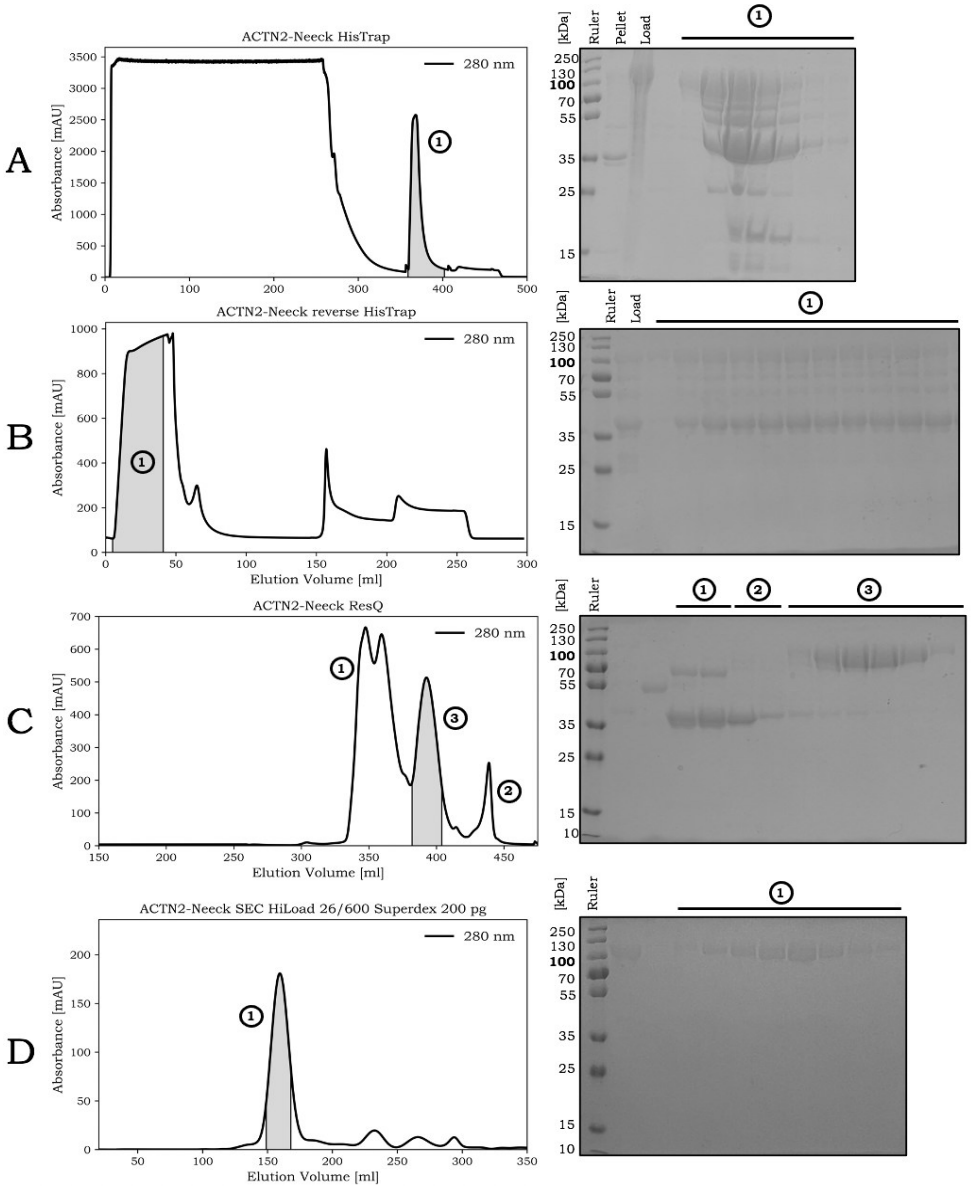

Figure 9: Purification of ACTN2-Neeck (MW: 207.8 kDa). 10A: IMAC. Protein elutes at 500 mM Imidazol. 10B: revIMAC. The flowthrough containing ACTN2-Neeck without the affinity tag was collected. 10C: AEX. AEX was able to remove the contamination at the 35 kDa band. Peak number 3 corresponds to the MW of monomer. 10D: SEC. The elution peak of ACTN2-Neeck is at 156-158 ml on this column. All 12% SDS-PAGE gels were loaded with 7 µl of the marker and fraction.

4.1.3 Purification of ZASP

ZASP was purified by IMAC followed directly by SEC, with the elution peak at 189 ml on the HiLoad 26/600 S200 pg column (Figure 11). The 3 M GuHCl buffer was replaced gradually by a urea buffer in a 5-step dialysis process successfully and with a negligible loss of protein quantity. As expected from previous experience yet still remarkably, 5 L of expression volume yielded approximately 120 mg of N-terminal His_6-tagged ZASP.

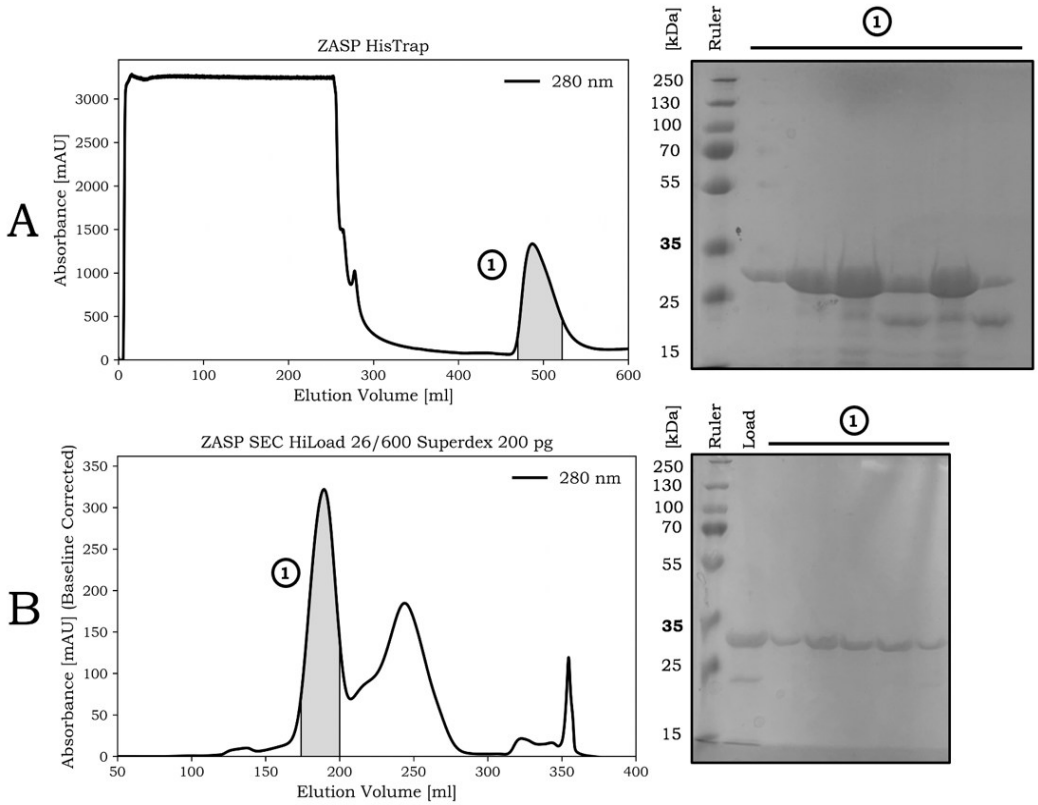

Figure 10: Purification of ZASP (MW: 33.2 kDa). 11A: IMAC. ZASP elutes at 500 mM Imidazol. 11B: SEC. SEC was able to purify ZASP to desired purity. Peak number 1 is corresponding to ZASP based on elution volume and the MW bands aligned on the gels. The elution peak is at X ml on this column. In each 12% SDS-PAGE gel, 7 µl marker and 10 to 12 µl of fraction volumes were loaded.

4.2 Fluorescent labelling of α-actinin-2-Neeck and ZASP

To image the Δ91-FATZ-1-GFP condensates in presence of the colocalizing Z-disc proteins, α-actinin-2-Neeck and ZASP were labelled N-terminally with fluorescent dyes using a sortase-mediated reaction, as described in Chapter 3.7.

4.2.1 α-actinin-2-Neeck labelling with ATTO 680

First of all, it was determined that this labeling reaction is more reliable in small-scale due to solubility and degradation issues. α-actinin-2-Neeck-ATTO 680 has the elution peak at 11-12 ml on the HiLoad Superdex 200 Increase 10/300 GL column (Figure 12). Each labeling reaction yielded roughly 0.5 mg of labeled protein. Meanwhile, concentrating the labeled α-actinin-2-Neeck in order to make stocks for imaging experiments results in reduction of protein amount down to a half.

The average DOL of seven α-actinin-2-Neeck-ATTO 680 labeling reactions is 58% (meaning 58% of possible sites were labelled) with a standard deviation (STD) of 30, which is sufficient for the imaging experiments.

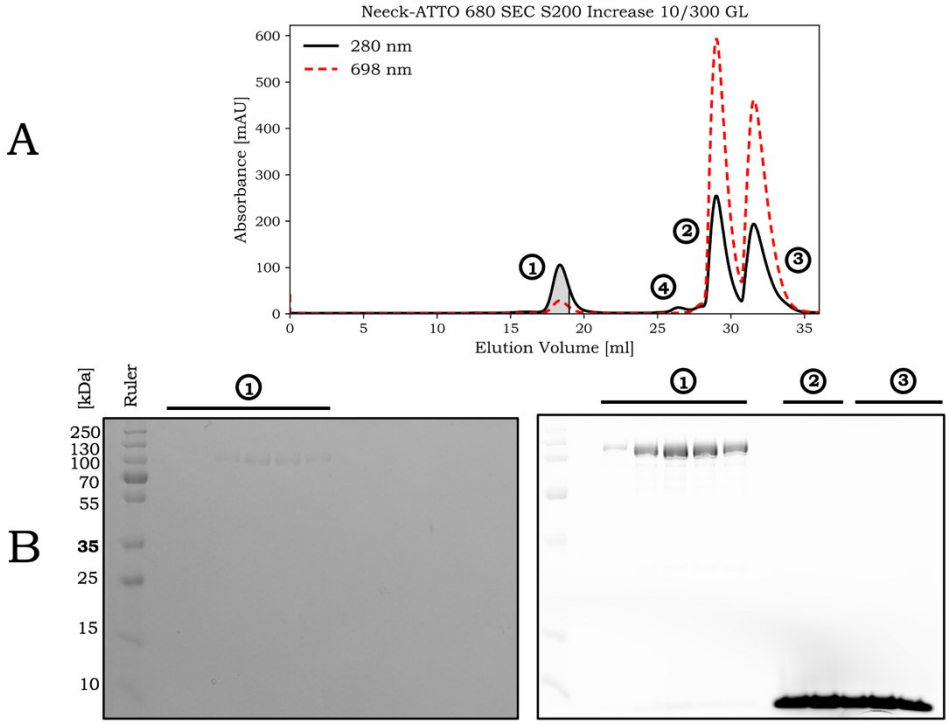

Figure 11: ACTN2-Neeck labelling with ATTO 680 dye. 12A: SEC. To purify ACTN2-Neeck-ATTO 680 from the free dye and sortase, SEC on a Superdex 200 Increase 10/300 GL column was used while monitoring the dye emission maximum at 698 nm. The elution volume around 11 ml corresponds to ACTN2-Neeck-ATTO 680 and fractions had the visible color by naked eye. Peaks number 2 and 3 appear to be the free dye. Peak 4 has no signal at 698 nm. 12B: The 12% SDS-PAGE gel (left) and its corresponding fluorescent image (right). The detector of fluorescence imager is stronger, and colors are contrasted. 7 µl of marker and 9 µl of each fraction was loaded onto gel. The MW of Neeck monomer is 103.9 kDa and the ATTO 680 dye is 1024 Da (See Table 4).

4.2.2 ZASP labelling with ATTO 565

ATTO 565 was conjugated to ZASP with the aforementioned sortase-mediated reaction, utilizing 70 µM ZASP, as ZASP was more tolerating to higher concentrations than α-actinin-2-Neeck. ZASP-ATTO 565 was purified by SEC using Superdex 75 Increase 10/300 GL column able to resolve the labeled ZASP (MW: 33.2 kDa) from the sortase (MW: 27.7 kDa). The average yield per reaction was 0.1 mg of labeled ZASP.
ZASP is extremely prone to degradation. However, ZASP-ATTO 565 stock concentrations of 70 to 100 µM were achieved and also evaluated by SDS-PAGE for intactness before imaging experiments. The degree of labeling for ZASP with ATTO 565 dye was constantly at 5%, which was entirely sufficient for confocal imaging purposes with current equipment.

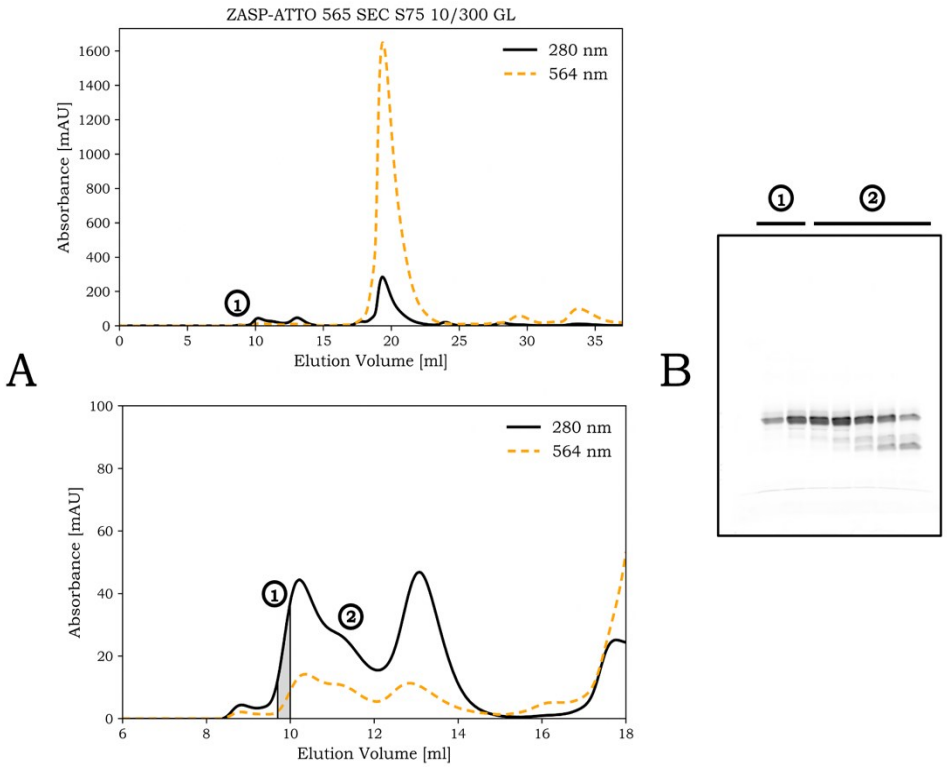

Figure 12: ZASP labeling with ATTO 565. 13A: SEC. ZASP-ATTO 565 was eluted in the SEC Buffer A9 on a Superdex 75 10/300 GL analytical column and the peak elution volume stands at 10 ml (top). The protein peak appears to have a shoulder (number 2) and contains mostly "degraded" ZASP (bottom: zoomed in section). Pooling only the best 1 to 2 fractions each labeling ensured quality and purity of the ZASP samples. 13B: The fluorescent image of the 12% SDS-PAGE gel. The stained gel image is missing, yet the MW of the thickest bands align with the ZASP MW (33.2 kDa). The "shoulder peak" number 2 appears to have strong degradation. 10 µl of fractions were loaded onto the gel.

4.3 Δ91-FATZ-1-GFP Biomolecular Condensates

To investigate how Δ91-FATZ-1-GFP condensates are influenced by increasing the α-actinin-2-Neeck and ZASP concentration, fluorescently tagged proteins in various concentrations were imaged with the confocal microscope following the DOE setup (see Materials and Methods). To quantify the droplets and detect potential differences between concentrations, the droplet count, size, and total area covered were measured from the 2D images of the GFP channel. See Figure S3 for all multiple pairwise comparisons.

4.3.1 Qualitative Δ91-FATZ-1-GFP concentration series

The threshold concentration at which the droplets are reproducibly visible at the 10th minute was assessed by imaging a Δ91-FATZ-1-GFP concentration series (Figure 14). Overall, area per condensate and overall area covered grows as the Δ91-FATZ-1-GFP concentration increases. At the 10th minute, with 40 μM Δ91-FATZ-1-GFP, no droplets were observed. Only at concentrations above 60 μM Δ91-FATZ-1-GFP, the droplets were reliably visible and dynamic. Clearly, the plane of focus for droplets also varied at high concentrations, influencing the measurements. Especially above 150 μM, the average droplet size exceeds 10 μm^2 and droplet count per image is reduced.

4.3.2 Δ91-FATZ-1-GFP condensates with increasing α-actinin-2-Neeck concentration

4.3.2.1 Random zones imaging with α-actinin-2-Neeck

Figure 15 shows the chosen 2D images of each tested condition. The composite images confirm the protein colocalization. The intensity of colors was not manipulated after images were taken and is dependent on manual adjustment of the microscope settings as well as the protein concentrations.

First, measured droplet distributions were tested for normality to apply appropriate statistics. While droplet size and overall area covered did not follow a normal/Gaussian distribution, droplet count measurements passed the normality test. Table 10 gives a brief statistical summary of random field-of-view droplet measurements. Within a defined image area, the count of the droplets is dependent on the size of the image and of the droplets. Because of this fact and due to the high number of categories to compare, following results focus more on the measured area per condensate.

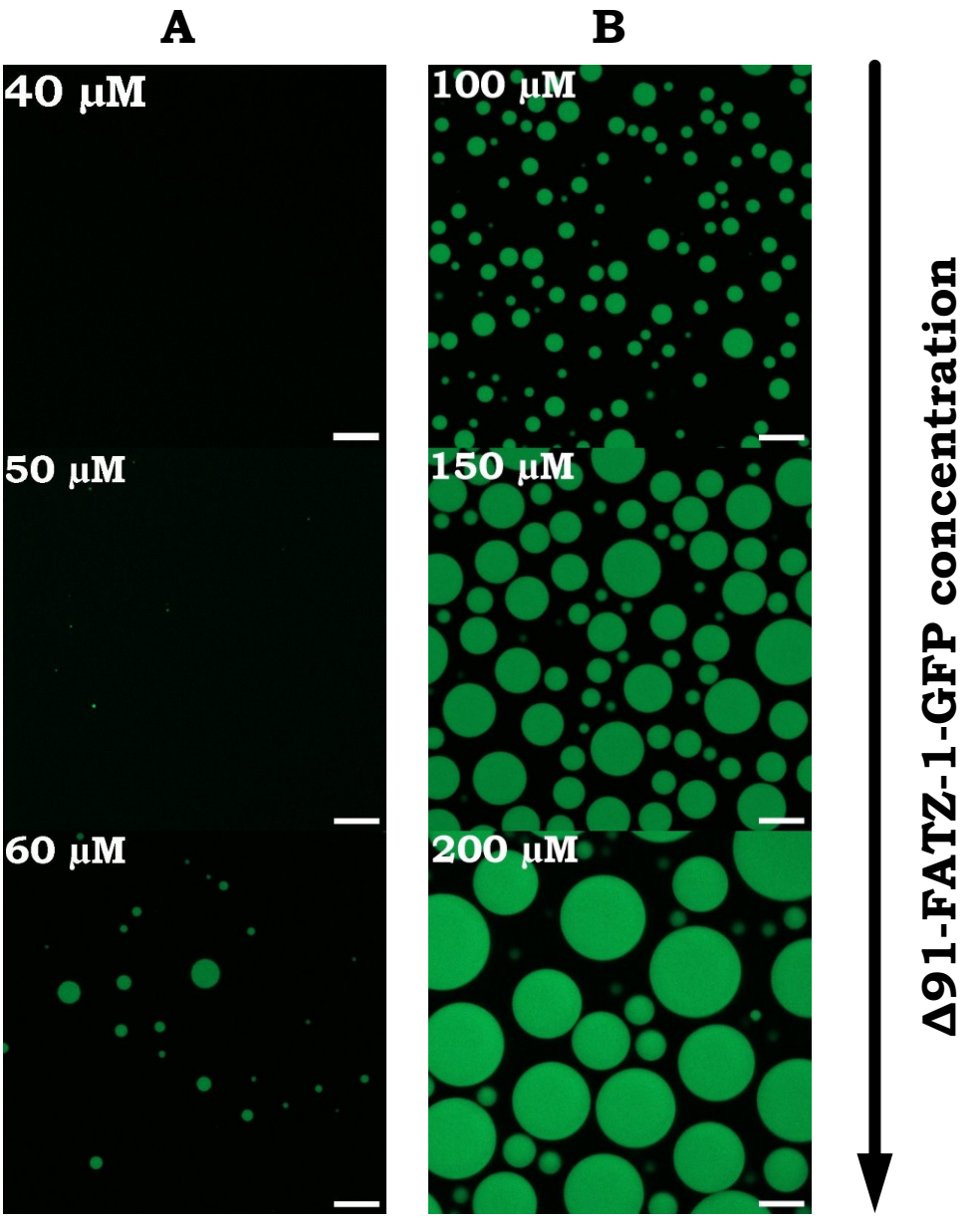

Figure 13: Representatively chosen confocal images of Δ91-FATZ-1-GFP concentration series. 14A: At 10th minute, droplets are visible above 50 µM, where a few smaller than a micron droplets are visible. 14B: Average droplet size grows proportionally to the Δ91-FATZ-1-GFP concentration. All images were taken at the 10th minute of incubation at 37 degrees. Image size: 84.53x84.53 µm. The scale bar is 10 µm.

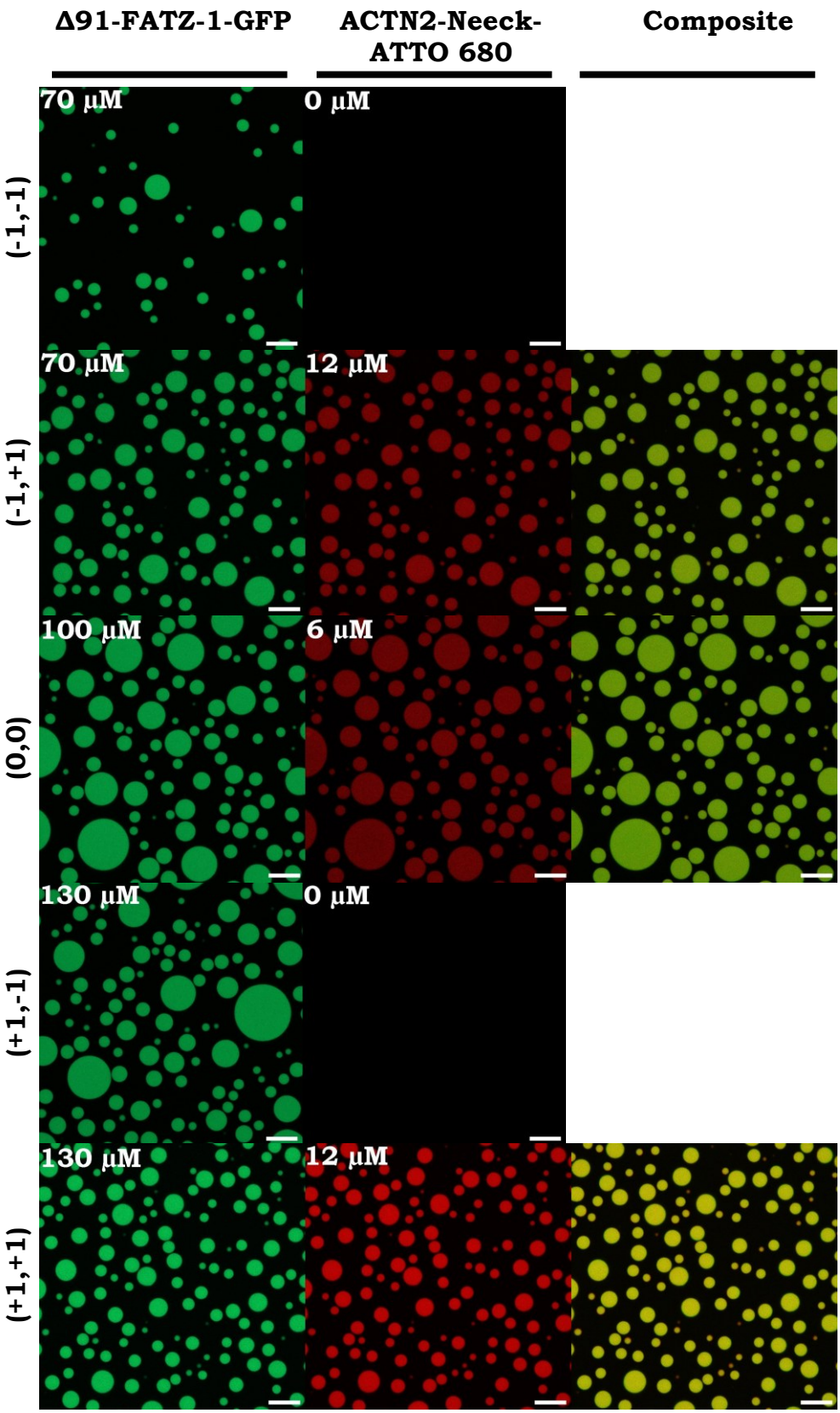

Figure 14: Confocal random field-of-view images of Δ91-FATZ-1-GFP condensates with ACTN2-Neeck at DoE concentrations. The images are randomly chosen and belong to a sample pool of at least 26 other images. The images were taken at 10th minute at 37 °C. Image size: 84.53x84.53 μm. The scale bar is 10 μm. The brightness and intensity of images were untouched.

Table 10: Δ91-FATZ-1-GFP with α-actinin-2-Neeck droplet size, count and area covered measurements obtained from random imaging experiments. Non-integer numbers were rounded for count.

Coded Condition	**-1, -1**	**-1, +1**	**0, 0**	**+1, -1**	**+1, +1**
Δ91-FATZ-1-GFP [µM]	**70**	**70**	**100**	**130**	**130**
ACTN2-Neeck [µM]	**0**	**12**	**6**	**0**	**12**
N	27	27	36	27	27
Size [µM]					
Minimum	5.775	3.310	9.456	17.87	11.99
Median	10.33	13.08	20.73	23.52	26.67
Maximum	22.31	23.35	38.23	36.47	46.78
Mean	11.98	13.39	20.59	25.59	28.43
SD	5.083	5.648	6.531	5.552	9,842
Count					
Minimum	32	63	69	70	54
Median	76	94	99	94	75
Maximum	166	149	127	109	118
Mean	89	100	100	91	79
SD	38.73	26.83	15.11	10.36	18.2
Total Area Covered [%]					
Minimum	6.171	5.732	12.12	27.38	20.42
Median	14.13	20.97	34.08	37.92	38.65
Maximum	36.85	39.04	42.94	50.39	50.35
Mean	15.31	19.68	32.19	38.35	36.4
SD	7.208	9.91	8.363	6.092	7.91

As the Δ91-FATZ-1-GFP concentration raises from 70 to 130 µM, several changes in droplet parameters occur. Figure 16 depicts the droplet size distributions and Figure 17 the covered area with their pairwise statistical comparisons. Overall, 130 µM Δ91-FATZ-1-GFP with 12 µM α-actinin-2-Neeck condition has the highest droplet size and spread (Table 10).

Between conditions 1 and 4, when the Δ91-FATZ-1-GFP concentration is raised from 70 to 130 µM in absence of α-actinin-2-Neeck, average size of condensates increases from 12 to 25.6 μm^2, corresponding to an approximately 2.1-fold (Table 10). The overall area covered by droplets increases 2.5-fold (from 15,3% to 38,3%). In presence of 12 µM α-actinin-2-Neeck, the size increase is again 2.1-fold (from 13.4 to 28.4 μm^2) and the total area covered by droplets increases 1.85-fold (19,7% to 36,4%) (Table 10, conditions 2 and 5). All of these changes are statistically significant. At the same time, the average droplet size increases slightly for both Δ91-FATZ-1-GFP concentrations upon addition of 12 µM α-actinin-2-Neeck, nevertheless not in a statistically meaningful way (conditions 1-2 and 4-5). The mean overall area covered by droplets also increases by a few percent without statistical significance. The droplet count per image does not show a trend yet it is intrinsically linked to the area per droplet and overall area covered by them (Figure S2). At the 10^{th} minute, while droplets have settled on the glass, fusion events are still ongoing and visible under the microscope (Figure S5).

Additionally, the leverage analysis for DoE setups revealed that the droplet size is solely influenced by Δ91-FATZ-1-GFP concentration and not by α-actinin-2-Neeck (Figure S7).

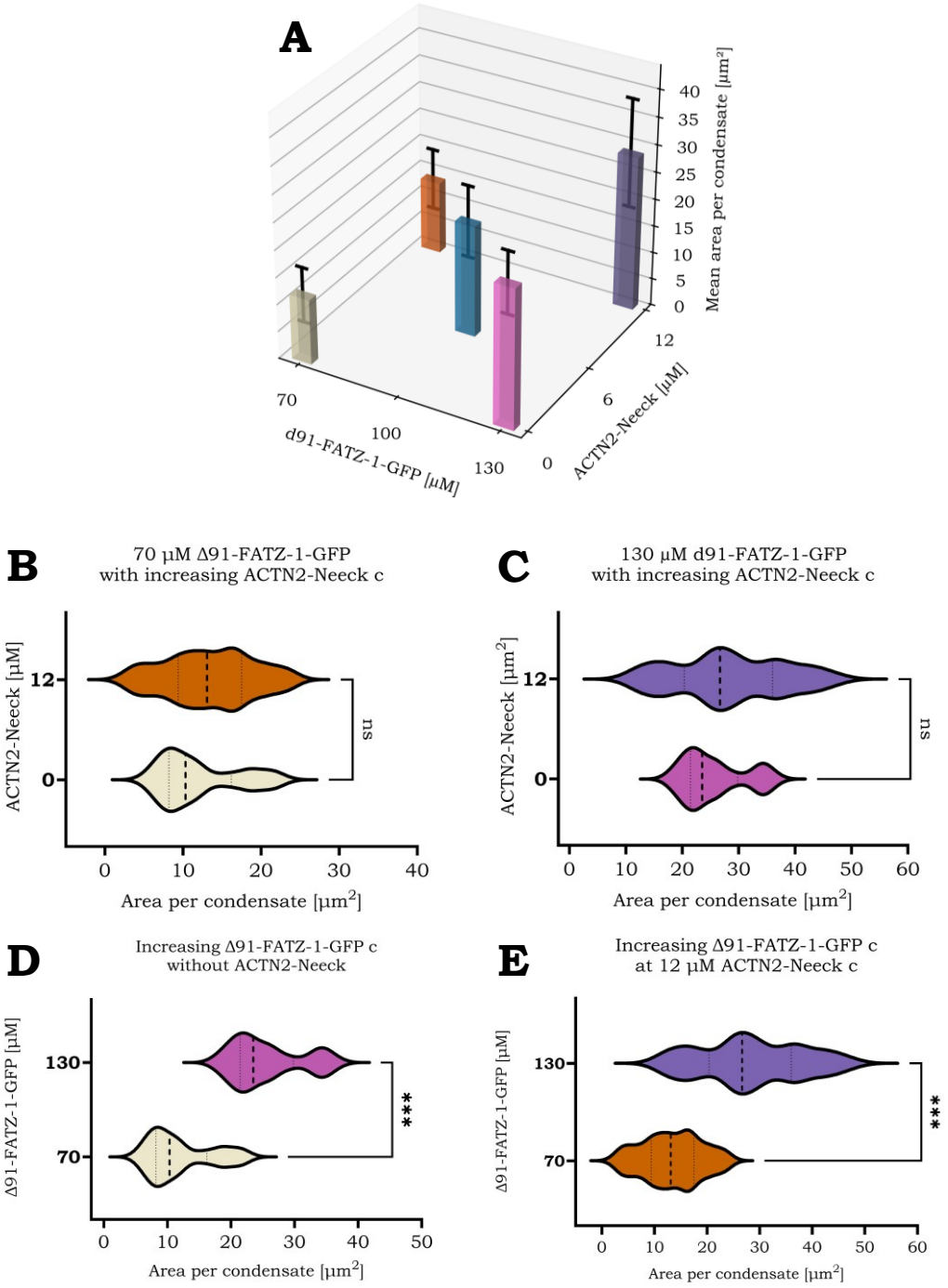

Figure 15: Droplet size measurements from random field-of-view images. 16A: 3D droplet size diagram. Droplet size seems to increase as the Δ91-FATZ-1-GFP concentration increases The bars depict the mean values and the error bars represent SD. 16B-C: There is no significant difference between condensate sizes at both constant Δ91-FATZ-1-GFP concentration. 16D-E: At constant ACTN2-Neeck concentration, the droplet size increases as Δ91-FATZ-1-GFP concentration increases. The significance was tested by ANOVA (p*** ≤ 0.001). The thick dashed lines represent the median value. Sample size is 27 for each and 36 for the center point (blue).

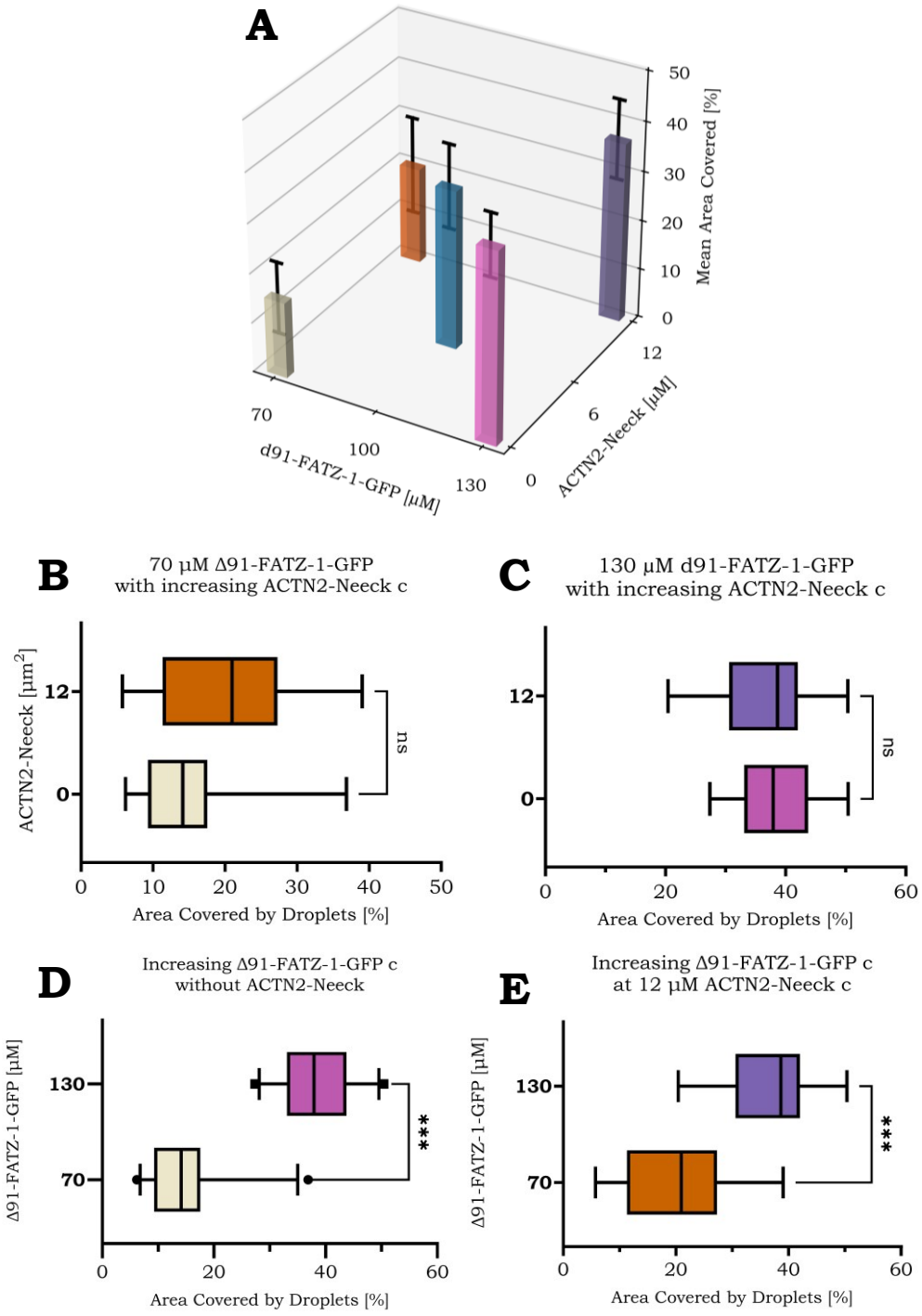

Figure 16: Total area covered by droplets from random field-of-view images. 17B-C: At constant Δ91-FATZ-1-GFP concentration of 70 and 130 µM, adding 12 µM ACTN2-Neeck does not cause a significant change in overall droplet area. 17D-E: As Δ91-FATZ-1-GFP concentration increases and ACTN2-Neeck is held constantly at 12 µM, droplet area covered gets higher. The significance was tested by ANOVA (p*** ≤ 0.001). Sample size is 27 for each and 36 for center point (blue).

4.3.2.2 Middle zone imaging with α-actinin-2-Neeck

Occasionally during imaging random zones on the slide, a visibly high variance of droplet distribution even within the same slide was observed, which made measurements hard to reproduce (data not shown). To understand if the droplets are uniformly distributed on a single slide and if image sampling and thus measurements are dependent on the field-of-view zones, a mini-experiment was done imaging only exactly the center/mid-zone of the slide (see Materials and Methods 3.9.3).

Additionally, to see if heat is distributed evenly along the slide, the glass slide temperature at the center of the sample and at the edges of the sample area were measured. Figure 18 shows the temperature measurement within the first 10 minutes of incubation at 37 °C. First of all, both temperature curves are nearly identical. Within 10 min, the temperature raises from the environment temperature (approximately 28 °C) to a final of 35.5 and 35.4 °C at the mid-zone and outer zone, respectively.

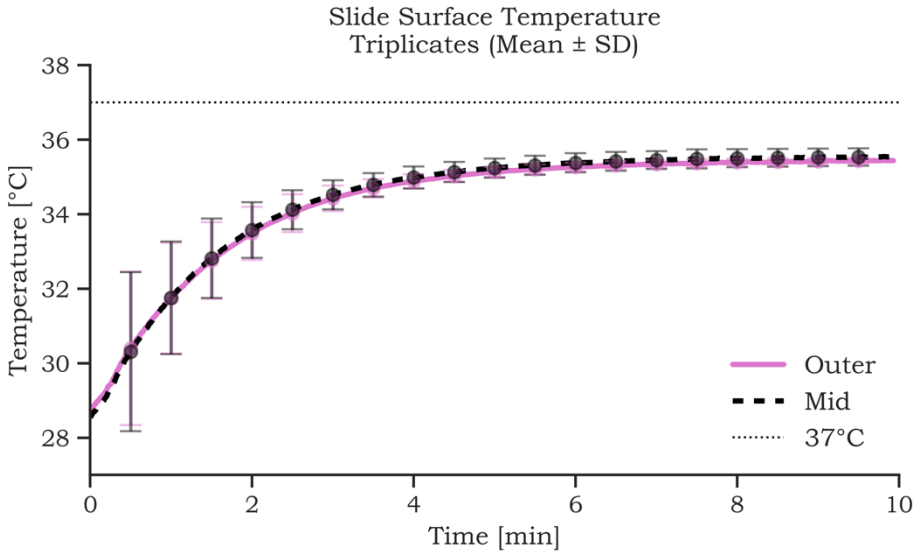

Figure 17: Temperature measurement at the middle and edge of sample area on the glass slide. The temperature at both positions seems identical. At the 10th minute, the measured T is 35.5 °C at the mid-zone and 35.4 °C at the middle zone. The mean temperature at every second and the SD error bars only every minute was plotted.

Figure 19 shows representatively chosen images taken within the mid-zone. The size, count and total covered area measurements are summarized in detail in Table 11.

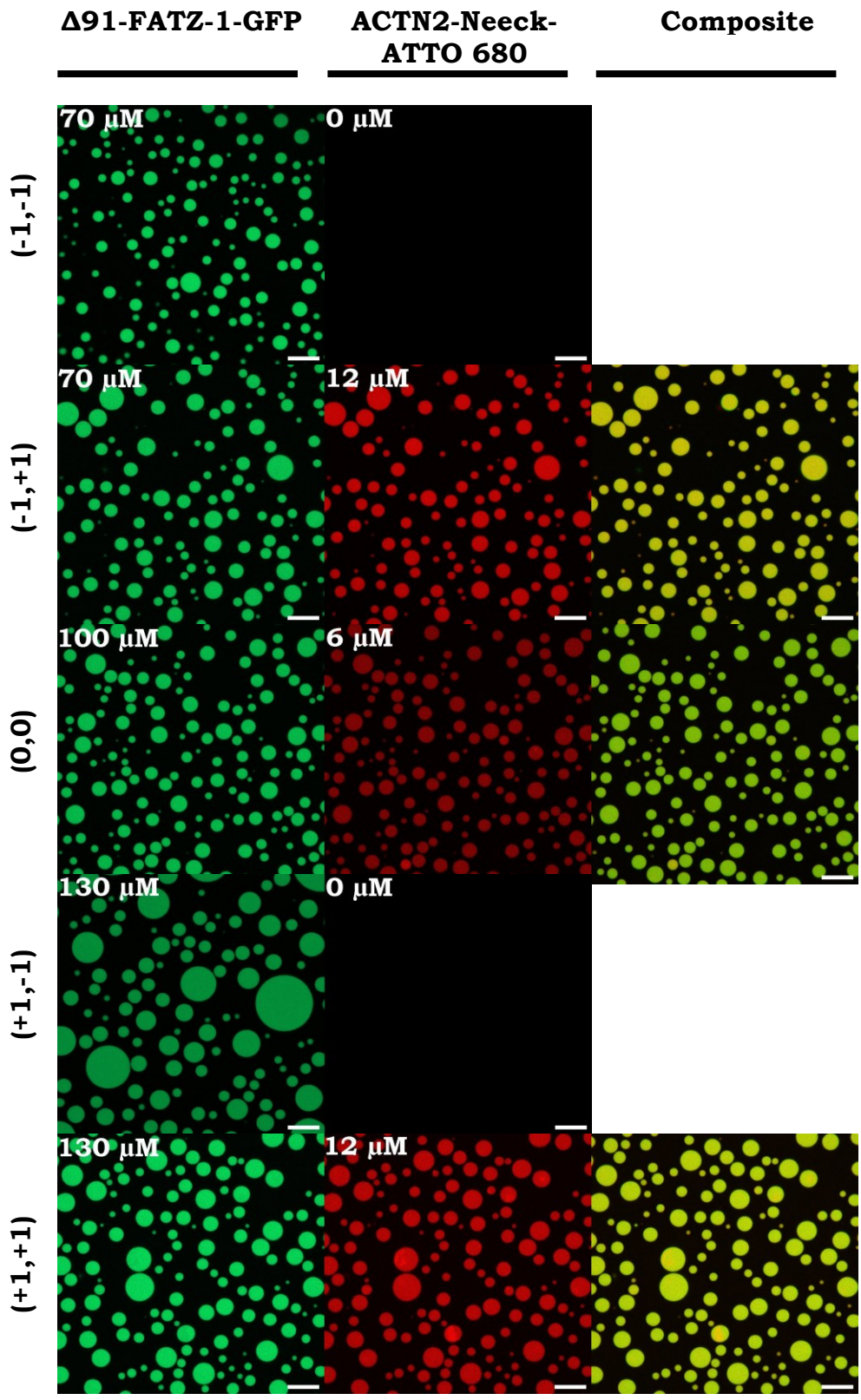

Figure 18: Confocal images of Δ91-FATZ-1-GFP with ACTN2-Neeck from mid-zone field-of-view. The images were chosen randomly. The experiment was repeated 3 times less than with the random field-of-view experiments. Images were taken at 10th minute at 37 °C. Image size: 84.53x84.53 µm. The scale bar is 10 µm. The brightness and intensity of images were untouched.

Table 11: Δ91-FATZ-1-GFP with α-actinin-2-Neeck-ATTO 680 droplet size, count and area covered measurements obtained from mid-zone imaging experiments. Non-integer numbers were rounded for count.

Coded Condition	**-1, -1**	**-1, +1**	**0, 0**	**+1, -1**	**+1, +1**
Δ91-FATZ-1-GFP [μM]	**70**	**70**	**100**	**130**	**130**
ACTN2-Neeck [μM]	**0**	**12**	**6**	**0**	**12**
N	9	9	12	9	9
Size [μM]					
Minimum	3.622	7.52	7.347	15.28	13.35
Median	7.568	10.46	9.128	21.06	16.19
Maximum	8.988	12.57	12.56	47.07	24.02
Mean	7.04	10.47	9.324	25.03	18.22
SD	1.993	1.862	1.643	11.48	4.593
Count					
Minimum	64	114	93	58	89
Median	86	122	126	86	105
Maximum	151	131	165	130	128
Mean	105	122	127	93	108
SD	36.12	6.042	16.85	23.3	14.42
Total Area Covered [%]					
Minimum	3.206	11.92	10.76	26.67	22.71
Median	12.18	21.07	16.79	29.39	31.07
Maximum	17.22	23.46	26.02	50.44	37.19
Mean	10.87	19.07	17.89	35.55	30
SD	5.251	4.39	4.78	10.18	5.47

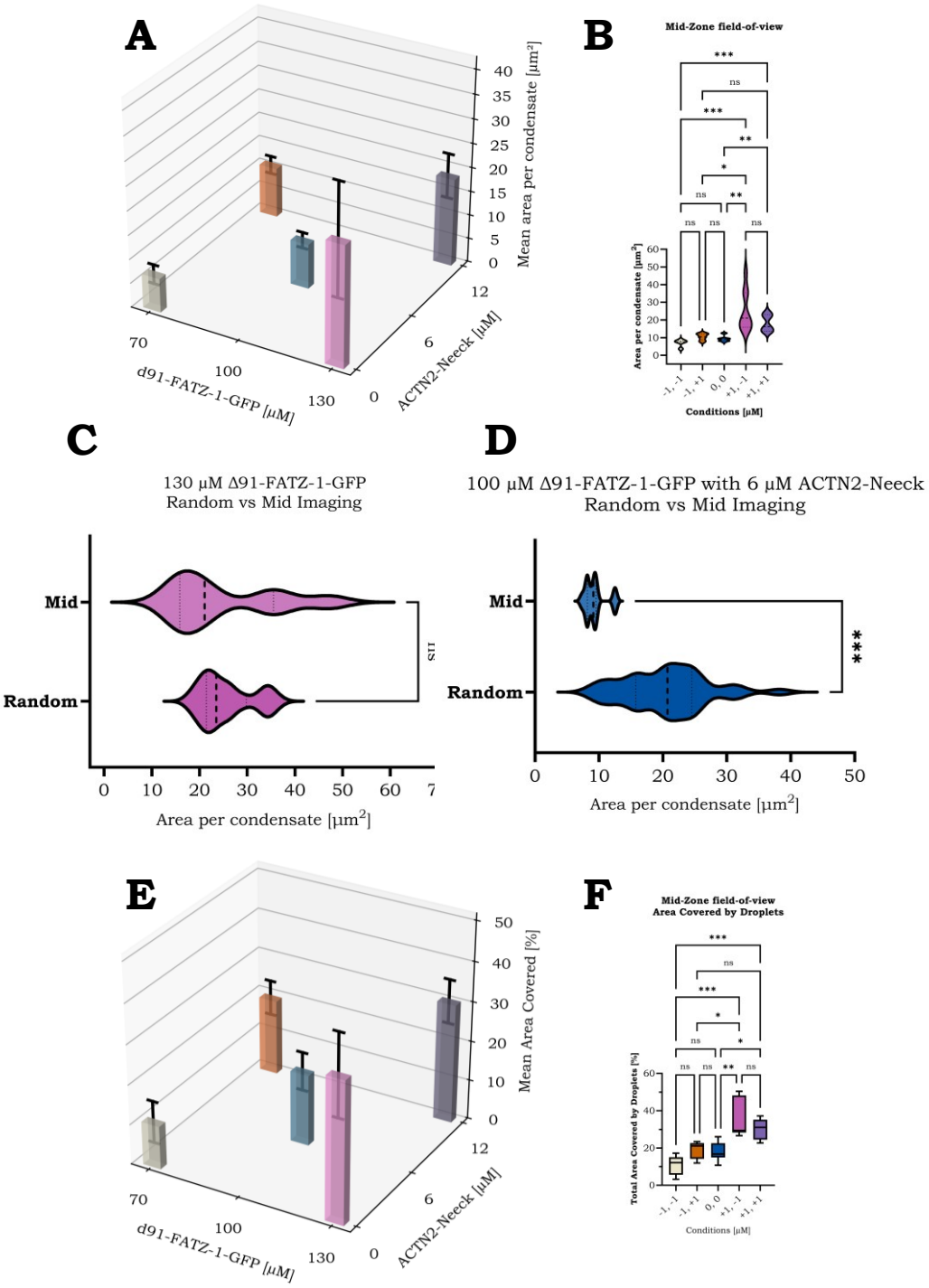

Figure 19: Droplet size and area covered measurements from mid-zone imaging experiment with Δ91-FATZ-1-GFP and ACTN2-Neeck. 20A-D: Overall, the spread of distribution is smaller than for random field-of-view images, except for 130 µM Δ91-FATZ-1-GFP. Statistically there were no difference in size between two sampling methods except for 100 µM Δ91-FATZ-1-GFP with 6 µM ACTN2-Neeck. 20E-D: Area covered by droplets. Sample size was 9 all conditions, and 12 for 100 µM Δ91-FATZ-1-GFP with 6 µM ACTN2-Neeck. Error bars represent SD. Coded factors for protein concentration conditions: X, Y = Δ91-FATZ-1-GFP, ACTN2-Neeck.

Figure 20 summarizes the droplet size and area covered measurements done in the mid-zone, together with representative pairwise comparisons with the random field-of-view experiments. The mid-zone droplet size distribution has overall a smaller spread than random field-of-view experiments, except for the 130 µM Δ91-FATZ-1-GFP. Only the 100 µM Δ91-FATZ-1-GFP with 6 µM α-actinin-2-Neeck has a statistically smaller droplet size than in the random field-of-view experiments. Without α-actinin-2-Neeck, the droplet size increases as the Δ91-FATZ-1-GFP concentration increases (conditions -1, -1 and +1, -1, Figure 20B). At constant Δ91-FATZ-1-GFP concentration, the droplet size does not significantly change upon increasing the α-actinin-2-Neeck concentration (between conditions -1, -1 and -1, +1 and conditions +1, -1 and +1, +1). At 12 µM α-actinin-2-Neeck, increasing the Δ91-FATZ-1-GFP concentration from 70 to 130 µM also does not change the droplet size. Similarly, at constant Δ91-FATZ-1-GFP concentration, the area covered by droplets also does not change upon increasing the α-actinin-2-Neeck concentration (Figure 20E-F). An increase in overall area is seen when the Δ91-FATZ-1-GFP is increased from 70 to 130 µM, at both α-actinin-2-Neeck concentrations.

4.3.3 Δ91-FATZ-1 condensates with increasing ZASP concentration

Figure 21 shows randomly chosen images of the Δ91-FATZ-1-GFP with ZASP-ATTO 565 experiment. In presence of ZASP, the shape of several droplets is occasionally asymmetrical and look like the droplet is asymmetrical and more ovoid (Figure 21 and Figure S7).

Table 12 summarizes the ZASP experiment measurements. Upon addition of 20 µM ZASP to 70 µM Δ91-FATZ-1-GFP, the average droplet size is reduced from 6.4 to 1.5 μm^2, corresponding to 4.3-fold change (Figure 22A). Also, the total area covered by droplets was reduced from 7.8 to 0.4%, almost a 20-fold reduction (Figure 22C). The count also decreased 4.5-fold (Figure 22E). At a higher Δ91-FATZ-1-GFP concentration, the effect is less drastic. At 130 µM of Δ91-FATZ-1-GFP, addition of 20 µM ZASP reduces the size 1.4-fold, total area covered by 1.4-fold while increasing the count by 1.1-fold. On the other hand, at constant high ZASP concentration of 20 µM, increasing the Δ91-FATZ-1-GFP from 70 to 130 µM increases the average droplet size 11.1-fold (significantly, Figure 22B), the count by 6.6-fold (not significant, Figure 22D) and the total droplet area by 75.5-fold (significantly, Figure 22E).

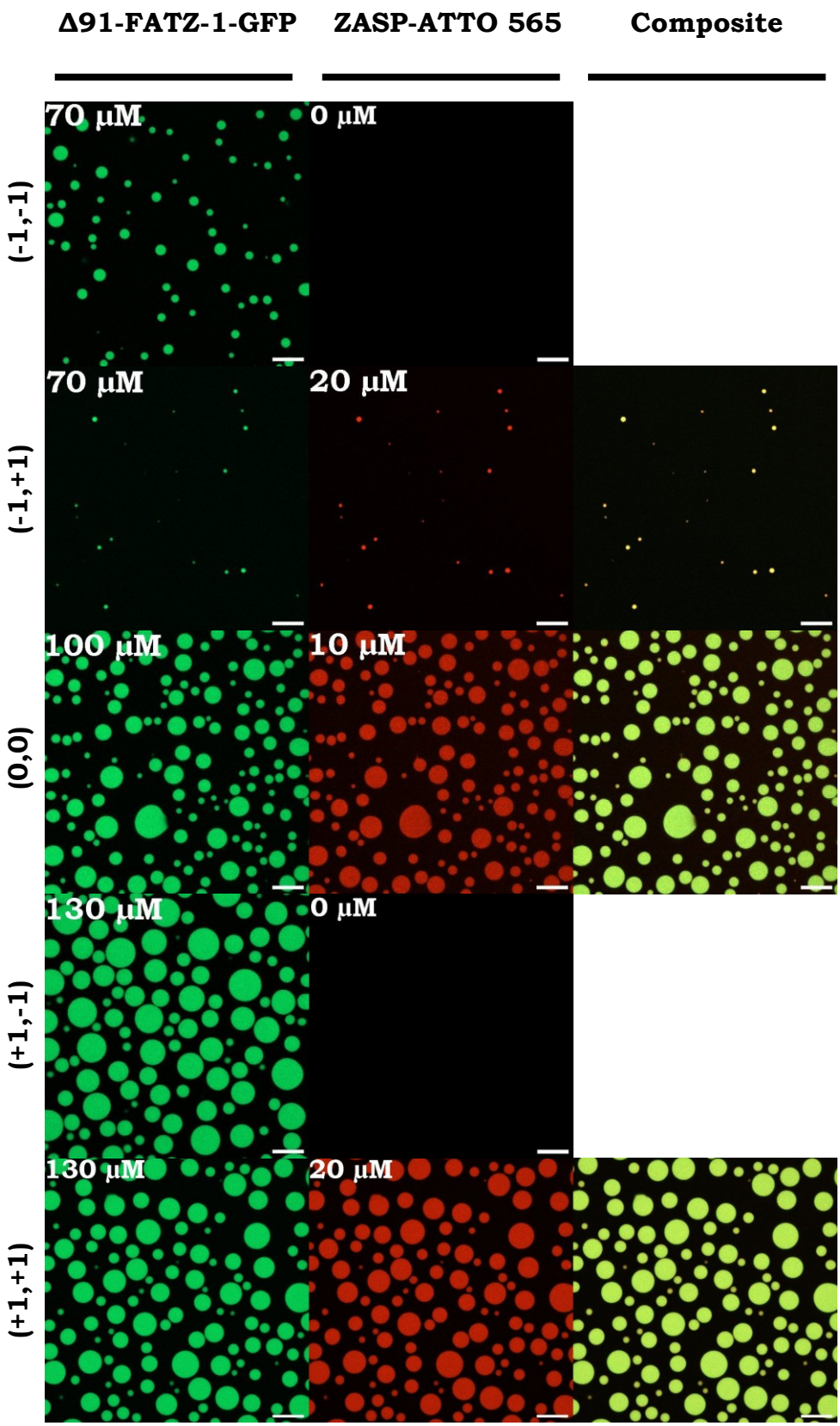

Figure 20: Confocal images of Δ91-FATZ-1 condensates with ZASP-ATTO 565. Occasionaly, droplets with a "blown" morphology were observed (indicated with an arrow). Images were taken after 10 min incubation at 37 °C. The images were chosen randomly. Image size: 84.53x84.53 μm. Scale bar is 10 μm.

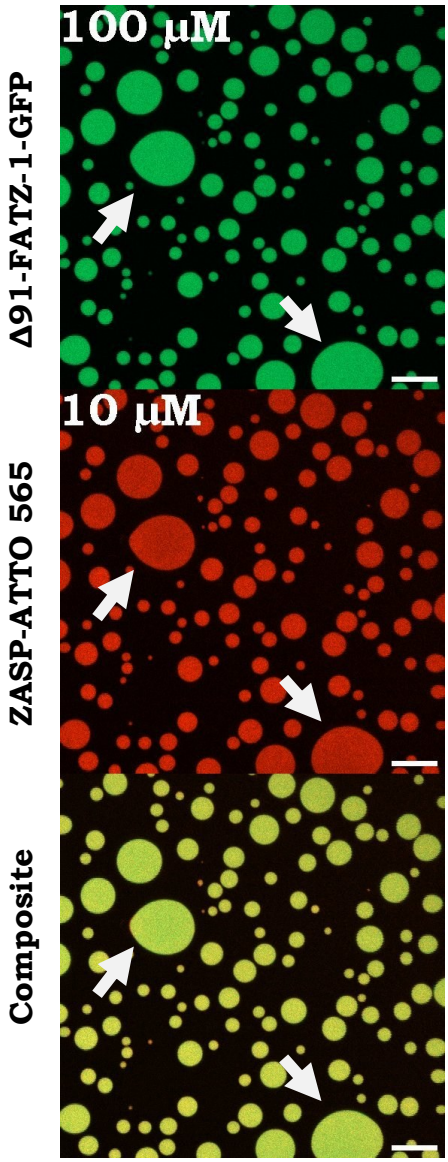

Figure 21: Δ91-FATZ-1-GFP droplet morphology occasionally deviates from a sphere in presence of ZASP (arrow). Images were taken after 10 min incubation at 37 °C. Image size: 84.53x84.53 µm. Scale bar is 10 µm.

Table 12: Δ91-FATZ-1-GFP with ZASP-ATTO 565 droplet size, count and area covered measurements. Non-integer numbers were rounded for count.

Coded Condition	**-1, -1**	**-1, +1**	**0, 0**	**+1, -1**	**+1, +1**
Δ91-FATZ-1-GFP [μM]	**70**	**70**	**100**	**130**	**130**
ZASP [μM]	**0**	**10**	**20**	**10**	**20**
N	9	6	12	6	3
Size [μM]					
Minimum	4.715	1.094	8.456	22.18	16.28
Median	5.937	1.549	12.05	23.95	16.91
Maximum	8.528	1.938	17.55	27.97	18.5
Mean	6.436	1.557	12.73	24.31	17.23
SD	1.148	0.3376	3.097	1.976	1.145
Count					
Minimum	46	10	107	95	109
Median	72	16	124	104	122
Maximum	128	29	136	113	124
Mean	81	18	122	104	118
SD	28.92	7.548	10.63	7.521	8.145
Total Area Covered [%]					
Minimum	3.761	0.199	16.06	35.89	30.54
Median	7.667	0.33	24.87	40.42	32.28
Maximum	13.82	0.784	37.05	43.91	33.48
Mean	7.821	0.425	25.73	40.06	32.1
SD	2.974	0.223	6.836	2.637	1.481

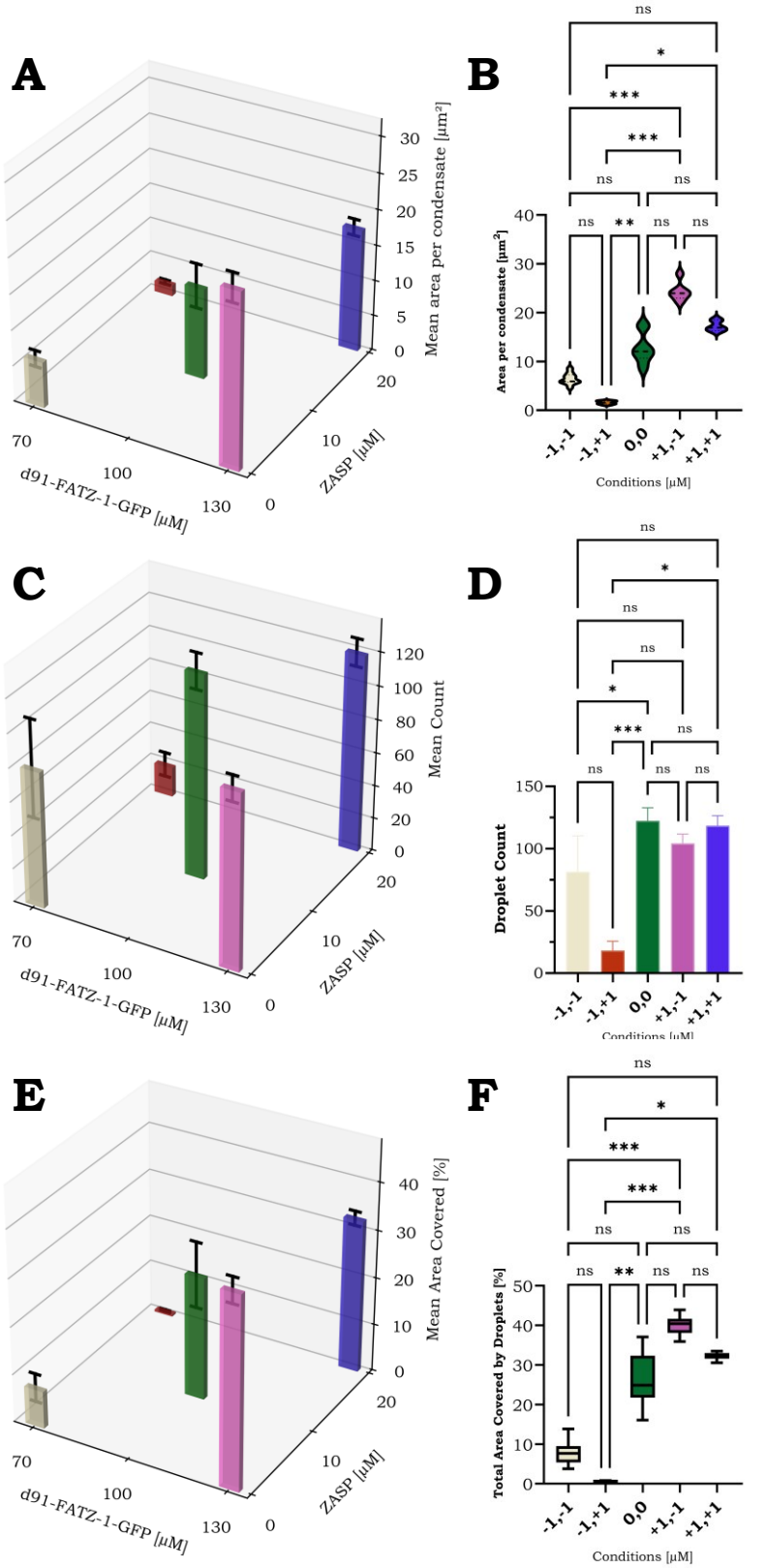

Figure 22: Phase diagrams and droplet measurement pairwise comparisions of Δ91-FATZ-1 with ZASP. Average droplet size is less than a micron and overall covered area is less than 1% for 70 uM Δ91-FATZ-1 with 20 uM ZASP. Error bars represent SD. Measurements were compared by ANOVA.

4.4 Turbidity of 70 µM Δ91-FATZ-1-GFP with increasing α-actinin-2-Neeck concentration

To test whether the hypothesis that α-actinin-2 reduces the turbidity and thus the LLPS of FATZ-1 holds true for different constructs, a turbidity assay with Δ91-FATZ-1-GFP (N-terminal His_6-tag) and α-actinin-2-Neeck (unlabeled and without His_6-tag) was done at concentrations similar as in the Sponga *et al.* (2021) study and the microscopy experiments (see Materials and Methods).

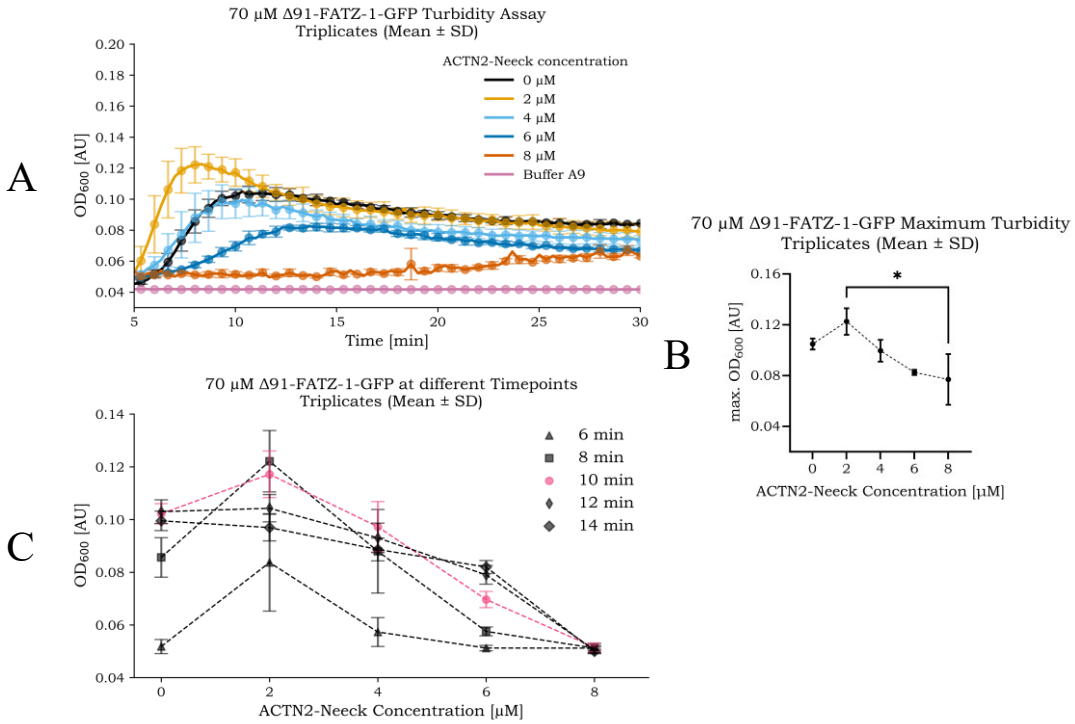

Figure 23: Turbidity assay with 70 µM Δ91-FATZ-1-GFP with increasing ACTN2-Neeck concentration. 23A: 2 µM Neeck (yellow) has the highest turbidity. As ACTN2-Neeck concentration is increased higher than 2 µM, the turbidity increases slower in comparision to lower c. 8 µM ACTN2-Neeck reaches maximum after 45th minute. Buffer (pink) is the negative LLPS control. SD bars were plotted every 40 sec. 23B: Maximum mean turbidity of each condition. 2 µM ACTN2-Neeck has the highest maximum turbidity. Statistically, only 2 µM turbidity max is higher than the 8 µM ACTN2-Neeck (ANOVA p* ≤ .033) . 23C: Mean turbidity measurements at different timepoints in function of ACTN2-Neeck. The 5th minute is the starting point where instrument is still stabilizing. At the 6th to 10th minutes, highest turbidity is observed at 2 µM ACTN2-Neeck with the strongest decay as ACTN2-Neeck concentration increases. At later timepoints, turbidity is overall lower and shows a linear downward tendency. After the 10th minute, turbidity with increasing ACTN2-Neeck concentration follows a linear downward trend.

Figure 23A depicts the turbidity measurements done with 70 μM Δ91-FATZ-1-GFP with increasing α-actinin-2-Neeck concentrations. All conditions follow an initially sigmoidal-like curve, typical for LLPS. As α-actinin-2-Neeck concentration is increased higher than 2 μM, the turbidity increases slower in comparison to lower concentrations. 8 μM α-actinin-2-Neeck curvature is visible in the full time-scale plot (Figure S8). There is no change in behavior after the 30th minute for the 0-6 μM turbidities. On the other hand, increase in 8 μM α-actinin-2-Neeck turbidity (orange) begins after the 20th minute, where lower concentration curves have already started to flatten. 2 μM α-actinin-2-Neeck condition (gold) has the highest turbidity maximum and reaches it earlier than the other concentrations (Table 11). 0 μM and 4 μM reach their maximum at the 10th minute, with a few seconds shift. 6 μM α-actinin-2-Neeck (dark blue) reaches its global maximum at the 13th minute, later than the lower α-actinin-2-Neeck concentrations. Moreover, the variance turbidity seems to decrease after the 10th minute and also as the Neeck concentration increases, except for 8 μM α-actinin-2-Neeck which exhibits SD spikes especially after the 30th minute. 2 μM Neeck curve exhibits overall the highest variance before the 10th minute as seen standard deviation (SD) error bars (gold).

Table 13: Turbidity maximum and timepoints with 70 μM Δ91-FATZ-1-GFP.

ACTN2-Neeck	**0 μM**	**2 μM**	**4 μM**	**6 μM**	**8 μM**
Max. Minutes	10	8	10	13	46
Max. OD_{600}	0.104	0.122	0.099	0.825	0.076

The maximum mean turbidity of 70 μM Δ91-FATZ-1-GFP with increasing α-actinin-2-Neeck concentration is plotted on Figure 23B. 2 μM α-actinin-2-Neeck has the highest turbidity. Also, the turbidity seems to show a downward trend as the α-actinin-2-Neeck concentration is increased. ANOVA results showed that there is significant difference between the turbidity maxima. However, the multiple comparisons test based on mean ranks detected a weak difference only between 2 μM and 8 μM α-actinin-2-Neeck turbidity maxima.
Figure 23C depicts the turbidity measurements of a certain α-actinin-2-Neeck concentration at a given timepoint, allowing to compare the trends in a time-dependent manner. Microscopy experiments were done at the 10th minute (pink). Based on statistical tests, while turbidity is significantly different between different α-actinin-2-Neeck concentrations, only turbidity of 2 μM α-actinin-2-Neeck is higher than turbidity of 8 μM α-actinin-2-Neeck at the 10th minute. Turbidity after the 10th minute shows a continuously downward trend as Neeck concentration increases, whereas no significant differences were detected.

5 Discussion

Multivalent Z-disc protein FATZ-1 forms biomolecular condensates *in vitro* and α-actinin-2 (ACTN2) and ZASP, two key players in context of myofibrillogenesis, colocalize to the FATZ-1 droplets. Despite the fact that their interactions are well described, the function of their specific interaction is still unclear (Sponga *et al.*, 2021; Von Nandelstadh *et al.*, 2009). It was previously also shown that increase in α-actinin-2 diminishes FATZ-1 droplet formation (Sponga *et al.,* 2021). These findings suggest that FATZ-1 might play a role in Z-body maturation into the Z-disc and α-actinin-2 and ZASP might regulate the condensates as myofibrillogenesis progresses. Moreover, biomolecular condensates function as subcellular organization and signaling tools to control local concentrations of cellular materials such as proteins and RNA especially during transient developmental stages (B. Wang *et al.*, 2021; Wu *et al.*, 2020). The propensity to phase separate and precisely the droplet size (linked to growth) has to be regulated in the cells for proper biological function in context of biomolecular condensate assemblies (Goehring & Hyman, 2012). Building on this foundation, this study aims to investigate how FATZ-1 condensates are influenced by α-actinin-2 and ZASP.

5.1 FATZ-1 concentration increases the droplet area

Under the confocal microscope, the FATZ-1 droplets are spherical and range from few to above 10 µm at these concentrations (Figure 14). Under the environmental conditions of this study (the 10th minute), 70 µM of FATZ-1 was assessed as the lower threshold where droplets were visible. Above 200 µM, FATZ-1 stock solutions begin to be more sensitive to temperature changes and tend to aggregate. Due to solubility issues and to a second limitation with the molar ratios of the other proteins of interest, a range between 70-130 µM was settled for FATZ-1. Further experiments showed that the droplet size increases in 2-fold range as the concentration increases from 70 to 130 µM (Figure 15, 19, 21). Yet, the actual cellular concentration of FATZ-1 in Z-body or Z-disc is still unknown, whereas the applied concentrations are probably way above physiologically relevant concentrations.

5.2 Effect of α-actinin-2 on FATZ-1 condensates – Microscopic characteristics

To investigate how the FATZ-1 condensates are influenced upon increasing the α-actinin-2 concentration, we used Δ91-FATZ-1-GFP and α-actinin-2-Neeck constructs. α-actinin-2-Neeck is a constantly open conformation

capable of binding actin even in absence of PIP and thus would resemble the active Z-body & Z-disc variant. It was previously shown that α-actinin-2 colocalizes to FATZ-1 droplets (Sponga *et al.*, 2021).

The here reported imaging experiment was designed based on DoE approach previously utilized in crystallography to minimize the amount of resources needed while being statistically relevant with the protein solubility and molar ratio limitations in mind. We worked under identical conditions for each experiment, including the laser power to avoid differentially heating the samples. However, a high variance in droplet distributions even within the same slide was observed, which was not reduced by increasing the replicate numbers. The possibility of an intrinsic uneven heat distribution on the slide surface was eliminated by measuring the temperature at different positions on the sample area with thermocouples, whereas the laser also heats the sample and might interfere with events such as droplet nucleation. Thus, to assess if imaging strategy influences droplet measurements, experiment was repeated in a smaller scale with sampling only the mid-zone. However, with both sampling methods, increasing the α-actinin-2-Neeck concentration from 0 to 12 µM at chosen FATZ-1 concentrations did not significantly change the droplet size, count or overall area covered by them (Figure 16, 17, 20). Increasing the α-actinin-2-Neeck concentration while keeping the concentration of Δ91-FATZ-1-GFP constant even increased the average droplet size and area covered by them slightly. On the other hand, all findings indicate that the droplet size increases about 2-fold upon increasing the Δ91-FATZ-1-GFP concentration, whether α-actinin-2 is there or not. Interestingly, Z-discs of α-actinin-2-Neeck transfected cells were eventually disrupted after widening, possibly due to uncontrolled and overly active integration of proteins into the Z-discs (Sponga *et al.*, 2021). Thus, it is also a possibility that the increased mobility of the α-actinin-2-Neeck construct might play an enhancing role in LLPS dynamics and interaction capacity of FATZ-1 and α-actinin-2.

5.3 Effect of α-actinin-2 on FATZ-1 condensates – Turbidity changes

Intriguingly, microscopy experiments do not agree with the previously done turbidity assays of FATZ-1 and α-actinin-2, where droplet formation was diminished by increasing α-actinin-2 concentration and formation was rescued by adding the LM2 peptide, which sequesters α-actinin-2 (Sponga *et al.* 2021). To understand this discrepancy, we conducted a new turbidity assay with 70 µM Δ91-FATZ-1-GFP and unlabeled α-actinin-2-Neeck in increasing concentration (0-2-4-6-8). Although a downward trend was observed above 2 µM α-actinin-2-Neeck, the change in turbidity was only

significant between 2 and 8 µM α-actinin-2-Neeck concentration and not to the same extent as reported in the Sponga *et al.* (2021) study (Figure 23B). In the time of writing this thesis, we know that different protein constructs and buffer conditions were used in the previous turbidity experiment. In this way, we clarified that a His_6-tag and the C-terminal GFP tag, previously thought as neglectable, effect LLPS behavior of the FATZ-1 condensates in presence of α-actinin-2-Neeck. Indeed, empirically, modifications on the same protein, such as mutations, affinity-tags and GFP-fusions may lead to different LLPS behavior than the wild-type protein, by modulating the secondary structure and solubility properties respectively (Conicella *et al.*, 2020; Sanulli & Narlikar, 2021; Uebel & Phillips, 2020). Moreover, post-translational modifications (PTMs) are potentially the major LLPS regulation mechanism in living cells, while *in vitro* proteins expressed in bacterial cells are PTM-less (Li *et al.*, 2022). This highlights the need to characterize and regard each construct of interest separately while aiming for the most physiological conditions to draw significant, real-life insights into the LLPS of proteins (?).

Interestingly, in all measurements before the 10th minute time point, addition of 2 µM α-actinin-2-Neeck to 70 µM Δ91-FATZ-1-GFP increased the turbidity, albeit not significantly (Figure 23C). However, this trend was now observed after the 10th minute, suggesting that different concentrations might have different behaviors and kinetics at different timepoints. Indeed, concentration series experiments showed, especially below the set minimal threshold of 70 µM, that droplet formation and dissolution might happen faster than for the higher concentrations (qualitative remark), adding further to the complexity and non-linearity in evaluation of results.

5.4 Effect of ZASP on FATZ-1 condensates

To investigate effect of ZASP on FATZ-1 condensates, a preliminary experiment was done with Δ91-FATZ-1-GFP and ZASP isoform 6. The latter construct is a rather soluble construct among other ZASP isoforms. It is clear from images and measurements that adding ZASP concentration decreases the droplet area at low FATZ-1 concentration, yet not in a statistically significant way (Figure 21, 22). Remarkably, increasing the Δ91-FATZ-1-GFP concentration in presence of a high ZASP concentration (20 µM) enhanced the increase in droplet size and area covered by one to two orders of magnitude, yet again not significantly (Table S3). Repeating this experiment with a bigger sample size and more replicates would allow to reduce the variance observed between samples and to draw more concrete conclusions about effect of ZASP on the FATZ-1 condensates. In the line of findings that the mildly hydrophilic dye ATTO 565 enhanced solubility of ZASP and allowed it to be concentrated up to 5-fold compared to the non-labeled protein, it is also possible that

fluorescent labeling might have effected properties of ZASP that influence FATZ-1 droplets. Thus, it would be advantageous to further study and characterize the constructs of interest as well as their conformational purity, as well as of each sample, before conducting imaging experiments. Mass photometry, dynamic light scattering, and SDS-PAGE based sedimentation experiments would be some examples to incorporate into this project.

Importantly, FATZ-1 droplets deviate from their spherical shape occasionally in presence of ZASP (Figure 21, S6). These droplets seem to be egg-shaped and asymmetrical, observed at each prepared sample. It is unclear what exactly might cause this. The droplet morphology adds another dimension to LLPS landscape of Z-disc proteins. Due to increased protein concentrations and interactions during gelation, more complex droplet morphologies such as multi-phased architectures may form especially when multiple multivalent components are present (Feric *et al.*, 2016). Arising droplet morphologies could be investigated with fluorescent imaging techniques like confocal microcopy and its less phototoxic modification spinning disc microcopy (Zhang *et al.*, 2023). The functional implications of such morphologies might lie in further fine-tuning of spatial and temporal organization of droplet components. (Feric *et al.*, 2016).

5.5 Conclusion and Outlook

The specific function of FATZ-1 interaction with key proteins in Z-disc maturation like α-actinin-2 and ZASP, is unclear. In the case that FATZ-1 phase-separates also in living cells, α-actinin-2 or ZASP might play a role in regulating the LLPS behavior of FATZ-1 during myofibrillogenesis. LLPS is a tool for cells to organize, concentrate and exchange material in sub-compartments and has been reported in many transient embryonic developmental stages like cell differentiation (Zhuge *et al.*, 2023). In this study, we utilized confocal microscopy experiments together with supporting turbidity assays to observe FATZ-1 condensates in presence of α-actinin-2 and ZASP. In microscopy experiments, LLPS was described by experimental outputs of droplet size, count, area. Changes in these upon increase of the second Z-disc protein concentration would suggest a potential regulation mechanism for the FATZ-1 LLPS, that might be a player during myofibrillogenesis. In the turbidity experiments, a decrease in turbidity upon increasing the α-actinin-2-Neeck concentration would suggest that α-actinin-2-Neeck has a diminishing effect on FATZ-1 droplets, an effect that would be expected to occur during transition from Z-bodies to Z-disc. Meanwhile, it is unknown if FATZ-1 phase separates in cells.

Microscopy and turbidity experiments are in agreement that α-actinin-2-Neeck does not influence FATZ-1 droplets in a statistically significant way at experimentally accessible concentrations in the scope of this study. Potentially, the variance and reproducibility of the microscopy and turbidity experiments could be improved by more replicates, yet this could also increase the hidden error if the setup is not perfectly "ideal", which is challenging to achieve as LLPS of proteins is still an enigmatic topic. Importantly, the α-actinin-2-Neeck concentrations used in microscopy experiments (0, 6 and 12 µM) were not in the same scale and resolution as the turbidity (0, 2, 4, 8 µM). While the DOE approached allowed us to test the "extremes" and explore boundaries, fine-tuned concentration series experiments with consistent and narrower concentration ranges and with identical constructs in parallel is required. However, it is safe to say that both microscopy and turbidity experiments are highly protein-demanding, considering the amount of replicates needed to reach a potential reproducibility.

Slightly differently to α-actinin-2-Neeck, increasing the ZASP concentration seems to reduce the droplet size and area when FATZ-1 concentration is low, yet again not in a significant way. Despite that, the droplet size is reduced to approximately a micron, 10-fold smaller than in the presence of high α-actinin-2-Neeck concentration. Also, the droplet size and area difference between 70 and 130 µM FATZ-1 is immense in presence of high ZASP concentration (Figure 22, Supplementary Table 3). These findings suggest that α-actinin-2-Neeck and ZASP influence FATZ-1 to an unknown but different extent, which is expected since ZASP is an intrinsically disordered protein with a similar size to FATZ-1 and α-actinin-2-Neeck is a bigger and structured dimer. Yet, it is intriguing to study different combinations and finer concentration windows of these Z-disc proteins as they are relevant for different developmental stages.

Importantly, the actual cellular concentration of FATZ-1 in the Z-body nor Z-disc is unknown. With current advances in proteomics, the average concentration of a protein in the cell can be calculated according to number of copies per cell and cell volume (Wiśniewski *et al.*, 2014). Our microscopy experiments required a minimum of 70 µM of FATZ-1. Also, how physiologically relevant the applied molar ratios of these proteins are, (namely to 70:60 µM and 130:12 M for FATZ-1:α-actinin-2 and 70:20 µM and 130:20 µM for FATZ-1:ZASP) is yet to be studied. It is possible that within the frame of this project, higher concentration ZASP-ATTO 565 can actually be applied. Finally, while the average width of a Z-disc is 0.13 µm, the droplets observed in this study exceed this by more than one order of magnitude (Squire *et al.*, 2005). ZASP at high concentrations actually resembled the common BC size in contrast to the bigger α-actinin-2-Neeck colocalized droplets.

According to the Sticker-Spacer Model, the droplet size distribution is dependent on the dynamics of the system (Ranganathan & Shakhnovich, 2020). The authors suggest that increased viscosity marked by a slowed-down droplet coalescence would shift the droplet size distribution to a smaller scale. In our results, only at low FATZ-1 and high ZASP concentration the reduction in droplet size was observed, albeit not significantly (Figure 21, Supplementary Table 3).

In conclusion, although other constructs may yield different results, this study demonstrated that FATZ-1 LLPS is not influenced significantly by increasing α-actinin-2 or ZASP concentration, regarded here as a potential regulation mechanism during myofibrillogenesis, specifically transition from the Z-body to mature Z-disc. Based on previous knowledge, an LLPS diminishing effect was expected upon increasing α-actinin-2 (Sponga *et al.*, 2021). However, based on our results, quite the opposite of a diminishing effect might be true, since a slight increase in droplet area at several concentration combinations were observed, also with ZASP especially at high FATZ-1 concentrations. This suggests that conducting the experiments at lower FATZ-1 concentrations might be more beneficial and circumvent the molar limitations on the proteins to observe significant effects.

While the experiments would possibly benefit from exploring more concentration ranges, protein combinations and more replicates, this interpretation is outlined here due to its simplicity and non-reliance on unverified assumptions, in accordance with the Occam's Razor principle. With our research, we addressed this gap in the knowledge how the FATZ-1 condensates are regulated by colocalizing Z-disc proteins *in vitro*. This is an exciting opportunity to re-shift the focus on dissecting the sequence of events during Z-body maturation into Z-disc. Meanwhile, immunofluorescence and further *in vitro* reconstruction experiments are ongoing in in our lab to pinpoint when and how FATZ-1 is involved in myofibrillogenesis and how α-actinin-2 and ZASP are related to LLPS in their own way. Our *in vitro* study revealed that while both α-actinin-2 and ZASP colocalize to the FATZ-1 condensates and ZASP causes a shift in droplet morphology, they influence droplet behavior differently to an unknown extent.

6 Supplementary Materials

Supplementary Figure 1: Schematics explaining Random field-of-view and Mid field-of-view imaging. During mid-zone imaging, the middle zone of the sample area marked with an X is imaged three times. During random imaging, any part of the sample area might be imaged, at random distances. The image was created using BioRender.

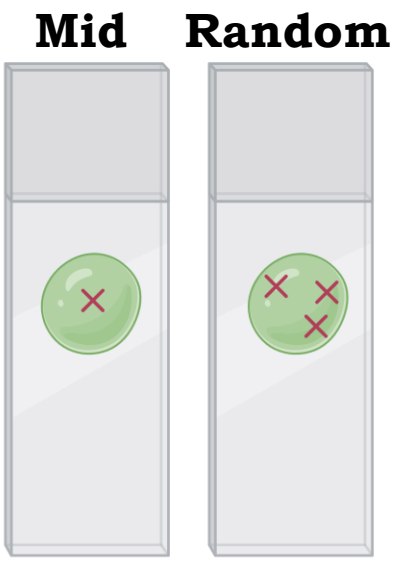

Supplementary Figure 2: 3D droplet count phase diagrams of Δ91-FATZ-1-GFP and ACTN2-Neeck-ATTO 680.

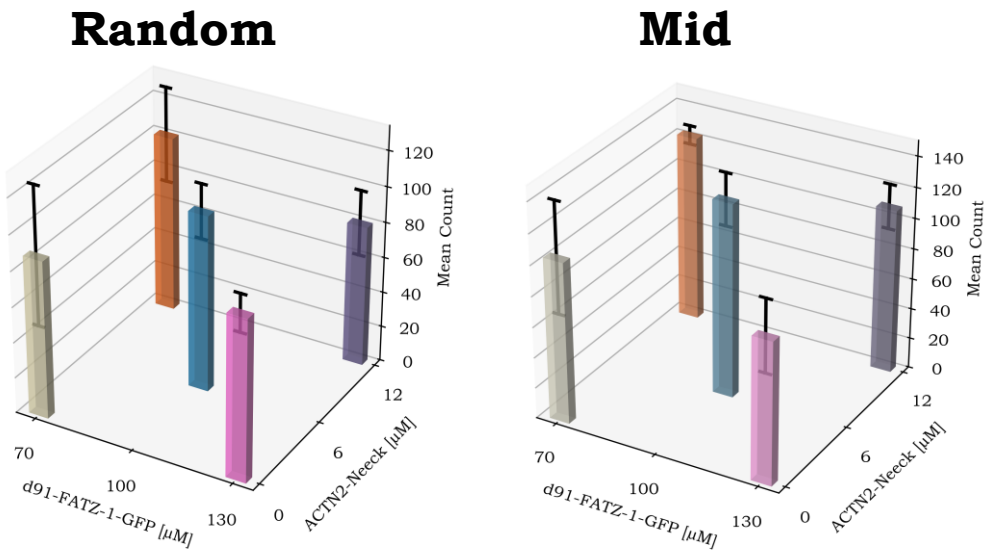

Supplementary Figure 3: Full pairwise comparisons of Δ91-FATZ-1-GFP with ACTN2-Neeck-ATTO 680 droplet size, count and area covered measurements. By non-parametric ANOVA. Significance is plotted in APA style. Ns stands for "not significant". A: Count, B: Droplet area per condensate, C: Area covered by droplets.

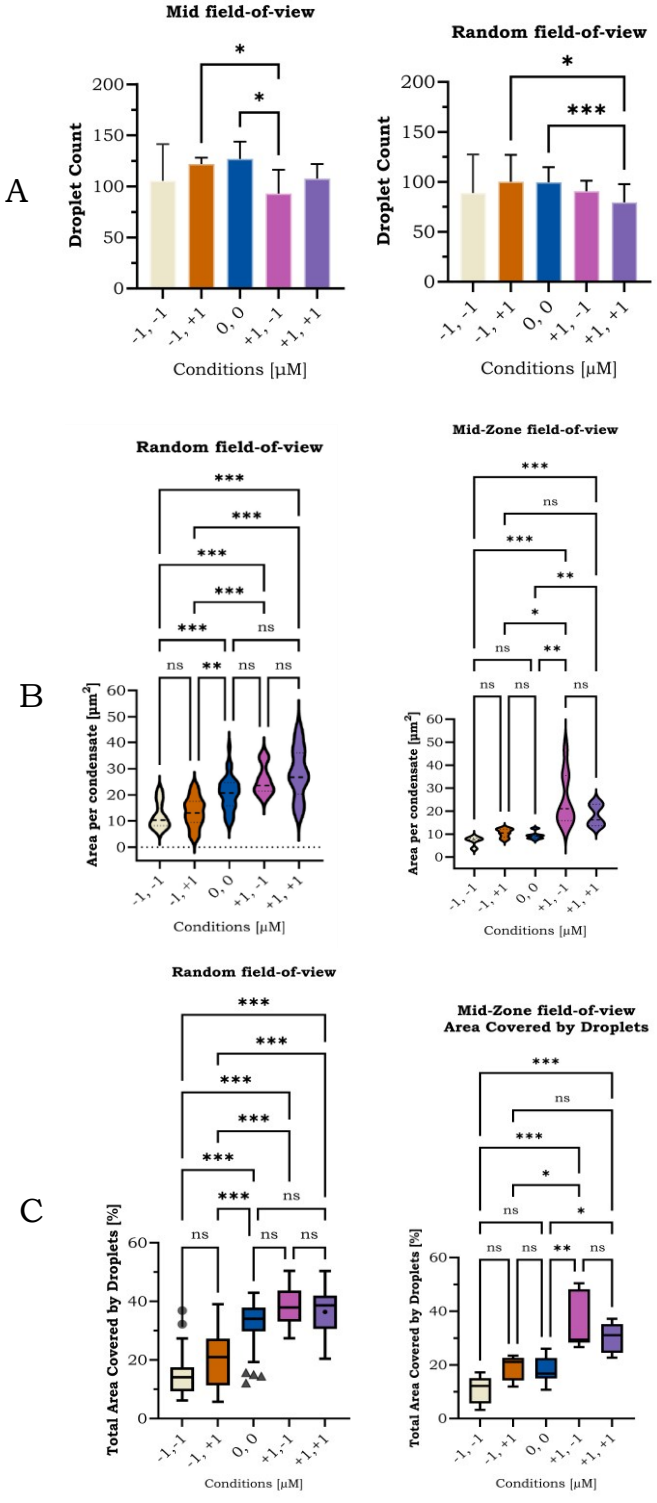

Supplementary Figure 1: Pairwise comparisons of Δ91-FATZ-1-GFP and ZASP with Δ91-FATZ-1-GFP and ACTN2-Neeck imaging experiments.

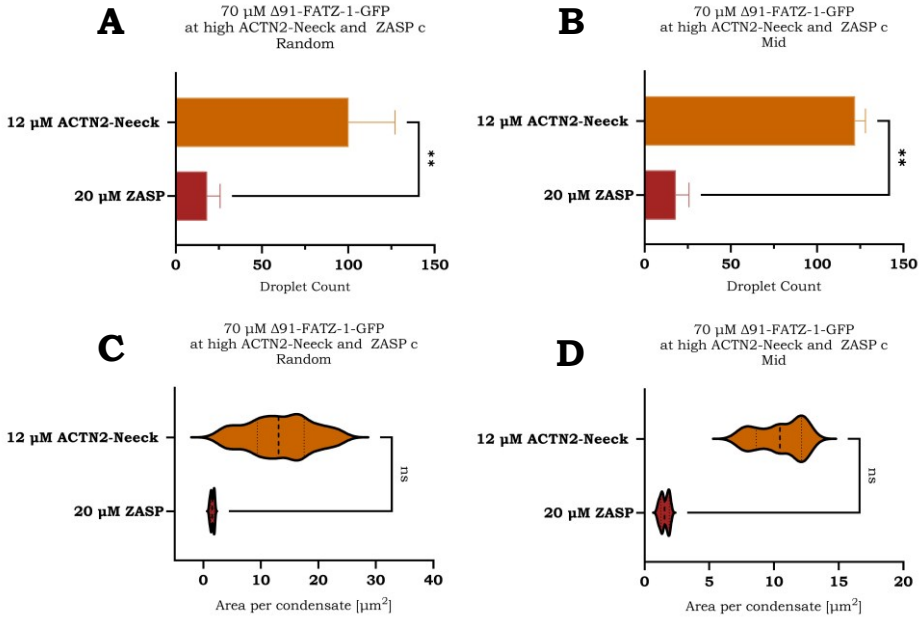

Supplementary Figure 2: Droplets are dynamic: fusion of droplets captured in real-time. Fusing droplets are indicated with an arrow. The ACTN2-Neeck channel was imaged before Δ91-FATZ-1-GFP channel. To avoid confusion, measurements were done only on Δ91-FATZ-1-GFP images. Image size: 84.53x84.53 µm. Scale bar: 10 µm.

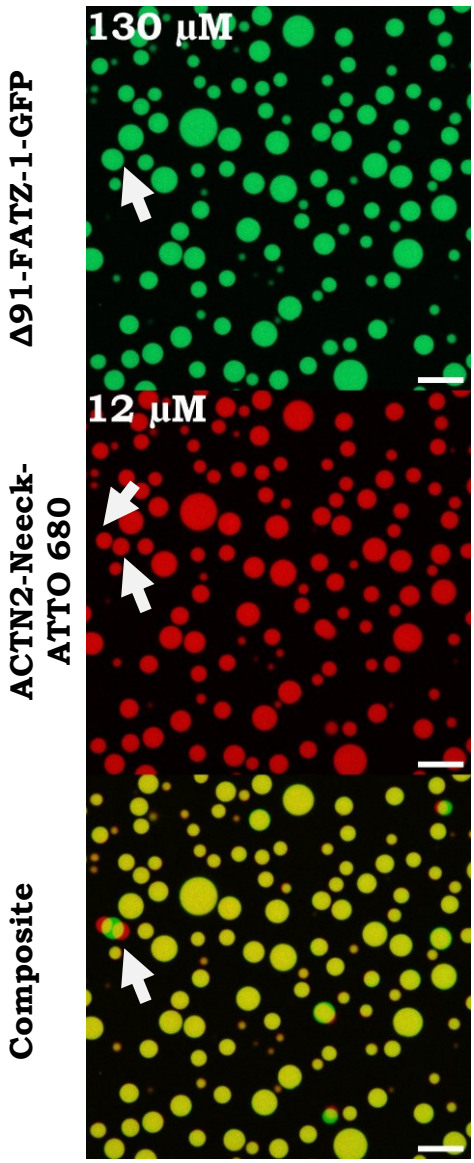

Supplementary Figure 4: Droplet size leverage analysis of Δ91-FATZ-1-GFP with ACTN2-Neeck-ATTO 680 random field-of-view experiments. These screenshot results belong to JMP software. The effect of each factor is given in the effect summary.

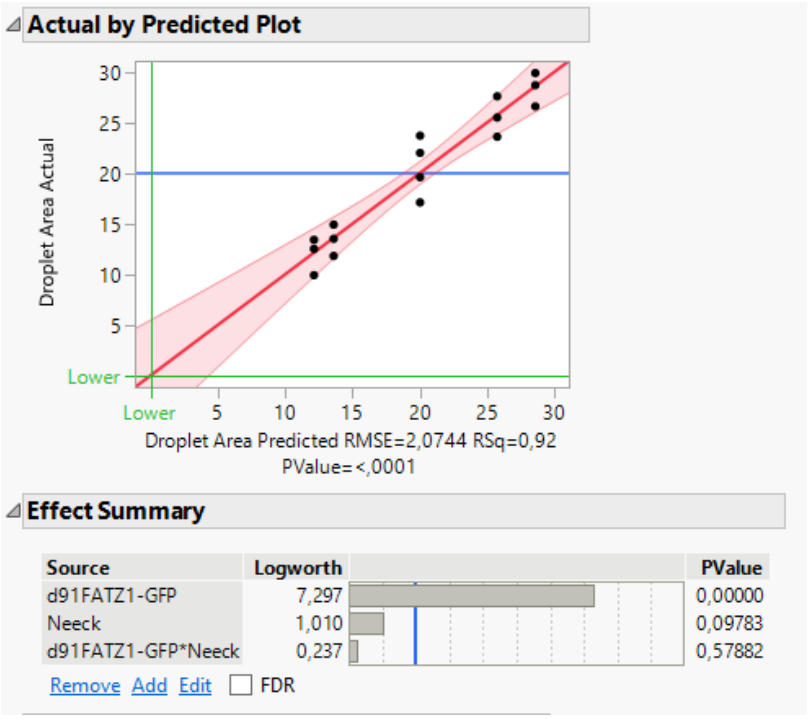

Supplementary Figure 4: The full time-scale plot of Δ91-FATZ-1-GFP turbidity assay. Error bars were plotted every 2 minutes.

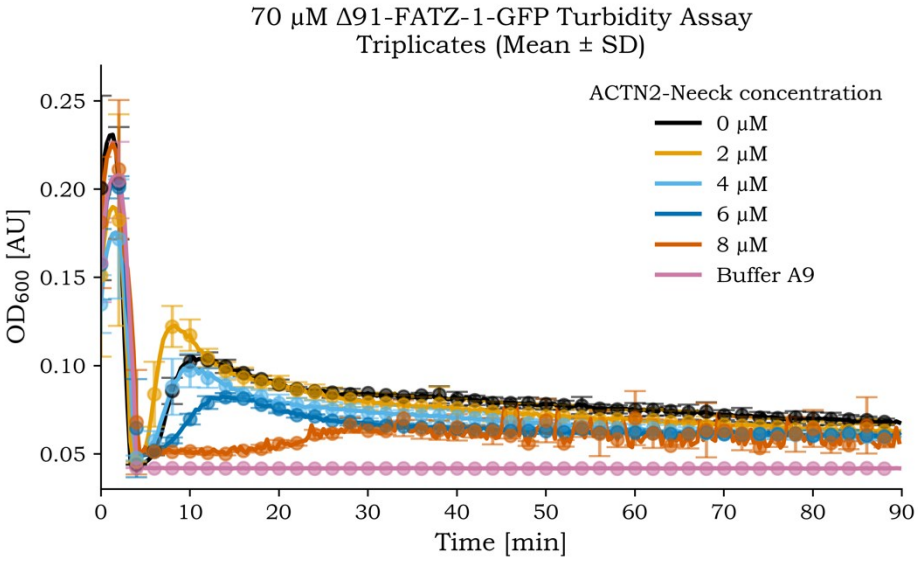

>delta91-FATZ-1-GFP_3C_NtHis6
MAHHHHHHSAG**LEVLFQ**GPTVGGQLGTAGQGFSYSKSNGRGGSQAGGSGSAGQYGSDQQHHL
GSGSGAGGTGGPAGQAGRGGAAGTAGVGETGSGDQAGGEGKHITVFKTYISPWERAMGVDPQ
QKMELGIDLLAYGAKAELPKYKSFNRTAMPYGGYEKASKRMTFQMPKFDLGPLLSEPLVLYN
QNLSNRPSFNRTPIPWLSSGEPVDYNVDIGIPLDGETEELGSGSGMSKGEELFTGVVPILVE
LDGDVNGHKFSVRGEGEGDATNGKLTLKFICTTGKLPVPWPTLVTTLTYGVQCFSRYPDHMK
RHDFFKSAMPEGYVQERTISFKDDGTYKTRAEVKFEGDTLVNRIELKGIDFKEDGNILGHKL
EYNFNSHNVYITADKQKNGIKANFKIRHNVEDGSVQLADHYQQNTPIGDGPVLLPDNHYLST
QSVLSKDPNEKRDHMVLLEFVTAAGITHGMDELYK

>ACTN2_Neeck_TEV_NtHis6
MHHHHHHGSST**ENLYFQ**GSSNQIEPGVQYNYVYDEDEYMIQEEEWDRDLLLDPAWEKQQRKT
FTAWCNSHLRKAGTQIENIEEDFRNGLKLMLLLEVISGERLPKPDRGKMRFHKIANVNKALD
YIASKGVKLVSIGAEEIVDGNVKMTLGMIWTIILRFAIQDISVEETSAKEGLLLWCQRKTAP
YRNVNIQNFHTSWKDGLGLCALIHRHRPDLIDYSKLNKDDPIGNINLAMEIAEKHLDIPKML
DAEDIVNTPKPDERAIMTYVSCFYHAFAGAEQAETAANEECKVEAVNQENERLMEEYERLAS
ELLEWIRRTIPWLENRTPEKTMQAMQKKLEDFRDYRRKHKPPKVQEKCQLEINFNTLQTKLR
ISNRPAFMPSEGKMVSDIAGAWQRLEQAEKGYEEWLLNEIRRLERLEHLAEKFRQKASTHET
WAYGKEQILLQKDYESASLTEVRALLRKHEAFESDLAAHQDRVEQIAAIAQELNELDYHDAV
NVNDRCQKICDQWDRLGTLTQKRREALERMEKLLETIDQLHLEFAKRAAPFNNWMEGAMEDL
QDMFIVHSIEEIQSLITAHEQFKATLPEADGERQSIMAIQNEVEKVIQSYNIRISSSNPYST
VTMDELRTKWDKVKQLVPIRDQSLQEELARQHANERLRRQFAAQANAIGPWIQNKMEEIARS
SIQITGALEDQMNQLKQYEHNIINYKNNIDKLEGDHQLIQEALVFDNKHTNYTMEHIRVGWE
LLLTTIARTINEVETQILTRDAKGITQEQMNEFRASFNHFDRRKNGLMDHEDFRACLISMGY
DLGEAEFARIMTLVDPNGQGTVTFQSFIDFMTRETADTDTAEQVIASFRILASDKPYILAEE
LRRELPPDQAQYCIKRMPAYSGPGSVPGALDYAAFSSALYGESDL

> ZASP_i6_3C_NtHis6
MKHHHHHHSAG**LEVLFQ**GPAMSYSVTLTGPGPWGFRLQGGKDFNMPLTISRITPGSKAAQSQ
LSQGDLVVAIDGVNTDTMTHLEAQNKIKSASYNLSLTLQKSKRPIPISTTAPPVQTPLPVIP
HQKVVVNSPANADYQERFNPSALKDSALSTHKPIEVKGLGGKATIIHAQYNTPISMYSQDAI
MDAIAGQAQAQGSDFSGSLPIKDLAVDSASPVYQAVIKSQNKPEDEADEWARRSSNLQSRSF
RILAQMTGTEFMQDPDEEALRRSRERFETERNSPRFAKLRNWHHGLSAQILNVKS

Protein Sequence Legend:

Pre3C Protease cleavage site (bold letters underlined with double line)

TEV cleavage site (bold letters underlined with a wavy line)

suGFP sequence (letters underlined with a dotted line)

His_6-tag (letters underlined with a single line)

7 References

Alberti, S., Gladfelter, A., & Mittag, T. (2019). Considerations and Challenges in Studying Liquid-Liquid Phase Separation and Biomolecular Condensates. *Cell*, *176*(3), 419–434. https://doi.org/10.1016/j.cell.2018.12.035

Arter, W. E., Qi, R., Erkamp, N. A., Krainer, G., Didi, K., Welsh, T. J., Acker, J., Nixon-Abell, J., Qamar, S., Guillén-Boixet, J., Franzmann, T. M., Kuster, D., Hyman, A. A., Borodavka, A., George-Hyslop, P. S., Alberti, S., & Knowles, T. P. J. (2022). Biomolecular condensate phase diagrams with a combinatorial microdroplet platform. *Nature Communications*, *13*(1), 7845. https://doi.org/10.1038/s41467-022-35265-7

ATTO-TEC. (2023, 2024). *Fluorescent Labels and Dyes catalogue 2023/2024*. ATTO-TEC. https://www.atto-tec.com/images/ATTO/Katalog_Preisliste/Katalog_2023_2024.pdf

Banani, S. F., Lee, H. O., Hyman, A. A., & Rosen, M. K. (2017). Biomolecular condensates: Organizers of cellular biochemistry. *Nature Reviews Molecular Cell Biology*, *18*(5), 285–298. https://doi.org/10.1038/nrm.2017.7

Boeynaems, S., Alberti, S., Fawzi, N. L., Mittag, T., Polymenidou, M., Rousseau, F., Schymkowitz, J., Shorter, J., Wolozin, B., Van Den Bosch, L., Tompa, P., & Fuxreiter, M. (2018). Protein Phase Separation: A New Phase in Cell Biology. *Trends in Cell Biology*, *28*(6), 420–435. https://doi.org/10.1016/j.tcb.2018.02.004

Brangwynne, C. P. (2013). Phase transitions and size scaling of membrane-less organelles. *Journal of Cell Biology*, *203*(6), 875–881. https://doi.org/10.1083/jcb.201308087

Bressloff, P. C. (2020). Active suppression of Ostwald ripening: Beyond mean-field theory. *Physical Review E*, *101*(4), 042804. https://doi.org/10.1103/PhysRevE.101.042804

Cinar, H., & Winter, R. (2020). The effects of cosolutes and crowding on the kinetics of protein condensate formation based on liquid–liquid phase separation: A pressure-jump relaxation study. *Scientific Reports*, *10*(1), 17245. https://doi.org/10.1038/s41598-020-74271-x

Conicella, A. E., Dignon, G. L., Zerze, G. H., Schmidt, H. B., D'Ordine, A. M., Kim, Y. C., Rohatgi, R., Ayala, Y. M., Mittal, J., & Fawzi, N. L. (2020). TDP-43 α-helical structure tunes liquid–liquid phase separation and function. *Proceedings of the National Academy of Sciences*, *117*(11), 5883–5894. https://doi.org/10.1073/pnas.1912055117

Decker, M., Jaensch, S., Pozniakovsky, A., Zinke, A., O'Connell, K. F., Zachariae, W., Myers, E., & Hyman, A. A. (2011). Limiting Amounts of Centrosome Material Set Centrosome Size in C. elegans Embryos. *Current Biology*, *21*(15), 1259–1267. https://doi.org/10.1016/j.cub.2011.06.002

Deutsch, E. W., Sun, Z., Campbell, D., Kusebauch, U., Chu, C. S., Mendoza, L., Shteynberg, D., Omenn, G. S., & Moritz, R. L. (2015). State of the Human Proteome in 2014/2015 As Viewed through PeptideAtlas: Enhancing Accuracy and Coverage through the AtlasProphet. *Journal of Proteome Research*, *14*(9), 3461–3473. https://doi.org/10.1021/acs.jproteome.5b00500

Dlugosz, A. A., Antin, P. B., Nachmias, V. T., & Holtzer, H. (1984). The relationship between stress fiber-like structures and nascent myofibrils in cultured cardiac myocytes. *The Journal of Cell Biology*, *99*(6), 2268–2278. https://doi.org/10.1083/jcb.99.6.2268

Du, A., Sanger, J. M., Linask, K. K., & Sanger, J. W. (2003). Myofibrillogenesis in the first cardiomyocytes formed from isolated quail precardiac mesoderm. *Developmental Biology*, *257*(2), 382–394. https://doi.org/10.1016/S0012-1606(03)00104-0

Elliott, A. D. (2020). Confocal Microscopy: Principles and Modern Practices. *Current Protocols in Cytometry*, *92*(1), e68. https://doi.org/10.1002/cpcy.68

Faulkner, G., Pallavicini, A., Comelli, A., Salamon, M., Bortoletto, G., Ievolella, C., Trevisan, S., Kojić, S., Dalla Vecchia, F., Laveder, P., Valle, G., & Lanfranchi, G. (2000). FATZ, a Filamin-, Actinin-, and Telethonin-binding Protein of the Z-disc of Skeletal Muscle. *Journal of Biological Chemistry*, *275*(52), 41234–41242. https://doi.org/10.1074/jbc.M007493200

Feric, M., Vaidya, N., Harmon, T. S., Mitrea, D. M., Zhu, L., Richardson, T. M., Kriwacki, R. W., Pappu, R. V., & Brangwynne, C. P. (2016). Coexisting Liquid Phases Underlie Nucleolar Subcompartments. *Cell*, *165*(7), 1686–1697. https://doi.org/10.1016/j.cell.2016.04.047

Frank, D., Kuhn, C., Katus, H. A., & Frey, N. (2006). The sarcomeric Z-disc: A nodal point in signalling and disease. *Journal of Molecular Medicine*, *84*(6), 446–468. https://doi.org/10.1007/s00109-005-0033-1

Frey, N., Barrientos, T., Shelton, J. M., Frank, D., Rütten, H., Gehring, D., Kuhn, C., Lutz, M., Rothermel, B., Bassel-Duby, R., Richardson, J. A., Katus, H. A., Hill, J. A., & Olson, E. N. (2004). Mice lacking calsarcin-1 are sensitized to calcineurin signaling and show accelerated cardiomyopathy in response to pathological biomechanical stress. *Nature Medicine*, *10*(12), 1336–1343. https://doi.org/10.1038/nm1132

Gasteiger, E., Hoogland, C., Gattiker, A., Duvaud, S., Wilkins, M. R., Appel, R. D., & Bairoch, A. (2005). Protein Identification and Analysis Tools on the ExPASy Server. In J. M. Walker (Ed.), *The Proteomics Protocols Handbook* (pp. 571–607). Humana Press. https://doi.org/10.1385/1-59259-890-0:571

Gautel, M., & Djinović-Carugo, K. (2016). The sarcomeric cytoskeleton: From molecules to motion. *Journal of Experimental Biology*, *219*(2), 135–145. https://doi.org/10.1242/jeb.124941

Gautel, M., Goulding, D., Bullard, B., Weber, K., & Fürst, D. O. (1996). The central Z-disk region of titin is assembled from a novel repeat in variable copy numbers. *Journal of Cell Science*, *109*(11), 2747–2754. https://doi.org/10.1242/jcs.109.11.2747

Goehring, N. W., & Hyman, A. A. (2012). Organelle Growth Control through Limiting Pools of Cytoplasmic Components. *Current Biology*, *22*(9), R330–R339. https://doi.org/10.1016/j.cub.2012.03.046

Goldstein, M. A., Michael, L. H., Schroeter, J. P., & Sass, R. L. (1988). Structural states in the Z band of skeletal muscle correlate with states of active and passive tension. *The Journal of General Physiology*, *92*(1), 113–119. https://doi.org/10.1085/jgp.92.1.113

Henderson, C. A., Gomez, C. G., Novak, S. M., Mi-Mi, L., & Gregorio, C. C. (2017). Overview of the Muscle Cytoskeleton. In R. Terjung (Ed.), *Comprehensive Physiology* (1st ed., pp. 891–944). Wiley. https://doi.org/10.1002/cphy.c160033

Hess, G. T., Cragnolini, J. J., Popp, M. W., Allen, M. A., Dougan, S. K., Spooner, E., Ploegh, H. L., Belcher, A. M., & Guimaraes, C. P. (2012). M13 Bacteriophage Display Framework That Allows Sortase-Mediated Modification of Surface-Accessible Phage Proteins. *Bioconjugate Chemistry*, *23*(7), 1478–1487. https://doi.org/10.1021/bc300130z

Hirose, T., Ninomiya, K., Nakagawa, S., & Yamazaki, T. (2023). A guide to membraneless organelles and their various roles in gene regulation. *Nature Reviews Molecular Cell Biology*, *24*(4), 288–304. https://doi.org/10.1038/s41580-022-00558-8

Huang, Q., Szklarczyk, D., Wang, M., Simonovic, M., & Von Mering, C. (2023). PaxDb 5.0: Curated Protein Quantification Data Suggests Adaptive Proteome Changes in Yeasts. *Molecular & Cellular Proteomics*, *22*(10), 100640. https://doi.org/10.1016/j.mcpro.2023.100640

Huxley, A. F., & Niedergerke, D. R. (1954). *Interference Microscopy of Living Muscle Fibres*. https://doi.org/10.1038/173971a0

Kanaan, N. M., Hamel, C., Grabinski, T., & Combs, B. (2020). Liquid-liquid phase separation induces pathogenic tau conformations in vitro. *Nature Communications*, *11*(1), 2809. https://doi.org/10.1038/s41467-020-16580-3

Kato, M., Han, T. W., Xie, S., Shi, K., Du, X., Wu, L. C., Mirzaei, H., Goldsmith, E. J., Longgood, J., Pei, J., Grishin, N. V., Frantz, D. E., Schneider, J. W., Chen, S., Li, L., Sawaya, M. R., Eisenberg, D., Tycko, R., & McKnight, S. L. (2012). Cell-free Formation of RNA Granules: Low Complexity Sequence Domains Form Dynamic Fibers within Hydrogels. *Cell*, *149*(4), 753–767. https://doi.org/10.1016/j.cell.2012.04.017

Katzemich, A., Liao, K. A., Czerniecki, S., & Schöck, F. (2013). Alp/Enigma Family Proteins Cooperate in Z-Disc Formation and Myofibril Assembly. *PLoS Genetics*, *9*(3), e1003342. https://doi.org/10.1371/journal.pgen.1003342

Kaya-Çopur, A., Marchiano, F., Hein, M. Y., Alpern, D., Russeil, J., Luis, N. M., Mann, M., Deplancke, B., Habermann, B. H., & Schnorrer, F. (2021). The Hippo pathway controls myofibril assembly and muscle fiber growth by regulating sarcomeric gene expression. *eLife*, *10*, e63726. https://doi.org/10.7554/eLife.63726

Kontrogianni-Konstantopoulos, A., Ackermann, M. A., Bowman, A. L., Yap, S. V., & Bloch, R. J. (2009). Muscle Giants: Molecular Scaffolds in Sarcomerogenesis. *Physiological Reviews*, *89*(4), 1217–1267. https://doi.org/10.1152/physrev.00017.2009

Kopanic, J. L., Al-Mugotir, M., Zach, S., Das, S., Grosely, R., & Sorgen, P. L. (2013). An Escherichia coli strain for expression of the connexin45 carboxyl terminus attached to the 4th transmembrane domain. *Frontiers in Pharmacology*, *4*. https://doi.org/10.3389/fphar.2013.00106

Lee, D. S. W., Choi, C.-H., Sanders, D. W., Beckers, L., Riback, J. A., Brangwynne, C. P., & Wingreen, N. S. (2023). Size distributions of intracellular condensates reflect competition between coalescence and nucleation. *Nature Physics*, *19*(4), 586–596. https://doi.org/10.1038/s41567-022-01917-0

Li, J., Zhang, M., Ma, W., Yang, B., Lu, H., Zhou, F., & Zhang, L. (2022). Post-translational modifications in liquid-liquid phase separation: A comprehensive review. *Molecular Biomedicine*, *3*(1), 13. https://doi.org/10.1186/s43556-022-00075-2

Luther, P. K. (2009). The vertebrate muscle Z-disc: Sarcomere anchor for structure and signalling. *Journal of Muscle Research and Cell Motility*, *30*(5–6), 171–185. https://doi.org/10.1007/s10974-009-9189-6

Luther, P. K., Barry, J. S., & Squire, J. M. (2002). The three-dimensional structure of a vertebrate wide (slow muscle) Z-band: Lessons on Z-band assembly11Edited by J. Karn. *Journal of Molecular Biology*, *315*(1), 9–20. https://doi.org/10.1006/jmbi.2001.5217

Mills, M. A., Yang, N., Weinberger, R. P., Woude, D. L. V., Beggs, A. H., Easteal, S., & North, K. N. (2001). Differential expression of the actin-binding proteins, α-actinin-2 and -3, in different species: Implications for the evolution of functional redundancy. *Human Molecular Genetics*, *10*(123), 1335–1346. https://doi.org/10.1093/hmg/10.13.1335

Nakatsuji, N. (2013). Mesoscopic science, where materials become life and life inspires materials. A great opportunity to push back the frontiers of life, materials, and biomaterials sciences. *Biomater. Sci.*, *1*(1), 9–10. https://doi.org/10.1039/C2BM90001G

Nott, T. J., Petsalaki, E., Farber, P., Jervis, D., Fussner, E., Plochowietz, A., Craggs, T. D., Bazett-Jones, D. P., Pawson, T., Forman-Kay, J. D., & Baldwin, A. J. (2015). Phase Transition of a Disordered Nuage Protein Generates Environmentally Responsive Membraneless Organelles. *Molecular Cell*, *57*(5), 936–947. https://doi.org/10.1016/j.molcel.2015.01.013

Papaneophytou, C. (2019). Design of Experiments As a Tool for Optimization in Recombinant Protein Biotechnology: From Constructs to Crystals. *Molecular Biotechnology*, *61*(12), 873–891. https://doi.org/10.1007/s12033-019-00218-x

Patel, A., Lee, H. O., Jawerth, L., Maharana, S., Jahnel, M., Hein, M. Y., Stoynov, S., Mahamid, J., Saha, S., Franzmann, T. M., Pozniakovski, A., Poser, I., Maghelli, N., Royer, L. A., Weigert, M., Myers, E. W., Grill, S., Drechsel, D., Hyman, A. A., & Alberti, S. (2015). A Liquid-to-Solid Phase Transition of the ALS Protein FUS Accelerated by Disease Mutation. *Cell*, *162*(5), 1066–1077. https://doi.org/10.1016/j.cell.2015.07.047

Pédelacq, J.-D., Cabantous, S., Tran, T., Terwilliger, T. C., & Waldo, G. S. (2006). Engineering and characterization of a superfolder green fluorescent protein. *Nature Biotechnology*, *24*(1), 79–88. https://doi.org/10.1038/nbt1172

Pollard, D. A., Pollard, T. D., & Pollard, K. S. (2019). Empowering statistical methods for cellular and molecular biologists. *Molecular Biology of the Cell*, *30*(12), 1359–1368. https://doi.org/10.1091/mbc.E15-02-0076

Quiroz, F. G., & Chilkoti, A. (2015). Sequence heuristics to encode phase behaviour in intrinsically disordered protein polymers. *Nature Materials*, *14*(11), 1164–1171. https://doi.org/10.1038/nmat4418

Ranganathan, S., & Shakhnovich, E. I. (2020). Dynamic metastable long-living droplets formed by sticker-spacer proteins. *eLife*, *9*, e56159. https://doi.org/10.7554/eLife.56159

Ranta-aho, J., Olive, M., Vandroux, M., Roticiani, G., Dominguez, C., Johari, M., Torella, A., Böhm, J., Turon, J., Nigro, V., Hackman, P., Laporte, J., Udd, B., & Savarese, M. (2022). Mutation update for the *ACTN2* gene. *Human Mutation*, *43*(12), 1745–1756. https://doi.org/10.1002/humu.24470

Rhee, D., Sanger, J. M., & Sanger, J. W. (1994). The premyofibril: Evidence for its role in myofibrillogenesis. *Cell Motility*, *28*(1), 1–24. https://doi.org/10.1002/cm.970280102

Ribeiro, E. de A., Pinotsis, N., Ghisleni, A., Salmazo, A., Konarev, P. V., Kostan, J., Sjöblom, B., Schreiner, C., Polyansky, A. A., Gkougkoulia, E. A., Holt, M. R., Aachmann, F. L., Žagrović, B., Bordignon, E., Pirker, K. F., Svergun, D. I., Gautel, M., & Djinović-Carugo, K. (2014). The Structure and Regulation of Human Muscle α-Actinin. *Cell*, *159*(6), 1447–1460. https://doi.org/10.1016/j.cell.2014.10.056

Rüttimann, B. G., & Wegener, K. (2015). The Power of DOE: How to Increase Experimental Design Success and Avoid Pitfalls. *Journal of Service Science and Management*, *08*(02), 250–258. https://doi.org/10.4236/jssm.2015.82028

Sanger, J. W., Kang, S., Siebrands, C. C., Freeman, N., Du, A., Wang, J., Stout, A. L., & Sanger, J. M. (2006). How to build a myofibril. *Journal of Muscle Research and Cell Motility*, *26*(6–8), 343–354. https://doi.org/10.1007/s10974-005-9016-7

Sanger, J. W., Wang, J., Fan, Y., White, J., Mi-Mi, L., Dube, D. K., Sanger, J. M., & Pruyne, D. (2016). Assembly and Maintenance of Myofibrils in Striated Muscle. In B. M. Jockusch (Ed.), *The Actin Cytoskeleton* (Vol. 235, pp. 39–75). Springer International Publishing. https://doi.org/10.1007/164_2016_53

Sanulli, S., & Narlikar, G. J. (2021). Generation and Biochemical Characterization of Phase-Separated Droplets Formed by Nucleic Acid Binding Proteins: Using HP1 as a Model System. *Current Protocols*, *1*(5), e109. https://doi.org/10.1002/cpz1.109

Schiaffino, S., Dyar, K. A., Ciciliot, S., Blaauw, B., & Sandri, M. (2013). Mechanisms regulating skeletal muscle growth and atrophy. *The FEBS Journal*, *280*(17), 4294–4314. https://doi.org/10.1111/febs.12253

Sjöblom, B., Salmazo, A., & Djinović-Carugo, K. (2008). α-Actinin structure and regulation. *Cellular and Molecular Life Sciences*, *65*(17), 2688–2701. https://doi.org/10.1007/s00018-008-8080-8

Spector, D. L. (2006). SnapShot: Cellular Bodies. *Cell*, *127*(5), 1071.e1-1071.e2. https://doi.org/10.1016/j.cell.2006.11.026

Sponga, A., Arolas, J. L., Schwarz, T. C., Jeffries, C. M., Rodriguez Chamorro, A., Kostan, J., Ghisleni, A., Drepper, F., Polyansky, A., De Almeida Ribeiro, E., Pedron, M., Zawadzka-Kazimierczuk, A., Mlynek, G., Peterbauer, T., Doto, P., Schreiner, C., Hollerl, E., Mateos, B., Geist, L., … Djinović-Carugo, K. (2021). Order from disorder in the sarcomere: FATZ forms a fuzzy but tight complex and phase-separated condensates with α-actinin. *Science Advances*, *7*(22), eabg7653. https://doi.org/10.1126/sciadv.abg7653

Squire, J. M., Al-khayat, H. A., Knupp, C., & Luther, P. K. (2005). Molecular Architecture in Muscle Contractile Assemblies. In *Advances in Protein Chemistry* (Vol. 71, pp. 17–87). Elsevier. https://doi.org/10.1016/S0065-3233(04)71002-5

Theile, C. S., Witte, M. D., Blom, A. E. M., Kundrat, L., Ploegh, H. L., & Guimaraes, C. P. (2013). Site-specific N-terminal labeling of proteins using sortase-mediated reactions. *Nature Protocols*, *8*(9), 1800–1807. https://doi.org/10.1038/nprot.2013.102

Uebel, C. J., & Phillips, C. M. (2020). *Phase-separated protein dynamics are affected by fluorescent tag choice*. https://doi.org/10.17912/micropub.biology.000143

Vernon, R. M., & Forman-Kay, J. D. (2019). First-generation predictors of biological protein phase separation. *Current Opinion in Structural Biology*, *58*, 88–96. https://doi.org/10.1016/j.sbi.2019.05.016

Von Nandelstadh, P., Ismail, M., Gardin, C., Suila, H., Zara, I., Belgrano, A., Valle, G., Carpen, O., & Faulkner, G. (2009). A Class III PDZ Binding Motif in the Myotilin and FATZ Families Binds Enigma Family Proteins: A Common Link for Z-Disc Myopathies. *Molecular and Cellular Biology*, *29*(3), 822–834. https://doi.org/10.1128/MCB.01454-08

Wadmore, K., Azad, A. J., & Gehmlich, K. (2021). The Role of Z-disc Proteins in Myopathy and Cardiomyopathy. *International Journal of Molecular Sciences*, *22*(6), 3058. https://doi.org/10.3390/ijms22063058

Wang, B., Zhang, L., Dai, T., Qin, Z., Lu, H., Zhang, L., & Zhou, F. (2021). Liquid–liquid phase separation in human health and diseases. *Signal Transduction and Targeted Therapy*, *6*(1), 290. https://doi.org/10.1038/s41392-021-00678-1

Wang, J., Shaner, N., Mittal, B., Zhou, Q., Chen, J., Sanger, J. M., & Sanger, J. W. (2005). Dynamics of Z-band based proteins in developing skeletal muscle cells. *Cell Motility and the Cytoskeleton*, *61*(1), 34–48. https://doi.org/10.1002/cm.20063

Wang, Z., Grange, M., Wagner, T., Kho, A. L., Gautel, M., & Raunser, S. (2021). The molecular basis for sarcomere organization in vertebrate skeletal muscle. *Cell*, *184*(8), 2135-2150.e13. https://doi.org/10.1016/j.cell.2021.02.047

White, J., Barro, M. V., Makarenkova, H. P., Sanger, J. W., & Sanger, J. M. (2014). Localization of Sarcomeric Proteins During Myofibril Assembly in Cultured Mouse Primary Skeletal Myotubes. *The Anatomical Record*, *297*(9), 1571–1584. https://doi.org/10.1002/ar.22981

Wiśniewski, J. R., Hein, M. Y., Cox, J., & Mann, M. (2014). A "Proteomic Ruler" for Protein Copy Number and Concentration Estimation without Spike-in Standards. *Molecular & Cellular Proteomics*, *13*(12), 3497–3506. https://doi.org/10.1074/mcp.M113.037309

Wu, X., Cai, Q., Feng, Z., & Zhang, M. (2020). Liquid-Liquid Phase Separation in Neuronal Development and Synaptic Signaling. *Developmental Cell*, *55*(1), 18–29. https://doi.org/10.1016/j.devcel.2020.06.012

Zhang, X., Li, H., Ma, Y., Zhong, D., & Hou, S. (2023). Study liquid–liquid phase separation with optical microscopy: A methodology review. *APL Bioengineering*, *7*(2), 021502. https://doi.org/10.1063/5.0137008

Zhuge, R., Wang, C., Wang, J., Yu, S., Liao, L., & Zheng, X. (2023). hCINAP regulates the differentiation of embryonic stem cells by regulating NEDD4 liquid-liquid phase-separation-mediated YAP1 activation. *Cell Reports*, *42*(1), 111935. https://doi.org/10.1016/j.celrep.2022.111935

7.1 List of Figures

7.2 List of Tables

8 Acknowledgements

First of all, I would like to thank my family for their support and encouragement. It was not an easy time and they always kept an eye on me from afar. Thank you for being so gentle with me and supporting me in pursuing what I want.

I thank my supervisor Professor Kristina Djinović-Carugo firstly for giving me the opportunity to work on this project that made a special place in my heart forever. She always shared her steps in logic with us and set the bar high in a direct and clear understanding and communication of everything, which made me grow so much. I will always be amazed and inspired by her energy.

I want to thank Philipp Galuska, who mentored and supervised me throughout my time on this project. He showed me A to Z on this project; even how to correctly use a blade while preparing the microscopy slides. I admire how flawless he works and it is not easy to express how grateful I am.

I would like to thank each of my lab members for their incredible patience with me and the interest they showed in what I had to say. I gained so much insight and a scientific intuition by being with them. Also, I recognize I was uniquely lucky to have honest, easygoing and super witty people around me. I wish each of them the best.

Lastly, I would like to thank my fellow students and colleagues from around the campus that shared their precious space and time with me, especially Jázmin Nagy. Our daily scientific discussions contributed immensely to this thesis.